Development of a Gaseous Electron-Tracking Compton Imaging Camera Using $LaBr_3$:Ce Scintillator and Its Application to Proton Therapy

Shunsuke Kurosawa

Department of Physics, Faculty of Science, Kyoto University
Kitashirakawa Oiwake-cho, Sakyo-ku, Kyoto, 606-8502, Japan
`kurosawa@cr.scphys.kyoto-u.ac.jp`

Abstract

MeV and sub-MeV gamma-rays imaging has been important for several scientific fields such as astronomy and medical imaging. However, present imaging detector works with a lower sensitivity than those in other energy range, because it is difficult to reconstruct Compton scattering which is a main interaction of photons with matter.

We have developed an electron-tracking Compton camera (ETCC) which consists of gaseous time projection chamber (TPC) and a position-sensitive scintillator. Since the gaseous TPC measures the electron-tracking, the ETCC is able to reconstruct Compton scattering event-by-event.

This camera is expected to be applied to above fields. Actually, we have already succeeded in imaging the cosmic and atmospheric gamma rays using our small size camera onboard a balloon in 2006. Then we have developed a larger camera in order to detect the bright celestial objects such as Cyg X-1.

In addition, we have developed the ETCC for the medical imaging for a diagnosis of a tumor, and the ETCC already have imaged small animals with agents including radio isotopes. Our ETCC is also expected to use in proton therapy, which is the one of the radiation therapies. Since charged particles have the sharp peak of the energy deposit (Bragg peak) near the end of the range, the tumor is killed efficiently. On the other hand, the normal cells around the tumor are less damaged than X-ray radiation therapy. Here, optimization of the proton range is decided by only the calculation before the therapy (planning step), while no monitoring system usually verifies the proton dose during the therapy.

During the proton therapy, prompt gamma rays are generated, and those prompt gamma rays are reported to trace the Bragg peak well.

Here, we demonstrated the imaging ability of the ETCC for those prompt gamma rays using water phantom irradiated with 140-MeV proton beam at Research Center for Nuclear Physics (RCNP) of Osaka University in 2010. The aim of this experiment is to detect the difference of the distributions between the annihilation and prompt gamma rays. As a consequence, we succeeded in obtaining different images between annihilation and prompt gamma-ray distribution, which is consistent with simulations. Thus we found that the ETCC has an imaging ability for continuum gamma rays, and this ability is useful for both medical imaging and astronomy.

The angular resolution of the ETCC depends on the energy resolution of absorber of the ETCC, and imaging performance for gamma rays strongly depends on the angular resolution of the ETCC. At present, a GSO:Ce array camera is used as an absorber, which has an energy resolution of 10.8 ± 0.3 % at 662 keV (FWHM). LaBr$_3$:Ce scintillator has an excellent FWHM energy resolution of ~ 3 % at 662 keV for a monolithic crystal. Although this scintillator has a hygroscopic nature, we developed LaBr$_3$:Ce arrays consisting of 8×8 pixels with a size of 5.8

mm ×5.8 mm ×15.0 mm. The FWHM energy resolution of all 64 pixels reached 5.7 ± 0.5 % at 662 keV. Using the $LaBr_3$:Ce arrays, an ETCC has an FWHM angular resolution of $4.2 \pm 0.3^{\circ}$ at 662 keV. In addition, we estimated an FWHM angular resolution of the array would be $\sim 3.5^{\circ}$ at 662 keV, if depth of interaction technique is used in the pixel scintillator.

Contents

1 Introduction **1**

2 Science of MeV Gamma Ray **7**

2.1 Interactions of Photons with Matter 7

2.2 Interactions of Charged Particle with Matter 10

2.3 Mechanism of Gamma-ray Radiation 12

2.4 Sub-MeV and MeV Gamma-ray astronomy 15

2.5 Medical Imaging and Proton Therapy 21

3 Compton and Other Gamma-Ray Imaging **28**

3.1 MeV Gamma-Ray Imaging Detector in Astronomy 28

3.2 MeV Gamma-Ray Imaging Detector in Medical Imaging 34

3.3 Electron-Tracking Compton Imaging 37

4 Gaseous TPC and Scintillator **41**

4.1 μ-PIC (Micro Pixel Chamber) 41

4.2 Gas Electron Multiplier 45

4.3 Time Projection Chamber with μ-PIC (μ-TPC) 46

4.4 Scintillation Camera 50

5 Performance of a Real-Time Monitor of Continuum Spectral Gamma Rays in Proton Therapy **56**

5.1 Verification of Dose in Proton therapy 56

5.2 Setup of the Beam Experiment Using the Compton Camera 60

5.3 Results of the Beam Test 69

5.4 Analysis of Imaging 73

5.5 Future Works 82

6 Improvement of Scintillator **86**

6.1 Position-Sensitive Scintillation Camera 86

6.2 Optimizing the Scintillator and the Pixel Size 88

6.3 ARM Calculation for the Selection of a Scintillator and the Pixel Size 88

6.4 LaBr$_3$:Ce Camera 91
6.5 Materials for LaBr$_3$:Ce Array Camera 93
6.6 Assembly of LaBr$_3$:Ce and GSO:Ce arrays 96
6.7 Performance of Array Camera 100
6.8 Improvement of a LaBr$_3$:Ce Array 104
6.9 Comparison with Other Position-Sensitive LaBr$_3$:Ce Camera 111
6.10 Performance of the Compton Camera with a LaBr$_3$ Array 112
6.11 Possibility of Improvement in Angular Resolution 115

7 Conclusion **117**

Chapter 1

Introduction

Recently sub-MeV and MeV gamma-ray imaging detector has been an important device in the several scientific fields such as astronomy, and nuclear medicine (e.g. [1, 2]). As for astronomy, an imaging detector in this energy band is expected to reveal a lot of interesting celestial objects such as black holes, gamma ray bursts (GRBs), and active galactic nuclei (AGNs). As for medical field, gamma-ray imaging is widely used in the diagnosis for searching a tumor with an agent.

However the quality of MeV gamma-ray imaging looks certainly less satisfied for its applications due to its low sensitivity, a poor angular or position resolution than imaging detectors used in other energy ranges. The main reason of the low sensitivity is that a main interaction of a photon in the matter is Compton scattering, which is a smallest cross section in the energy range of a few hundred keV to a few MeV. In order to obtain the direction of MeV photons, we must reconstruct the Compton scattering event-by-event, for which a Compton point, directions and energies of the scattered gamma ray, and those of the recoil electron have to be measured. However it is difficult to measure those all parameters, especially the direction of the recoil electron.

For MeV gamma-ray astronomy, several groups have so far developed imaging detectors using the reconstruction of Compton scattering, named a Compton camera. The Compton camera consists of a converter where the Compton scattering occurs, and an absorber where the scattered gamma-ray photon is measured. However such Compton cameras do not measure the direction of electrons in the parameters required for the reconstruction of Compton scattering, and thus localize the incident direction of a gamma ray only to an event circle as shown in Fig. 1.1 (a-1). Therefore they, written as ”classical Compton cameras”, must use three gamma-ray event circles at least in order to obtain the real direction of the point source as shown in Fig. 1.1 (a-2). In an actual observation, a lot of events should be accumulated to acquire some imaging quality. In addition, classical Compton cameras have little ability to reject the backgrounds like those coming from out of the field of the detector. In particular, in space, cosmic rays interact with the vessel of the satellite or the atmosphere, and then a lot of radioisotopes (RIs) are generated. Those RIs emit huge MeV gamma rays as much backgrounds for the detector.

For example, a classical Compton camera named COMPTEL detector onboard the Compton Gamma Ray Observatory (CGRO) satellite had provided various scientific results. However the large backgrounds deteriorated dramatically its imaging quality. As a consequence, COMPTEL had a less than half sensitivity (∼ 100 mCrab) of that designed before a launching [3], and only 32 objects were detected with the COMPEL in the MeV region [4], while 271 objects were detected with a GeV gamma-ray imaging detector [5], called the Energetic Gamma Ray Experiment Telescope (EGRET) on the CGRO.

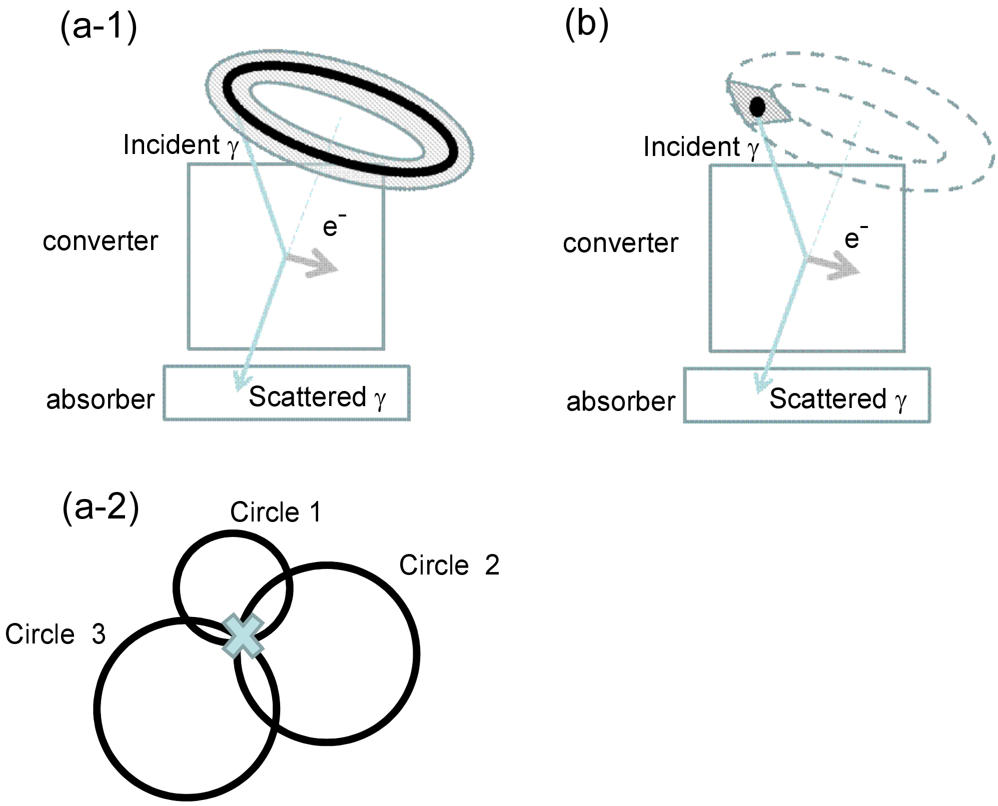

Figure 1.1: Schematic view of classical and advanced Compton camera as shown in (a-1) and (b), respectively. To determine a source direction with the classic one, three events must be measured and a cross point of obtained three circles is regard as the solution indicted as an X in Fig. (a-2).

Other types of imaging detectors using a collimator or a coded mask were developed and widely used in the energy regions of sub-MeV and MeV [6, 7, 8, 9, 10, 11]. Several groups succeeded in the observations in space using these detectors. However both detectors achieved a less sensitivity than the classical Compton camera in the sub-MeV and MeV region, because they do not select the signal photon or reject the noise one event-by-event by the measurement of the gamma-photon direction. As a result, the imaging by those detectors needs a lot of gamma photons and consequently degrades its sensitivity. Also the dynamic ranges of these detector are limited under a few hundred keV owing to i) difficulty in detecting events with sufficient statistics, and ii) Compton scattering or transparency for high energy gamma rays in the collimator or coded mask. In addition, in order to remove backgrounds coming from the outside of the field of view, a veto counter surrounding the detector such as a scintillator is indispensable. The veto counters which are usually heavier than the detector itself, are a disadvantage of the observation in space.

For medical imaging, the collimator technique is widely used in single photon emission computed tomography (SPECT) [12, 13]. For the SPECT imaging, an agent including gamma-ray emitting RI is used as a tracer which is injected into the body. Usually the agent concentrating in the active tissues such a tumor are used. In order to obtain a fine image, the fine collimation is necessary. However its available energy range is limited to approximately 80 - 300 keV due to its transparency for higher energy gamma rays.

An imaging detector specialized to the 511-keV annihilation gamma rays named a positron emission tomography (PET) has been recently popular on biological or medical imaging [14, 15]. By surrounding the target, the PET measures the back-to-back gamma rays, from an agent including a positron emitting RI in the body. Although the PET has a good spatial resolution of 0.5 cm for human imaging, the available RIs are limited to only positron emitting RIs.

In the energy range of sub-MeV gamma ray region, only the PET and SPECT are used as the medical imaging instruments, while in the MeV region, no instrument is used. Thus an available energy ranges for the medical imaging are restricted. However, there are a lot of RIs out of those energy ranges, and the RIs may have unknown potential to use as a new type of the agent.

For the treatment, gamma-ray imaging has not been used usually, but expected to be quite useful in the radiation therapy. Bennett et al. suggested the use of the PET imaging for the proton therapy [16]. Proton therapy is one of the charged beam radiation therapy using the Bragg peak, under which tumor cells are killed [17]. Here the proton energy is adjusted so that its Bragg peak position coincides with the tumor. This therapy is able to reduce unwanted side effects for the normal cells under the beam line. Although the optimization of the Bragg peak position is calculated before the treatment (planning), no detector measures the proton dose directly during the beam irradiation. In the planning step, the effect of the irradiation is usually verified by an X-ray computed tomography (CT) [18, 19]. However, the X-ray CT measures the electron density in the body. Then the optimizing calculation sometimes does not lead the Bragg position accurately when the treatment area includes complicated bone structures. At present, there is no method to measure the energy deposit of the proton beam around the tumor. Therefore it is necessary to monitor the proton beam range in the patient body during proton beam therapy.

Recently several groups have shown that the PET may be used for the determination of the radiation dose distribution in the patient after the proton therapy using the positron emitter in the body generated by the proton beam [20, 21]. However, the distribution of generated positron emitters in the patient is not considered to match well with the distribution of the radiation dose by the beam. The reason is that the positron emitters are more efficiently generated by the higher-energy protons than ~ 10 MeV. Moreover, the positron emitters such as ^{45}Ca tend to be accumulated in the bone, and the distribution of annihilation gamma rays from ^{45}Ca might trace the bone. In addition, the PET imaging cannot be operated during the beam-on time under the high counting rate due to the backgrounds.

During the proton beam radiation, prompt gamma rays are also generated by nuclear reaction. The simulation indicates that distribution of prompt gamma rays near the proton range is correlated with the proton dose, and the imaging of prompt gamma rays is expected to indicate the accurate dose distribution in the body [22]. Especially MeV gamma rays tend to be correlated with the proton dose than sub-MeV gamma rays. Thus, a novel detector is required to have ability of the imaging of continuum gamma rays above 1 MeV under the beam-on.

As mentioned above, MeV gamma-ray imaging is eagerly expected in several scientific fields. To obtain both a higher sensitivity and the ability of a good background rejection, we have developed an electron-tracking Compton camera (ETCC) which consists of a gaseous time projection chamber (TPC) and a scintillator array as shown in Fig. 1.2 [24, 25, 26, 27]. The TPC has a sensitive volume of 10 cm ×10 cm ×10 cm or 30 cm ×10 cm ×30 cm [28, 29, 30], which is equipped with a gaseous avalanche detector consisting of a gas electron multiplier (GEM) [31, 32] and a micro pixel chamber (μ-PIC) [33, 34]. When an incident gamma ray is scattered via Compton process in the TPC, both the three-dimensional track and energy of a Compton recoil electron are measured [28, 29]. At the same time, the scintillator array measures the energy and position of the scattered gamma ray. By combining these measurements, the ETCC is able to reconstruct a full process of Compton scattering event-by-event, which enables us to restrict the incident direction of a gamma ray on the arc (not circle) region as shown in Fig. 1.1 (b). In addition, the ETCC has a wide field of view (~ 3 str) and wide energy dynamic range (~ 0.1 -a few MeV). Moreover the ETCC can reject backgrounds efficiently using a geometrical fitting for an angle between a recoil electron and a scattered gamma ray.

Thus the ETCC has several unique features, and hence we have continued a development of the ETCC. Our goal for astronomy is to explore the all sky with a higher sensitivity than COMPTEL by an order of magnitude. As a first step, we had developed a small ETCC including a 10-cm squared μ-PIC successfully, and observed cosmic and atmospheric gamma rays using a balloon in 2006 [35, 36]. Then we are improving a larger ETCC with a higher sensitivity in order to detect the bright celestial objects such as Crab and Cyg X-1 by a balloon-born experiment planned in 2012.

In addition, I analyzed which component of the ETCC has a dominant effect to improve the angular resolution. Then based on its results, I improved the energy and angular resolution of the ETCC by developing a new scintillator array, and the angular resolution was expected to be better than COMPTEL. This novel scintillator camera was successfully assembled into the array with my own technique.

Since the ETCC is also surely expected to be useful for medical imaging, and we have carried out the performance test of the ETCC such as spatial resolution, and the energy range

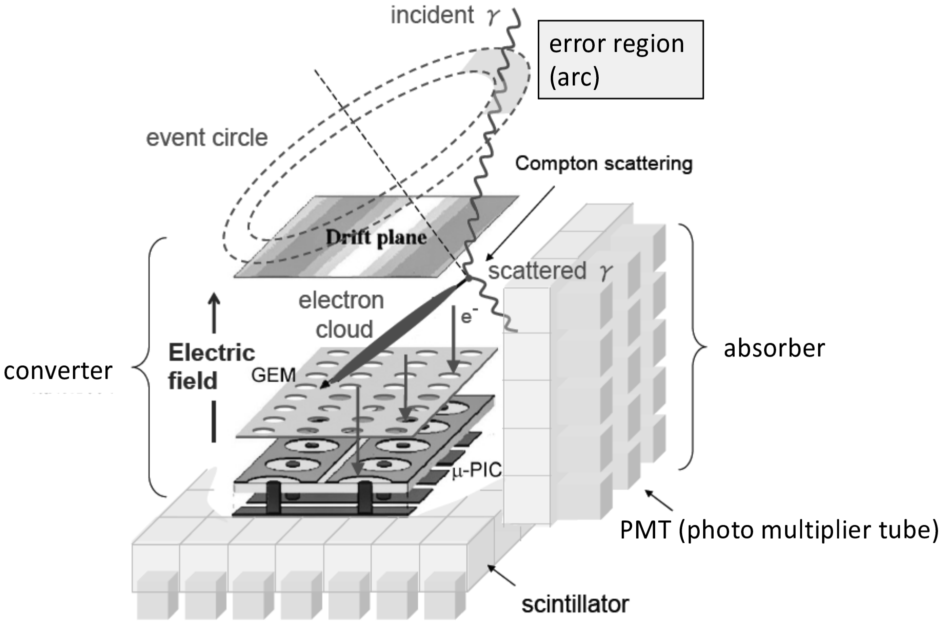

Figure 1.2: Schematic view of the ETCC (advanced Compton camera).

for medical use [37, 38]. We have obtained gamma-ray images with a high energy RI up to approximately 1.3 MeV (e.g., 1.116 MeV from ^{65}Zn), and multi-RI tracers for small animals.

In proton therapy, the monitor of the Bragg peak position and the dose in situ are required. The ETCC looks a suitable imaging detector measuring prompt gamma rays, and one of the purposes of this thesis is to demonstrate the feasibility of the ETCC for it. We carried out an experiment on the gamma-ray imaging of the ETCC using continuous gamma rays including prompt gamma rays from a water tank irradiated with 140-MeV proton beam at Research Center for Nuclear Physics (RCNP) of Osaka University in 2010. This beam test was the first experiment as a continuous gamma-ray imaging with a Compton camera, and it provided two important suggestions. One was that the ETCC is able to use as a real-time monitoring system of proton therapy. The other was that the ETCC has an advantage for MeV gamma astronomy because most objects in the universe emit a continuum gamma ray spectrum.

The outline of this thesis is as follows. In Chapter 2, I describe the interactions of photons with matter, and sciences of astronomy and medical imaging. In particular, I show the detail of proton therapy in the section of medical imaging.

Chapter 3 and 4 are expositions about imaging detectors. In Chapter 3, I illustrate a history and mechanism of the MeV gamma-ray imaging detectors including Compton camera and other devices. In Chapter 4, the structure of the ETCC including a gaseous TPC and scintillator are described.

In Chapter 5, the development of the real-time monitor for proton therapy is shown. In addition, because of the wide energy dynamic range, our ETCC can obtain an image with continuum spectral gamma rays. Then I demonstrate an image from a water tank irradiated with proton beam.

I have developed a new position-sensitive scintillation camera using a $LaBr_3$:Ce crystal in order to improve the spatial resolution of an ETCC. In Chapter 6, I explain why I have developed the new scintillation camera with a higher energy resolution, and the detail of development and performance of the $LaBr_3$:Ce camera. In addition, the performance of the ETCC using the $LaBr_3$:Ce is shown.

Chapter 2

Science of MeV Gamma Ray

2.1 Interactions of Photons with Matter

In this and next sections, I describe the interaction of photons and charged particles with the matter, respectively. The main interactions of high energy photons from X-rays to gamma rays with the matter are photo-absorption, Compton scattering and pair production as its energy increasing. The cross sections of these interactions depend on the energy of photons and the atomic number Z of the matter. Figures 2.1 and 2.2 show each cross-section of the interaction with Argon, and the dominant interaction as a function of the photon energy.

In less than 100 keV region, the photoelectric absorption is a dominant interaction. This process provides the energy of a photon into an electron in the atom, and ejects the electron, called photoelectron, from the atom When a photon with an energy of E_0 makes a photoelectron, the kinetic energy of the photoelectron is as follows,

$$K_e = E_0 - E_{\mathrm{bind}}, \tag{2.1}$$

where E_{bind} is the binding energy of the photoelectron in the atom. If E_0 is higher than the binding energy of the K shell, the probability of the interaction with an electron in K shell is maximum. Then the cross section of the photoelectric absorption of a K shell electron is:

$$\sigma_K = 4\sqrt{2}Z^5 \left(\frac{8\pi}{3}r_e^2\right)\left(\frac{e^2}{4\pi\varepsilon_0\hbar c}\right)^4\left(\frac{m_e c^2}{E_0}\right)^{7/2}, \tag{2.2}$$

where r_e is the classical electron radius:

$$r_e = \frac{e^2}{4\pi\epsilon_0 m_e c^2}. \tag{2.3}$$

In the energy band from a few hundred keV to 10 MeV, Compton scattering is the dominant interaction. this scattering is an elastic scattering of a gamma ray and an electron. Figure 2.3 shows Compton process, in which an incident gamma-ray photon provides a part of the initial energy to a recoil electron, and simultaneously the gamma-ray photon is scattered as its energy becoming lower.

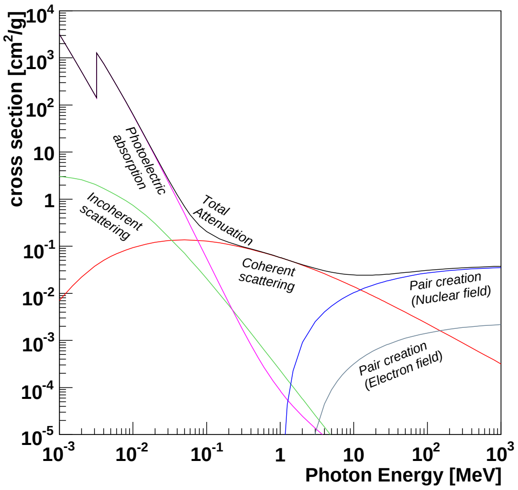

Figure 2.1: The cross-section of the interaction between gamma rays and matter (Argon) [39].

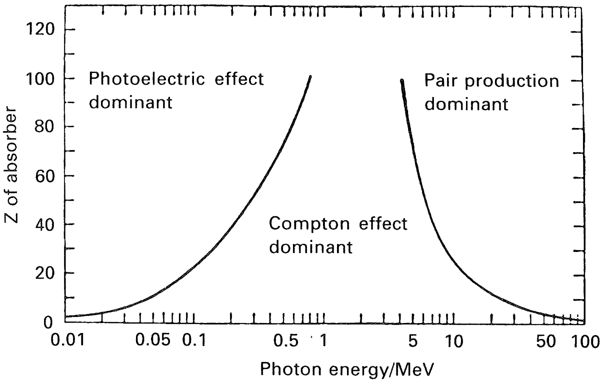

Figure 2.2: The significant interaction between gamma rays and matter [40].

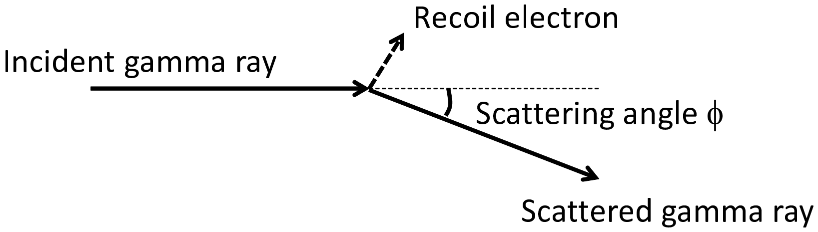

Figure 2.3: Schematic view of Compton scattering.

When the gamma ray photon with an energy of E_0 scatters through Compton process with a free electron, the energy of the scattered gamma ray is

$$E' = \frac{E_0}{1 + \frac{E_0}{m_e c^2}(1 - \cos\phi)}, \tag{2.4}$$

and the energy of the recoil electron is

$$K_e = E_0 - E' = \frac{\frac{E_0}{m_e c^2}(1 - \cos\phi)}{1 + \frac{E_0}{m_e c^2}(1 - \cos\phi)} E_0, \tag{2.5}$$

where ϕ is a scattering angle. The angular distribution of the scattered gamma rays is represented by the differential scattering cross section as follows,

$$\frac{d\sigma}{d\Omega} = Z r_e^2 \left(\frac{1}{1 + k(1 - \cos\phi)}\right)^2 \left(\frac{1 + \cos^2\phi}{2}\right) \left(1 + \frac{k^2(1 - \cos\phi)^2}{(1 + \cos^2\phi)\left[1 + k(1 - \cos\phi)\right]}\right), \tag{2.6}$$

where σ and Ω are the cross section, and the solid angle, respectively, and $k = \frac{E_0}{m_e c^2}$. The angular distribution is shown in Figure 2.4.

In a real atom, electrons do not rest and they have the finite momentum of the orbit. Therefore, the gamma-ray scattered at the fixed angle from a monoenergetic source has some intrinsic fluctuation in its energy (the "Doppler broadening").

When the gamma-ray energy exceeds twice of the rest mass of the electron, a pair creation occurs, especially it is dominant interaction above 10 MeV. This interaction is to create a pair of an electron and a positron with the interaction between the photon and an electric field around the nucleus. The energies of an electron and a positron emitted from the photon of the energy E_0 must be satisfied with the following equation,

$$E_0 = E_- + E_+ + 2m_e c^2. \tag{2.7}$$

where E_- and E_+ are kinematic energy of an electron and a positron, respectively. The cross section is proportional to Z^2.

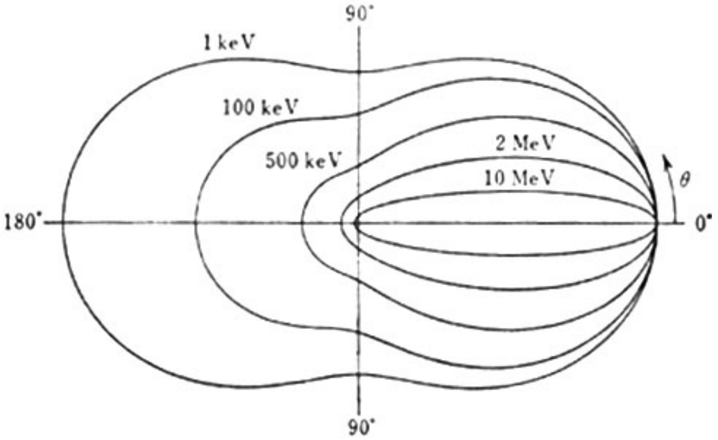

Figure 2.4: The angular distribution of Compton scattering [40].

One of the different properties between photons and charged particles is range. Although charged particles define the range, gamma rays have no well-defined range. X/gamma rays are attenuated exponentially based on the probability function as they pass through matter. The attenuation of gamma rays is given by:

$$I(x) = I_0 e^{-\mu x}. \tag{2.8}$$

where $I(x)$ is the gamma ray intensity as a function of the distance x into the material, I_0 is constant (intensity at $x = 0$), and μ is the mass attenuation coefficient. The mass attenuation coefficient depends on gamma-ray energy and the material with which the gamma rays interact.

2.2 Interactions of Charged Particle with Matter

In the matter, charged particles lose the energy by following processes:

1. Coulomb interaction with an electron or atomic nucleus
2. Bremsstrahlung
3. Interaction with atomic nucleus
4. Cherenkov radiation

I mention on the lower energy particles with a less than a few hundred MeV, and I ignore the interaction with atomic nucleus in this thesis. Also, Cherenkov radiation is not described in this section, because the energy loss is small by Cherenkov for our experiment.

In Coulomb interaction, ionization occurs in a target atom of the matter by a charged particle. The energy of an emitted electron E_e is follows:

$$E_e = E_{int} - I, \tag{2.9}$$

where E_{int}, and I are, Coulomb energy given by a charged particle into the atom, and the ionization potential of the atom. In addition, by Coulomb interaction, excitation occurs when the charged particle has a larger energy than the excite energy, and then a photon emits with an energy of the difference between the states in the atom. The event with ionization or excitation is called an inelastic scattering (inelastic collision).

The energy loss of the charged particle by the inelastic scattering is described by Bethe-Bloch formula is as follows:

$$\frac{dE}{dx} = 4\pi r_e^2 z^2 \frac{m_e c^2}{\beta^2} NZ\{\log\left(\frac{2m_e c^2}{I}\beta^2\right) - \log(1-\beta) - \beta^2\}, \tag{2.10}$$

where c, m_e, e, z, N, Z, and I are velocity of light, rest mass of the electron, charge of the electron, particle charge number, number of atom per unit volume in the matter, atomic number of matter, and mean excitation potential of the matter, respectively. In addition, $\beta = v/c$ (v is velocity of the charged particle) and r_e is a classical electron radius defined by Equation 2.3

This formula means that the energy deposit increases dramatically in the end of the range where the particle velocity is close to zero. However, this formula 2.10 is derived based on an assumption that the charged particles has a constant charge when the particle travels in the matter. Therefore this formula cannot be used when the particles have $Z > 1$ except alpha particle.

In the bremsstrahlung, ionizing process deposits a continuous energy in the matter. When a charged particle with the charge number of z and the mass of M passes the matter of an atomic number Z, the intensity I is described as follows:

$$I \propto \frac{z^2 Z^2}{M^2}. \tag{2.11}$$

This equation indicates that gamma-ray emission from the bremsstrahlung process is mostly caused by an electron or a positron, because the mass of the proton or other charged particle are heavier than the electron by an order of 10^3 or more.

This energy loss of an electron or a positron by the bremsstrahlung $\frac{dE}{dx}_b$ is approximately described as follows:

$$\frac{dE}{dx}_b = \frac{ZT(MeV)}{750}\frac{dE}{dx}_e, \tag{2.12}$$

where Z, T, and $\frac{dE}{dx}_e$ are an atomic number of target atom, kinematic energy of electron or positron, and the energy loss by the inelastic scattering, respectively.

2.3 Mechanism of Gamma-ray Radiation

By various processes listed below, continuous or line gamma rays are emitted.

◇ continuous gamma rays

- Thermal radiation
- Synchrotron [electron]
- Bremsstrahlung [electron, nucleus]
- (Inverse) Compton scattering [electron, photon]

◇ line gamma rays / broadening line

- nuclear transitions (de-excitation, radioactive decay, neutron capture) [nucleus, (neutron)]
- annihilation line [electron, positron]
- pion decay [pion]

Here, in the square bracket of the above list denotes the particle related to the process.

Thermal radiation is emission from a large population of electromagnetically interacting particles in equilibrium with their mean energy characterized by temperature T. The spectrum of radiation intensity follows the 'black body' distribution, and the energy density of radiation at frequency ν is

$$I_\nu = \frac{8\pi h\nu^3}{c^3}\frac{1}{e^{h\nu/k_BT}-1}, \tag{2.13}$$

where h is Planck's constant, and k_B is Boltzmann's constant. For a thermal gamma-ray photon of 1 MeV, the corresponding temperature would be above 10^9 K. Thus, thermal process is not dominant, and nonthermal processes are a more dominant source of gamma rays. In the MeV region, several nonthermal processes exist as follows.

When a relativistic electron moves in the magnetic field B, an electron trajectory will be changed by the Lorentz force. Because any acceleration of the charged particle can be viewed as the modification of the field, the kinetic energy of the electron is transformed into the energy of the electromagnetic field. For the relativistic electron, such an energy is lost as an emission of photon, which is called Synchrotron Radiation.

Synchrotron radiation spectrum has a characteristic peak described as

$$h\nu_c = \frac{3h}{4\pi}\frac{eB_\perp}{m_ec}\left(\frac{E_e}{m_ec^2}\right)^2, \tag{2.14}$$

where, e, m_e, E_e are the charge, the mass, the energy of the electron, respectively, and $B_\perp = B\sin\theta$, where the pitch angle θ is the angle between the particle trajectory and the direction of the magnetic field . The total energy loss rate by synchrotron radiation of an electron moving in the magnetic field B is

$$-\left(\frac{dE_e}{dt}\right)_{\rm syn} = \frac{4}{3}\sigma_T c \frac{B^2}{8\pi}\gamma^2\beta^2, \tag{2.15}$$

where σ_T is Thomson cross section described followings:

$$\sigma_T = \frac{8\pi e^4}{3m_e^2 c^4} \tag{2.16}$$

Another important process of gamma-ray production is 'Bremsstrahlung'. When an electron passes very near the nucleus, the trajectory of the electron is substantially changed by the strong electric field of the nucleus, and photons are emitted by the same process as that in synchrotron.

The spectrum of bremsstrahlung radiation remains flat up to roughly the electron kinetic energy, and it drops sharply toward zero above the electron energy. For relativistic electrons in a fully ionized plasma (no screening), the bremsstrahlung loss is

$$-\left(\frac{dE_e}{dt}\right)_{\rm B} = 4n_a Z^2 r_0^2 \alpha c \left(\ln\frac{E_e}{m_e c^2} + 0.36\right) E_e. \tag{2.17}$$

In the case of total screening, above formula is modified to

$$-\left(\frac{dE_e}{dt}\right)_{\rm B} = 4n_a Z^2 r_0^2 \alpha c \left(\ln\frac{183}{Z^{-1/3}} - \frac{1}{18}\right) E_e, \tag{2.18}$$

where n_a is the target atom density, $r_0 = \frac{e^2}{m_e c^2}$ is the classical radius of the electron, and α is the fine structure constant.

When an energetic photon collides with a low energy electron, the photon is scattered and some of the photon energy transfers to the electron. This process is called Compton scattering. The inverse process also surely exists, and generates a gamma-ray photon: when the low energy photon collides with an energetic electron, this photon has some energies from the electron via the collision. This 'Inverse Compton Scattering' is important in the regions of the high photon density.

The energy loss for an electron in the photon field energy density $w_{\rm ph}$ is written as

$$-\left(\frac{dE_e}{dt}\right)_{IC} = \frac{4}{3}\sigma_T c w_{\rm ph}\gamma^2\beta^2. \tag{2.19}$$

A nucleus has several specific, quantized states of the energy to bind the nucleons. These nuclear states have typical energy bands of the sub-MeV or MeV scale, and hence the transition between those states of a nuclear absorbs or emits the MeV gamma-ray photons. Thus, line gamma rays are emitted from 'de-excitation' of a nucleus:

$$X^* \longrightarrow X + \gamma, \tag{2.20}$$

and 'radioactive decay':

$$X \longrightarrow Y^* + e^+ \longrightarrow Y + \gamma. \tag{2.21}$$

Table 2.1: The gamma rays by nuclear transitions [41, 43, 44, 45]

process	Reaction	Energy [MeV]	half life*
De-Excitation	^{12}C(p, 2p)^{11}B*	4.444	
	^{14}N(p, p*)^{14}B*	$2.313, 5.105$	
	^{16}O(p, p*)^{16}O*	$2.741, 6.129, 6.917, 7.117$	
	^{26}Mg(p, p*)^{26}Mg*	1.809	
	^{56}Fe(p, p*)^{56}Fe*	$0.847, 1.238, 1.811$	
radioactive decay	^{56}Ni	$0.158, 0.270, 0.480, 0.759, 0.812$	6.10 d
	^{56}Co	$0.847, 1.238, 2.598$	77.2 d
	^{57}Co	$0.122, 0.136$	271.7 d
	^{44}Ti	1.157	63 y
	^{26}Al	1.809	7.4×10^5 y
	^{60}Fe	$1.173, 1.333$	1.5×10^6 y
capture	$n +^1 \mathrm{H} \rightarrow^2 \mathrm{D} + \gamma$	2.223	

$\star$ d: day, y: year

De-excitation occurs by the energetic collisions of cosmic-rays with the interstellar gas nuclei, in space. On the other hand, a radioactive decay occurs by nuclearsynthesis in a supernova and a core of heavy stars. The examples of line gamma-ray emissions by nuclear transitions expected in the universe are listed in Table 2.1. The observation of line gamma rays from this process lead to identify the origin of the nucleus.

Pion is a boson involved in the strong nuclear interaction, and is created during the strong-interaction events such as collisions of cosmic-ray protons with ambient-gas nuclei. The dominant π-producing channels in hadronic interactions are as follows,

$$p + p \longrightarrow p + p + a\pi^0 + b(\pi^+ + \pi^-), \tag{2.22}$$

$$p + p \longrightarrow p + n + \pi^+ + a\pi^0 + b(\pi^+ + \pi^-), \tag{2.23}$$

$$p + \alpha \longrightarrow p + p + a\pi^0 + b(\pi^+ + \pi^-), \tag{2.24}$$

$$p + \alpha \longrightarrow p + n + \pi^+ + a\pi^0 + b(\pi^+ + \pi^-), \tag{2.25}$$

where a and b are positive integers. π^0 decays rapidly into two gamma rays with a proper time of 9×10^{-17} sec, and the distribution of the number of photon has a peak at approximately 70 MeV at the center of gravity system, which is the half of the rest mass of pion. Since pions created by energetic protons has a momentum distribution, the observed gamma-ray spectrum of the pion decay is broadened by Doppler shift.

An electron-positron annihilation is an important source of gamma rays. In the annihilation, two or more photons are created, and the total energy of electron and positron is distributed to these photons. A positron and an electron may form a bound system, which is called positronium, and two different states exist. One is the ground state, and a positronium decays to two gamma rays. In this case, each photon has an energy of 511 keV, which is equal to the rest energy of an

Table 2.2: Interest of the Sub-MeV and MeV gamma-ray astronomy

physical features	science target
line gamma	Nucleosynthesis (supernovae)
$\pi^0\gamma$ reaction	Origin of the cosmic rays
transparency	Compact object (e.g. AGN, blackhole)
	Deep Field (e.g. gamma ray bursts)

electron. Here the two-gamma photons are emitted in the direction opposite (180°) at rest. The other state is the parallel-spin state, and it decays to three gamma rays having the continuum spectrum.

Actually, the 511 keV line was observed near the Galactic Center by The Solar Maximum Mission (SMM), The Oriented Scintillation Spectrometer Experiment (OSSE), and INTEGRAL (Fig 2.6), and implied the annihilation rate of $\sim 2 \times 10^{43}$ sec^{-1}. Annihilation photons suggests the existence of the electron-positron plasma. Low energy positrons are produced by β^+-decay, higher energy gamma photon (more than 1.022 MeV). The examples of the radioactive isotopes causing β^+-decay are ^{26}Al, ^{44}Ti, ^{56}Co, and the distinct nova also products ^{13}N and ^{18}F.

2.4 Sub-MeV and MeV Gamma-ray astronomy

Sub-MeV and MeV gamma-ray astronomy began in 1950's when Hayakawa et al. predicted that gamma photon might be emitted by π^0 decay process which is generated by cosmic rays [46, 47]. After that, the cosmic gamma rays was reported by several detectors on the satellites such as OSO-3 (1972) [48, 49], SAS-2 (1973) [50], and COS-B (1975) [51].

The physical features (process) of Sub-MeV and MeV gamma-ray region is listed in Table 2.2. The line gamma rays are generated in the supernovae where nucleosynthesis occurs. For example, radioactive nuclides such as ^{56}Ni and ^{44}Ti (Table 2.1), which produced by α process, emit gamma photons with an energy of a few hundred keV.

In 1982, Mahoney et al. detected line gamma-ray emission from ^{26}Al (1.809 MeV),^{60}Fe (1.173,1.332 MeV) using germanium-photon counting detectors onboard *HEAO 3* [52]. Figure 2.5 shows the all sky map of 1.8 MeV from the decay of ^{26}Al observed by COMPTEL [41], and ^{26}Al are mainly distributed in the galactic plane. COMPTEL's results reveal that the main contributors to the synthesis of ^{26}Al are most likely the massive stars, which contribute through their winds (Wolf-Rayet stars) and through their supernova explosion [53].

511-keV gamma rays are also found to concentrate in the Galactic center by INTEGRAL shown in Fig. 2.6 [54]. Several groups proposed the models or source objects for 511-keV emission such as positron production from Sgr A* [55], MeV-mass dark matter[54], microquasars [56], etc.

In addition, line gamma rays are generated in solar flare by a neutron capture (2.22 MeV), and de-excitation process such as ^{12}C(p, 2p)^{11}B* (4.44 MeV) [57]. These line gamma rays are

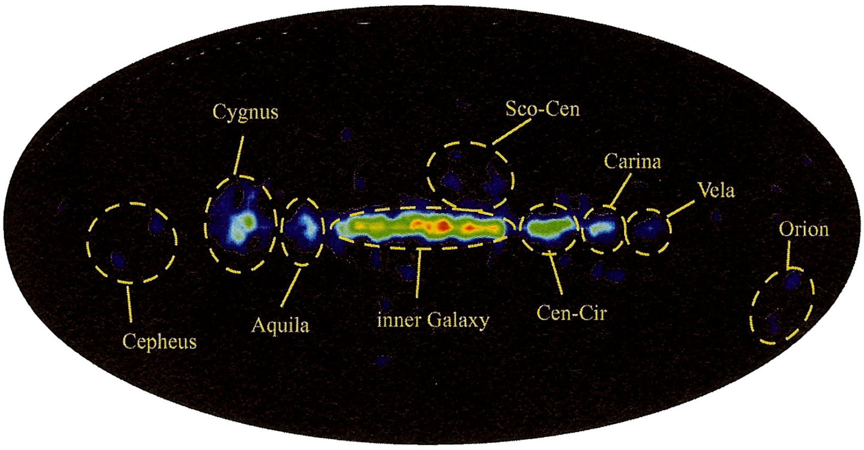

Figure 2.5: All sky map in 1.8 MeV by COMPTEL [41]

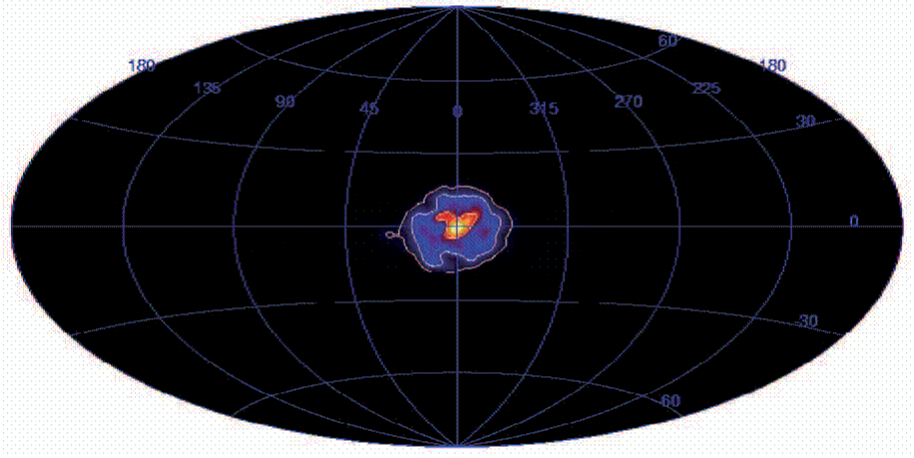

Figure 2.6: 511-keV line gamma rays map in the Galactic center with an INTEGRAL [54].

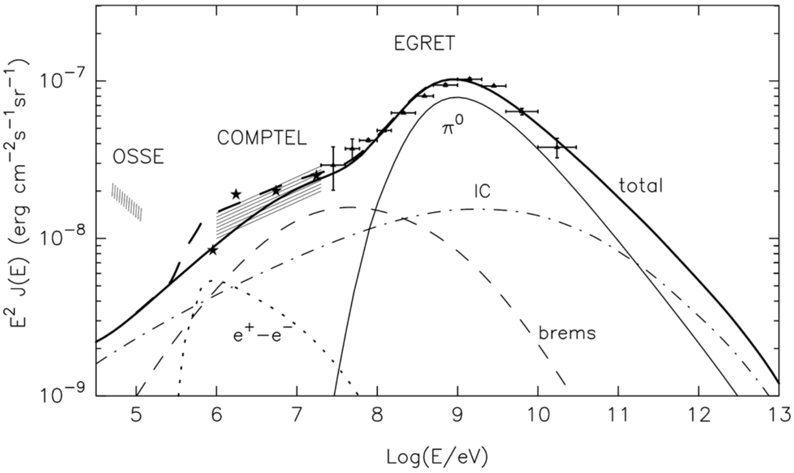

Figure 2.7: Fluxes of diffuse radiation produced by both electronic and nucleonic components of cosmic rays in the inner Galaxy [59]. Contributions from π^0-decay (thin solid line), bremsstrahlung (dashed), inverse Compton (dot-dashed), and positron annihilation in flight (dotted line) are shown.

produced by proton acceleration in the sun. By the observation of various line gamma rays, the history of the nucleosynthesis are would be cleared.

The study of gamma rays from π^0-decay directly shows the existence of high energy relativistic hadrons [58]. Figure 2.7 shows the fluxes of gamma ray emission from the galactic disk, and π^0 observation is important for the understanding of the sites and acceleration mechanism of galactic cosmic rays [59].

Since the universe are more transparent to MeV gamma rays than other energy band, gamma rays are a good probe for compact objects and the deep universe. The deep universe survey provides us the understanding in cosmological parameters and the history of the star formation. GRB, for example, has a uniform spatial distribution up to high redshift range. Some groups reports that GRB is a candidate for a standard candle, which is used to measure the far distance [60]. Indeed, Swift satellite discovered a GRB (GRB 090423), which is the most distant cosmic explosion (at present) ever seen with a redshift of 8.2 [61, 62].

Extragalactic diffuse gamma rays come from the outside of the Galaxy, of which the distribution is uniform in the all sky. Figure 2.8 is the spectrum of the extragalactic diffuse gamma rays. The spectrum shows that the majority is considered to be gamma rays by blazars and non-blazar AGNs in the energy region of MeV gamma rays.

Although the gamma ray imaging in astronomy is important to resolve the above issues, the imaging observation in the sub-MeV and MeV gamma region is not sufficient. For example, Compton Gamma-Ray Observatory (CGRO, 1991-2000) satellite had 4 detectors: COMPTEL,

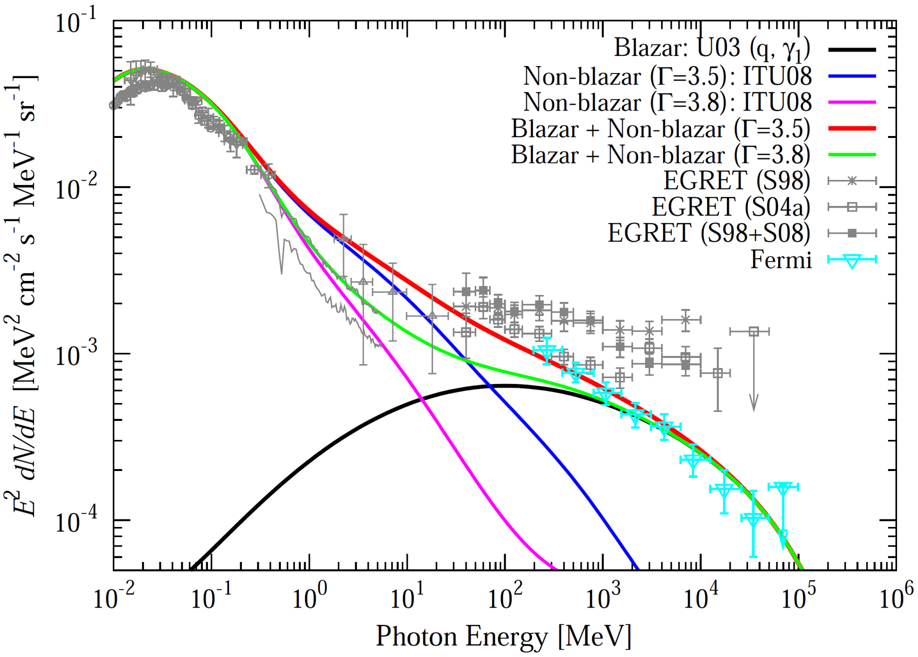

Figure 2.8: Spectrum of extragalactic diffuse gamma-ray [63], which is from non-blazar AGNs and blazars for a blazar gamma-ray luminosity function model. The model curves for the blazar component (absorbed+cascade), non-blazar AGN component, and the sum of the two are shown. (detail are described in [63].)

EGRET, OSSE and Burst And Transient Source Experiment (BATSE). COMPTEL found about 30 steady gamma-ray sources in the MeV region [64], while EGRET found about 270 sources in the sub GeV region [65]. Figures 2.9 and 2.10 show the all sky maps of the gamma-ray photons obtained by EGRET and COMPTEL, respectively. In addition, the Large Area Telescope (LAT) on the Fermi Gamma-ray Space Telescope (Fermi) released the First Fermi-LAT catalog (1FGL) containing 1451 sources detected and characterized in the 100 MeV to 100 GeV range during an approximately 2-year observation (Fig. 2.11). In the present circumstances, fewer sources are observed in the MeV and sub-MEV region than GeV and sub-GeV region by approximately two orders of magnitude.

To improve the imaging quality, we have developed an ETCC for the all-sky survey. The next chapter, I describe the detail of our ETCC and the imaging.

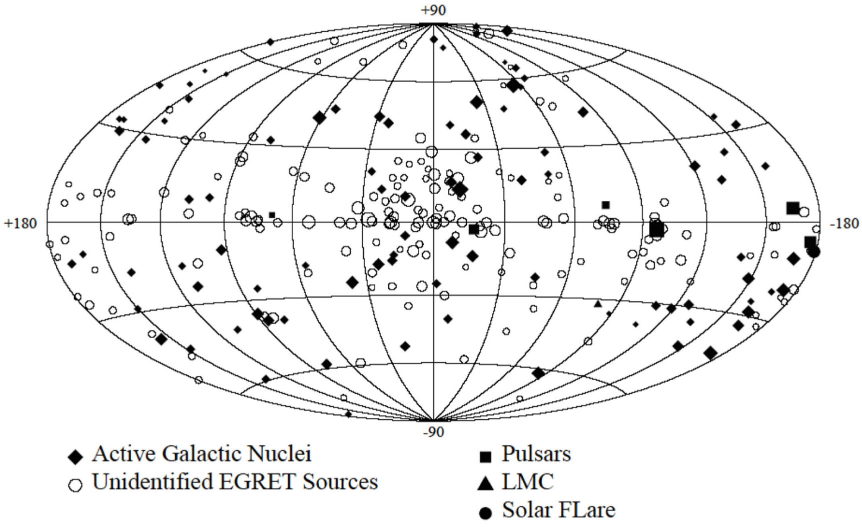

Figure 2.9: Distribution of the gamma-ray objects by EGRET [65].

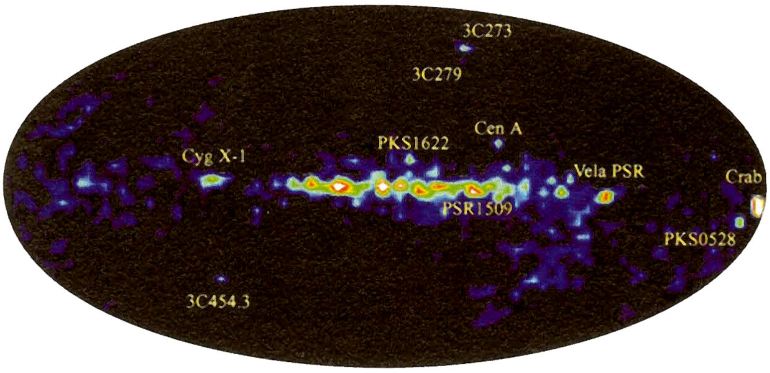

Figure 2.10: All sky map by COMPTEL (1 - 30 MeV) [41].

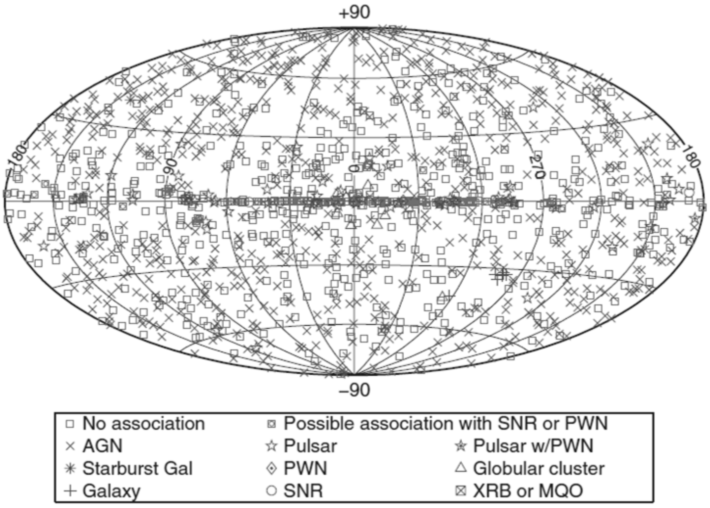

Figure 2.11: The distribution of the gamma-ray objects by LAT [66].

Table 2.3: Isotopes used in nuclear medicine

Isotope	Energy (keV)	Decay	Half-time
^{99m}Tc	140	IT*	6 hours
^{131}I	365	β^{-} decay	8 day
^{18}F	511	β^{+} decay	109.8 mim.
^{15}O	511	β^{+} decay	2 mim.

*:isomeric transition.

2.5 Medical Imaging and Proton Therapy

2.5.1 Medical Imaging

Medical imaging is to image and examine a tumor (cancer) in the human or animal body for a diagnosis and treatment. Although there are some medical imaging techniques such as Ultrasound imaging, thermal imaging, I briefly introduce the X and gamma-ray imaging techniques. The both X and gamma-ray are ionizing radiation, however gamma rays have a strong penetration ability through the human body than the X-rays as described in section 2.1. Then X-rays are used for examination of the density of the tissue in the body. Since tumors tend to be denser than normal ones, X-ray imaging is able to check the difference of the density. However a small or young tumor may be missed by the X-ray photograph.

On the other hand, a nuclear medicine imaging technique displays the distribution of not the density of the tissue, but the some biological activity using an agent with some RI. This agent tends to accumulate in the tumor based on the cellular function and physiology, and gamma rays from the RI are detected using two or three-dimensional detectors to localize the tumor. Since the detectors for the medical gamma-ray imaging such as the PET and SPECT have a narrow energy dynamic range, there are energy limits in use of isotopes in the agent. Table 2.3 lists common isotopes used in nuclear medicine.

2.5.2 Proton Therapy

Radiation therapy is a treatment method of a tumor using photons or charged particles, and the tumor is killed by the energy deposit from the photons or charged particles. Compared with other tumor treatment such as surgery and chemotherapy, the patient has only a small impact and long-term hospitalization is not necessary. In addition, chemotherapy usually has an adverse drug reaction. However radiation therapy also has a risk to kill the normal cells, if the Bragg peak does not match with the target.

Figure 2.12 shows relative dose distribution of conventional photon (X-ray) radiation as compared to proton radiation as the beam penetrates body tissue [67]. X-ray photons deposit much more energy in front of the tumor region than the tumor region. In addition, there is some energy deposit beyond the tumor. On the other hand, protons have minimal side scatter in the tissue than X-rays, and protons lose most of their energy at the end of their range corresponding

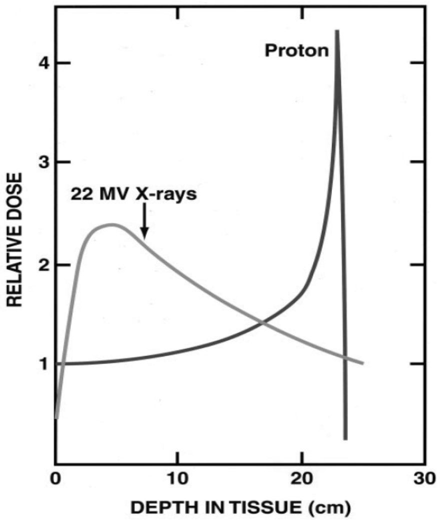

Figure 2.12: Relative dose distribution of conventional photon (X-ray) radiation as compared to proton radiation (250 MeV) as the beam enters and traverses body tissue. [67]

to the tumor. Therefore proton therapy is safer to normal cells than X-rays therapy.

The width of Bragg peak is generally narrow for actual size of the tumor. Then in order to adjust the Bragg peak position to the tumor position, either a variable filter in front of the patient, or a variable energy beam, called Spread out Bragg peak (SOBP) is used. Proton therapy is applied for the treatment of various disease sites [68] including paranasal sinus tumors [69], chordoma [70, 71], chondrosarcoma [72], lung tumors [73] etc.

In order to ensures that the treatment position matches the tumor, before the treatment, the proton range is commonly calculated based on the information of electron density distributions measured from the X-ray CT images. However this calculation has uncertainty due to different electron densities tissues such as bone[75]. The proton range uncertain is even 1-2 cm [77].

To verify the Bragg peak position (dose) in the body, gamma rays emitted by proton beam are studied, because the gamma-ray emission is related to proton energy deposit as shown in Fig. 2.14, which is a simulated result by GEANT 4.

Here, in proton therapy, the mechanism of gamma-ray emission is as follows.

1. Annihilation
2. Prompt gamma rays (except Annihilation)

The ingredients of the human body are Hydrogen, Oxygen, Nitrogen, Carbon etc., and approximately 70 % of the component is water. There are only six major channels producing the positron emitters ^{11}C, ^{13}N and ^{15}O by proton beam in human tissue as listed in Table 2.4 [78]. Those positron emitters have different half-times, and reactions in Table 2.4, which have different cross sections depending on the proton energy (Fig. 2.15). Thus the distribution of the

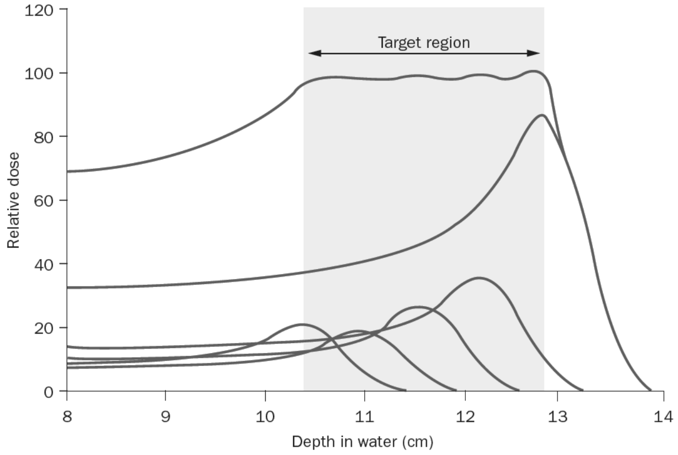

Figure 2.13: Combining proton beams with differing energies results in the summation of narrow, monoenergetic Bragg peaks into a broader, more clinically useful "spreadout" Bragg peak [76].

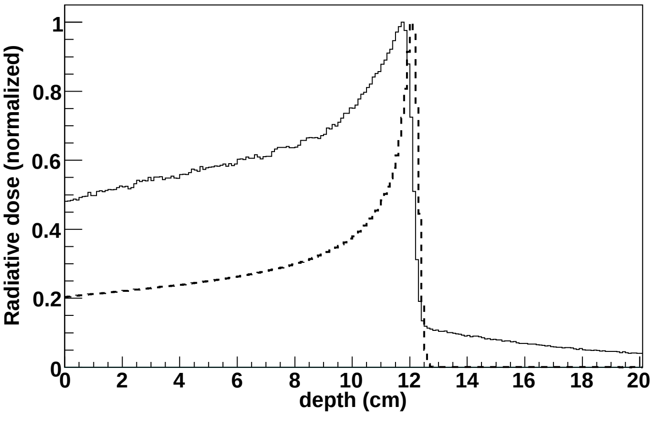

Figure 2.14: The simulated distributions of 140-MeV proton dose deposition (dotted line) and of gamma rays emitted in water in the all energy band (solid line) as a function of water depth. The detail of the simulation, which corresponds to our experiment setup is described in Chapter 5.

Table 2.4: Positron emitter production in the proton therapy

reaction	threshold [MeV]	Half-life [min]	Positron Max. energy [MeV]
^{16}O(p,pn)^{15}O	16.79	2.037	1.72
^{16}O(p,2p2n)^{13}N$^{a)}$	5.66$^{c)}$	9.965	1.19
^{14}N(p,pn)^{13}N	11.44	9.965	1.19
^{12}C(p,pn)^{11}C	20.61	20.39	0.96
^{14}N(p,2p2n)^{11}C$^{a)}$	3.22$^{c)}$	20.39	0.96
^{16}O(p,3p3n)^{11}C$^{b)}$	27.50$^{c)}$	20.39	0.96

a): (p,2p2n) is inclusive of (p,α)

b): (p, 3p3n) is inclusive of (p, αpn)

c): The listed thresholds refer to (p, α) and (p, αpn)

Table 2.5: Line gamma rays by proton interaction with organic nuclei [45].

Reaction	Transition*	Energy [MeV]	Mean time [sec]
^{12}C(p,x)^{10}B*	$^{10}B^{*0.718} \rightarrow g.s.$	0.718	1.0×10^{-9}
^{16}O(p,x)^{10}B*	$^{11}B^{*1.740} \rightarrow {}^{11}B^{*0.718}$	1.022	7.5×10^{-15}
^{12}C(p,2p)^{11}B*	$^{11}B^{*} \rightarrow g.s.$	4.44	5.6×10^{-19}
^{14}N(p,p*)^{14}N*	$^{14}N^{*5.106} \rightarrow g.s.$	5.105	6.3×10^{-12}
^{16}O(p,x)^{14}N*	$^{14}N^{*5.106} \rightarrow g.s.$	5.105	6.3×10^{-12}
^{16}O(p,p*)^{16}O*	$^{16}O^{*6.130} \rightarrow g.s.$	6.129	2.7×10^{-11}

$\star$ g.s. : Ground state.

511-keV gamma rays depends on both the incident proton energy and the elapsed time between the proton irradiation and the gamma-ray imaging.

Figure 2.16 shows the simulated distribution of linear production densities of ^{11}C, ^{13}N and ^{15}O [80], where the 511-keV gamma-ray distribution does not trace the Bragg peak. However since the PET is a very common imaging technique, the verification of the dose by 511-keV gamma rays has been studied [20].

Also other line, prompt gamma rays are generated during the proton radiation in the body. Table 2.5 lists example of the prompt lines, and Fig. 2.17 shows the simulated distribution of the depth dose and gamma rays including prompt gamma rays [81] when a water tank is irradiated with the proton beam. Although the peak of the prompt gamma-ray distribution also does not match the Bragg position, the fall-off position is matches to the Bragg position. Moreover, the gamma-ray intensity is correlated with the Bragg-peak intensity, therefore the prompt gamma-ray detector might measure also the proton beam current unlike the PET.

Figure 2.18 shows the fluence of the primary protons, secondary proton, neutron, and the total absorbed dose as a reference [74]. Around the Bragg peak, the main contribution to the absorbed dose is primary protons (from 80 to 90 %), whereas secondary protons created by primary proton-induced reactions contribute to the dose from 20 to 5 %. The secondary protons and neutrons such as recoil protons are generated by the nuclear reactions. This figure indicates that neutrons exist beyond the Bragg peak, and the gamma rays from neutrons such as 2.22-MeV

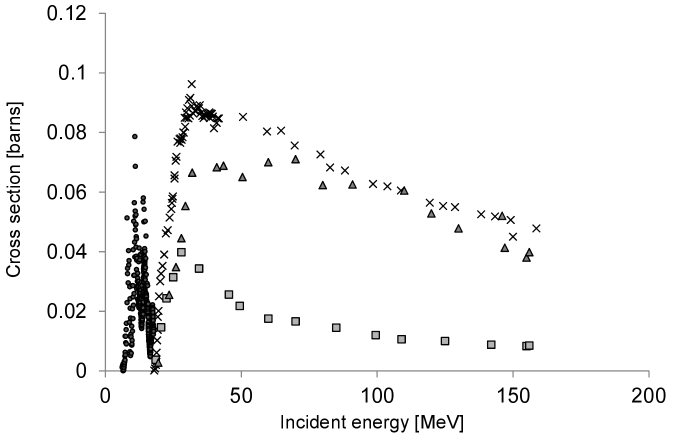

Figure 2.15: Nuclear reaction cross sections as a function of the proton energy [79]. Each mark denotes as followings: cross:$^{12}C(p,pn)^{11}C$, triangle:$^{16}O(p,2p2n)^{13}N$, square:$^{16}O(p,pn)^{15}O$, and circle:$^{14}N(p,pn)^{13}N$.

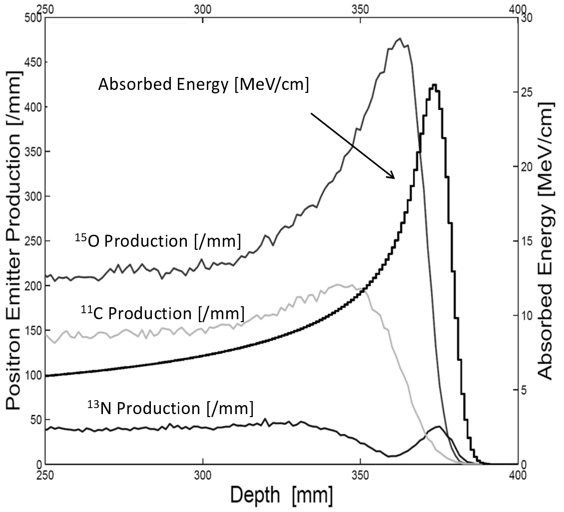

Figure 2.16: The simulation results of linear production densities of ^{11}C, ^{13}N and ^{15}O as a function of depth. The absorbed energy by the tissue is superimposed using a right-side vertical scale for comparison [80].

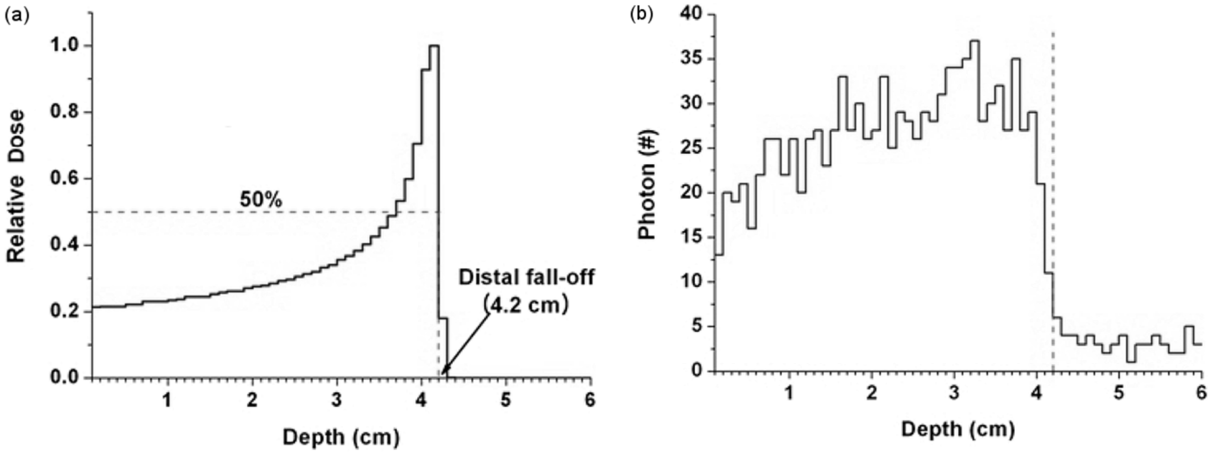

Figure 2.17: Comparison of the depth dose distribution (left) with the prompt-gamma distribution (right) for a beam energy of 70 MeV [81].

gamma rays (n-capture) is not used for the tracer of Bragg position.

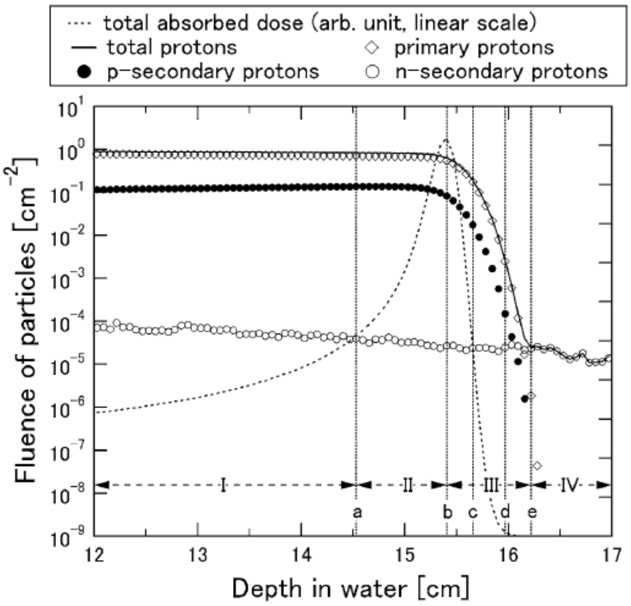

Figure 2.18: Fluences of protons as a function of depth in a water phantom per incident proton with energy of 150 MeV. (solid line) total fluence of protons; ◇ fluence of primary protons, • and ○ fluences of "p-secondary protons" and "n-secondary protons", which are generated by proton and decrease reactions. Total absorbed proton or electron dose is added for reference [74].

Chapter 3

Compton and Other Gamma-Ray Imaging

3.1 MeV Gamma-Ray Imaging Detector in Astronomy

In this section, I briefly summarize several imaging detectors onboard satellites in the sub-MeV and MeV region. Followings imaging techniques have been used for astronomy or being developed astronomy.

1. Collimator method
2. Coded aperture imaging
3. Gamma-ray lens method
4. Compton method
5. Pair-creation method

Collimator method is a simple method to select the gamma-ray direction by material shield as shown in Fig. 3.1. The narrower aperture of a collimator is necessary if a better position resolution is expected even though its field of view is small. Usually, the minimum angular resolution is several degrees under 1 MeV.

The Oriented Scintillation-Spectrometer Experiment (OSSE), which was onboad NASA's Compton Gamma-Ray Observatory (CGRO) (1991 - 2000), used the active and passive collimators. Figure 3.1 (b) shows the schematic view of the one detector of OSSE, in which there were 4 identical detectors on CGRO. The main detector is a phosphor-sandwich (phoswich) detector consisting of the NaI:Tl crystal (diameter: 33 cm, thickness: 10.2 cm) and the CsI:Na crystal (thickness of 7.6 cm). In front of the Nal:Tl crystal, a passive tungsten collimator was mounted. Around the main detector and the tungsten collimator, there was an annular shield of 8.5 cm thick NaI:Tl crystal for the anti-coincidence which is called active veto. This active veto counter efficiently rejects the gamma-ray background from the inner detector by the coincidence between inner and veto counter hitting. For the rejection of charged particles, a thin plastic scintillator

(0.6 cm thick) was also placed on the collimator. OSSE had an energy range from 0.1 MeV to 10 MeV and had a FOV of 3.8° × 11.4° (FWHM).

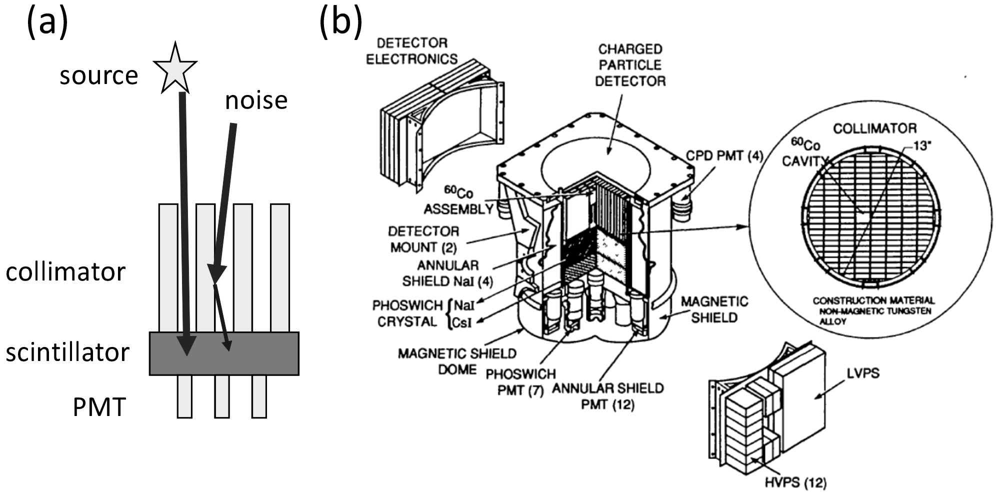

Figure 3.1: Schematic view of the gamma-ray imaging detector with the collimator (a), and OSSE (b) [41].

Coded aperture imaging camera consists of a position-sensitive photon camera and a coded mask in front of the camera (Fig. 3.2 (a)). The Coded mask has holes, which are arranged according to some rules, and the different gamma-ray sources make the different shadows owing to the holes pattern. In other words, the shadow pattern solves the gamma-ray direction by an inverse fast Fourier transform (FFT) method.

The INTErnational Gamma-Ray Astrophysics Laboratory (INTEGRAL), which is a mission of the ESA launched in 2002, has two gamma-ray telescopes with coded masks: SPI and IBIS.

The SPectrometer on Integral (SPI) is based on coded aperture imaging. The detector of SPI consists of the array of 19 Ge crystals cooled to 85 K, and thus has a good energy resolution of 2 keV for 1 MeV. The mask of SPI is made by a 3 cm thick tungsten plate, and the distance between the mask and the detector is 1.71 m. The whole detector is surrounded by the 511-kg active BGO shield viewed by 181 PhotoMultiplier Tubes (PMT). Due to the high energy resolution, the SPI's sensitivity for narrow-line gamma-rays is improved at least by a factor of 10 better than other gamma-ray telescopes.

Also, the Imager on Board of the Integral Satellite (IBIS) uses a coded aperture imaging. The coded mask of IBIS is a 16 mm thick tungsten mask. The detector consists of 2 layers. The lower layer is the array of 4096 CsI scintillators viewed by the silicon PIN photodiodes (each CsI size: 9 cm×9cm ×30 cm, total area: 3318 cm^2), named PICsIT. The upper layer is the array of 16384 CdTe pixels (pixel size: 4cm×4cm×2 mm, total area: 2621 cm^2), named ISGRI. ISGRI detects from 15 keV to 400 keV, and PICsIT covers from 200 keV to 10 MeV. The detector

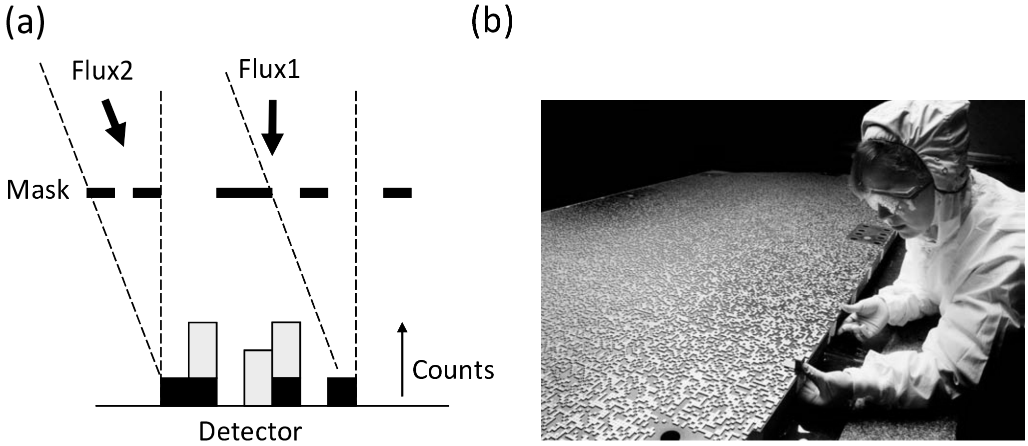

Figure 3.2: Schematic view of the Coded aperture imaging (a) [82], and photograph of Coded Mask in Swift/BAT (b) [83].

layers are surrounded by the BGO active shield, and a passive tungsten collimator is placed between the mask and BGO shield. The distance between the tungsten mask and the upper layer detector is 3.2 m, so that IBIS has a good angular resolution of 12 arc sec.

In addition, Burst Alert Telescope (BAT) loaded on Swift satellite consists of 2.7-m^2 area mask made from lead (Fig. 3.2 (b)) and a CdZnTe detector with a size of 4 mm ×4 mm ×2mm. BAT has an energy dynamic range of 15-150 keV, and a half-coded field of view of 1.4 str.

Here, both collimator and coded aperture except BAT/Swift imaging are required with veto counters surrounding the detector for background rejection, and therefore, the whole detector system becomes so heavy. In addition, when a mask is placed at a longer distance from the photon detector, the angular resolution is better up to a few arcmin, while more photon events are required to keep an image quality. Therefore, only bright objects are imaged using a coded mask detector with a good-angular resolution.

Gamma-ray lens method is a new technique to detect the focused gamma rays using Bragg reflection as shown in Fig. 3.3. Owing to use of Bragg reflection, the energy band is narrow than other detectors, and the focus length is so long. For example, CLAIRE experiment, which is the balloon-born experiment in 2001, had an energy band of 169 - 171 keV, an energy resolution of 2 keV at 170 keV (FWHM), and a focus length of approximately 2.8 m. However, the field of view was quite narrow $45''$ [84]. Here, when a detector has an energy range of a few hundred keV, the focus length should be $\sim$ 100m, Although the lens method is expected to be an excellent the position and energy resolution, which is suitable for a pointing observation, we must resolve difficult techniques such as formation flight between a lens and a photon detector in the space.

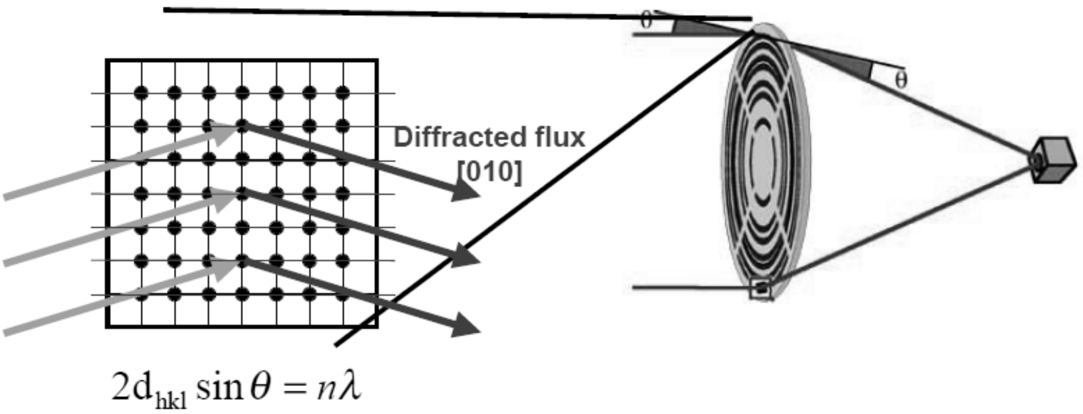

Figure 3.3: Schematic view of gamma-ray lens [85].

Compton imaging uses a Compton scattering which is a main interaction with the matter in the sub-MeV and MeV regions. The COMPTEL based on classical Compton imaging, which was onboad CGRO, was the first Compton telescope onboard a satellite. The schematic view of COMPTEL is shown in Fig. 3.4. The low-Z detector of it was a liquid organic scintillator NE213A (geometrical area: 4188 cm^2), and the high-Z detector was a NaI(Tl) crystal (geometrical area: 8744 cm^2). Although each detector was surrounded by an anti-coincidence counter dome for the rejection of charged particles, the veto counter for gamma rays is not used. For the background rejection, COMPTEL used the time of flight (TOF) technique. COMPTEL had an FWHM angular resolution of 1 - 3° typically for 0.75 - 30 MeV gamma-ray [42]. In addition, the energy resolution and the field of view were 5-10% and $\sim$ 1 str (FWHM), respectively, at 0.75-30 MeV.

The Energetic Gamma-Ray-Experiment Telescope (EGRET) aboard CGRO was based on a pair-tracking imaging detector. The schematic view of EGRET is shown in Figure 3.5. The EGRET consisted of a spark chamber for direction measurement, an anti-coincidence counter as a veto counter, and a NaI(Tl) calorimeter. The spark chamber had interleaved tantalum foils and tracking layers. The trigger counter had the plastic scintillator sheets inserted into the lower part of the spark chamber, and the thickness of the NaI(Tl) crystal was 20 cm. For the rejection of charged particles, the anti-coincidence hood with the 2 cm thick plastic scintillator surrounded the spark chamber.

Here, EGRET detected approximately 270 steady gamma-ray sources in the GeV region, while COMPTEL detected only approximately 30 steady sources in the MeV region. The reason is probably that COMPTEL could not reject backgrounds completely by the TOF of both detectors even though the sub-MeV and MeV bands have much larger backgrounds than the

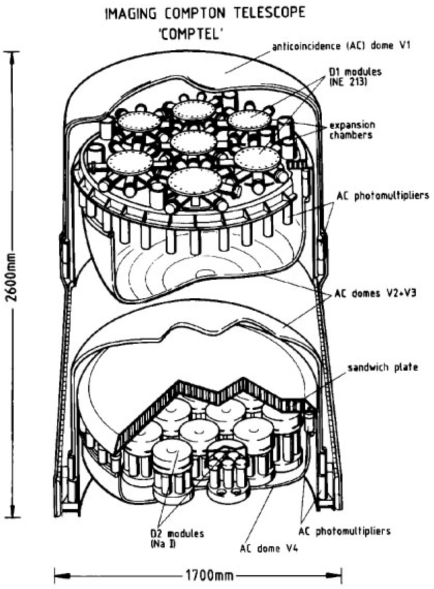

Figure 3.4: Schematic view of COMPTEL [42].

GeV band. Actually, COMPTEL had various backgrounds as shown in Figure 3.6, of which details were described in [86]. Each process is:

A Internal Single Photon: Gamma rays, produced at the inside of the detector by neutron capture or by radioactive isotopes (like ^{40}K), may make Compton scattering in the forward detector, and its scattered gamma-rays are absorbed in the backward detector.

B External Single Photon: Gamma rays are produced at other detectors or the satellite platform by neutron capture, decay of radioactive isotopes and scattering, and then they may make Compton scattering in the forward detector and its scattered gamma-rays are absorbed in the backward detector.

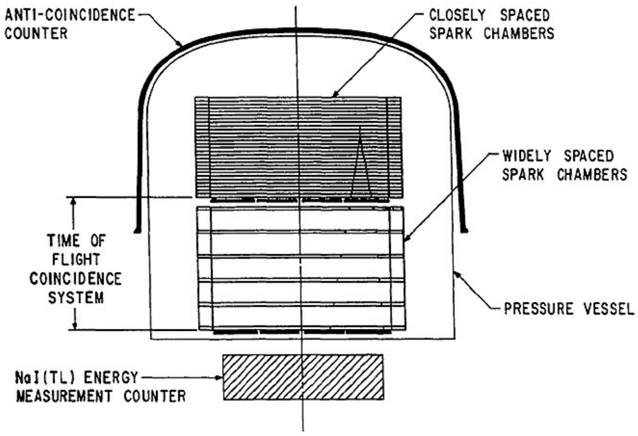

Figure 3.5: Schematic view of EGRET [41].

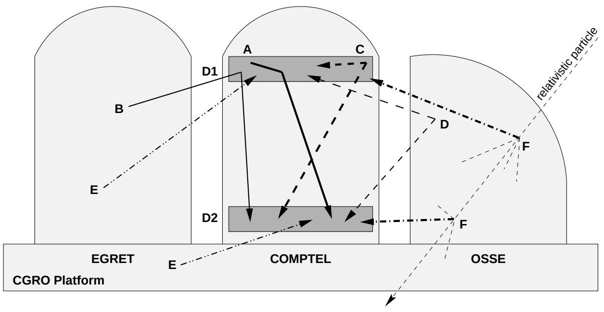

Figure 3.6: Various background of COMPTEL [86].

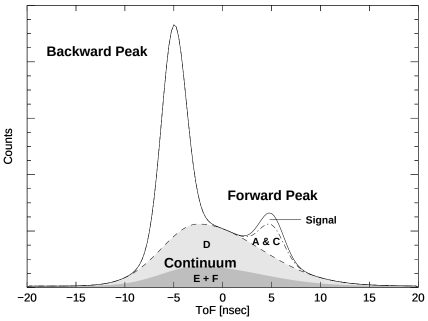

Figure 3.7: TOF distribution [86].

C Internal Multi-photon: Multi-photons are produced by the interactions, such as $^{27}\mathrm{Al}(n,\alpha)^{24}\mathrm{Na}$ or $^{27}\mathrm{Al}(n;n',\cdots)^{27}\mathrm{Al}$. Then some photons may hit the forward detector and also the backward detector simultaneously.

D External Multi Photon: In other detectors or the satellite platform, some gamma rays may be created by the same processes of C, and some photons may hit the forward detector and also the backward detector simultaneously.

E Random Coincidence: Sometimes, the different photons produced by the independent interactions hit the forward detector and also the backward detector accidentally.

F Cosmic-Ray Interaction: It interacts with material at the different positions, generates some photons simultaneously, when cosmic rays come into the satellite. Then those photons hit both the forward and backward detectors.

G Other Process: As the other backgrounds, neutron, electron and atmospheric gamma-rays were measured.

For the background rejection, COMPTEL used the time of flight (TOF) between the low-Z detector and the high-Z detector. Figure 3.7 shows the distribution of TOF by simulation. Although the most events are backward events in which gamma-ray interacts in the backward detector and then in the forward detector, these events can be easily rejected using the timing above 1 MeV. However D, E and F events make continuum components, and the forward peak includes the one third of them. Since the interaction of A and B events are the real Compton interaction, they are the intrinsic background and hardly be rejected. Moreover, if there is a decay in the forward detector, C events have no difference with celestial gamma rays in TOF distribution. Therefore, even if we pick up the forward peak, the most of the selected events are still due to background events as shown in Figure 3.7.

From the reason described above, the actual sensitivity of COMPTEL was lower than the design sensitivity. However, in the MeV region where the main interaction of photon with matter is Compton scattering, the most suitable method with better sensitivity is Compton imaging. In fact, in the MeV region, COMPTEL with Compton imaging had a better sensitivity than

SPI and IBIS with coded aperture imaging as shown in Fig. 3.8, which shows the sensitivities of several detectors launched so far for the continuum spectrum. However, the sensitivity of COMPTEL is worse by two orders of magnitudes than that in the X-ray and GeV gamma-ray bands. In order to obtain the better sensitivity for the all sky-survey in the sub-MeV and MeV region, we should use the Compton imaging method, and the incident gamma-ray direction is determined by not accumulating some photons, but a single photon.

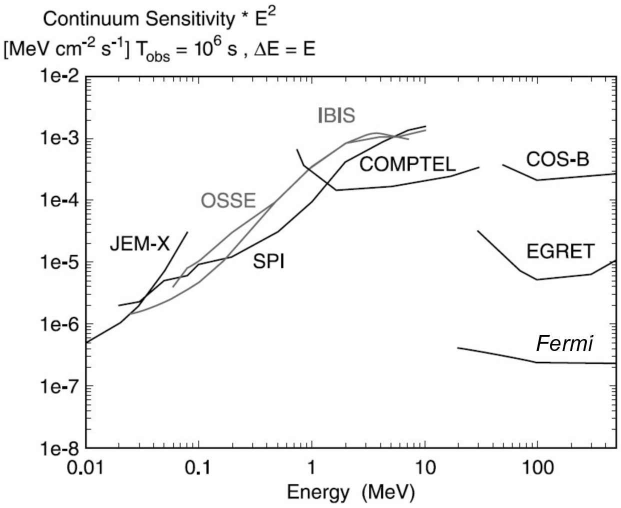

Figure 3.8: Continuum sensitivities of X/Gamma-ray observatories [87].

3.2 MeV Gamma-Ray Imaging Detector in Medical Imaging

For medical imaging, two detectors are used generally. The first is Single photon emission computed tomography (SPECT) using a collimator method. The part of the photon detector commonly consists of scintillator. Figure 3.9 (a) shows the schematic view of the SPECT, and double and triple-SPECT are also used in the medical imaging in order to obtain the higher sensitivity as shown in Fig. 3.9 (b,c). SPECT has a typical spatial resolution of $\sim 4-6$ mm (FWHM) depending on the size of the collimator aperture, and an available energy dynamic range is approximately $80-300$ keV by changing the collimators (fine collimator of ~ 4 mm resolution in ≤ 200 keV) [88]. The energy range is limited by background from collimator with Compton scattering and the penetration of higher energy gamma rays.

The other is a Positron emission tomography (PET). Figure 3.10 shows the schematic view of PET which consists of pairs of segmented detector on the opposite side. Using the pair detector, back-to-back 511-keV gamma rays from a positron-emitting RI are detected. The position of the positron-emitting RIs is obtained by the crossing point of several back-to-back gamma-ray lines. PET has been able to image three-dimensionally by moving the detector along the axis

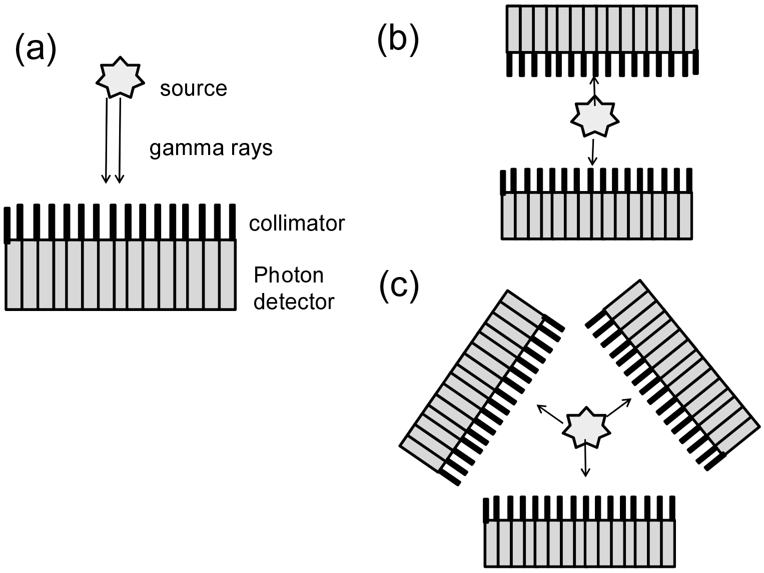

Figure 3.9: Schematic view of (a) one- (b) double- (c) triple- SPECTs.

Table 3.1: Calculated positron range [89].

positron emitter	^{18}F	^{11}C	^{13}N	^{15}O
FWHM [mm]	0.102	0.188	0.282	0.501
FWTM* [mm]	1.03	1.86	2.53	4.14

$\star$ FWHM: full width at tenth maximum.

of the body. Commonly, as the segmented detector, scintillator is used due to a high stopping power.

Here, the FWHM spatial resolution of the PET $\Delta x/x$ has a principle limit as described following equation:

$$\Delta x/x = \sqrt{\left(\frac{d}{2}\right)^2 + r^2 + b^2 + (0.0022D)}, \tag{3.1}$$

where d, r, b, and D denote the dimension of the square face of a crystal, positron range, a segmented scintillator size (block effect), and diameter of the PET (non-collinearity), respectively.

Positron range depends on the radio isotopes which have different energies, and the range belongs to Bethe-Bloch formula. Figure 3.11 shows a calculated distribution of positron-annihilation positions in water projected onto a plane for ^{18}F and the distribution profile 3.11 [89]. Table 3.1 lists the positron range for several positron emitters.

The block effect b represents the uncertainty associated with identifying individual crystals with secondary detection devices such as photomultiplier tubes. This factor typically contributes only a fraction of a millimeter to the spatial resolution. Non-collinearity is to have an error in the angle between the back-to-back gamma photons, because of the probability of positrons annihilating while in motion. For the large-size PET for human body, the non-collinearity effect

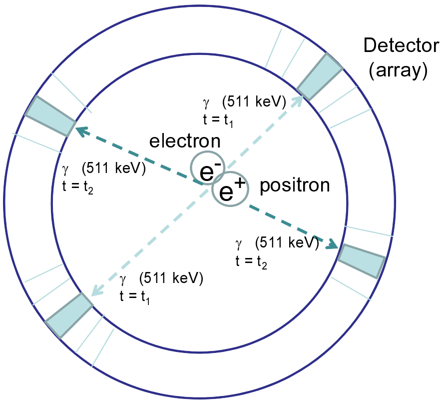

Figure 3.10: Schematic view of PET. Back-to-back gamma-ray emission at the same time ($t = t_1$ or t_2) are detected.

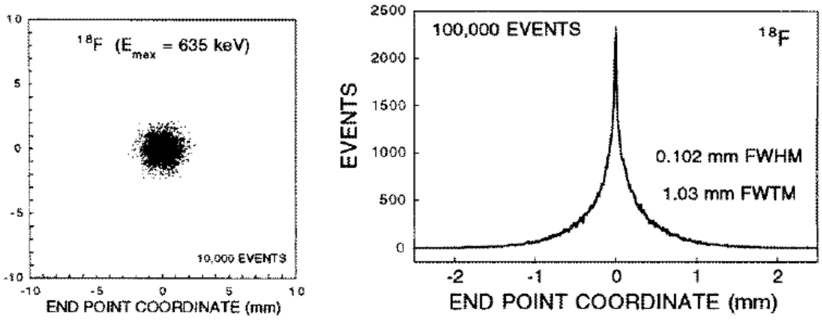

Figure 3.11: Calculated distribution of positron annihilation from ^{18}F source in water phantom (left), histogram of x coordinates from positron annihilation point distribution (right) [89].

is not negligible. Thus the typical spatial resolution for the human PET is $\sim$ 5 mm (FWHM), and small PET for the animal has a better spatial resolution of $\sim$ 2 mm (FWHM).

For medical requirement, the spatial resolutions of the SPECT and PET are sometime not sufficient. To recover the resolution of the PET and SPECT, usually in the medical diagnosis, X-ray CT or magnetic resonance imaging (MRI) also is used for the compensation.

The SPECT and PET have a narrow energy dynamic range, and available RIs is limited. If an imaging detector with a wide-energy dynamic range is available, it is possible to choice various RIs. For example, zinc is necessary to divide cells, and a ^{65}Z (1116 keV) ion might trace the position of growing up in the living body such as root in the plant or tumor [90, 91]. In addition, the wide energy range enables us to obtain a multi-RIs imaging simultaneously. Table 3.2 shows the RIs which are used at present or expected to be put to practical use for the medical imaging.

Table 3.2: Example of RIs for the imaging

IR	^{133}Ba	^{131}I	^{198}Au	^{22}Na	^{18}F	^{54}Mn	^{65}Zn	^{59}Fe
energy [keV]	354	364	412	511, 1275	511	835	1116	1099, 1292

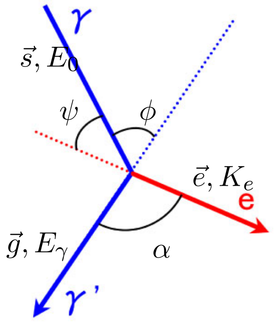

Figure 3.12: Parameters in Electron Tracking Compton Imaging

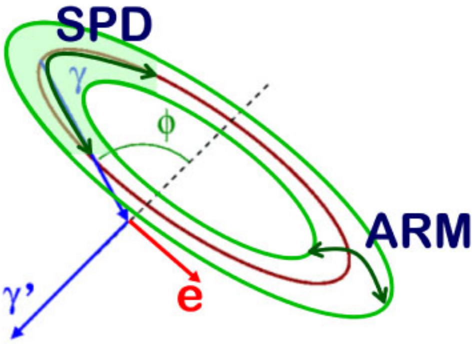

Figure 3.13: Definition of ARM & SPD

To obtain a wide energy dynamic range, a Compton camera has been studied for medical imaging so far [92, 93, 94]. However, most studies are still at simulation steps, and their Compton cameras were a classical imaging type. On the other hand, our electron-tracking Compton camera, as described in next section and Chapter 4, succeeded in obtain the animal imaging with RIs.

3.3 Electron-Tracking Compton Imaging

The electron tracking Compton imaging measures both the energies and the directions of the incident gamma-ray by obtaining with the energy and direction of the scattered gamma photon and the recoil electron. In Fig. 3.12, the energy and direction of the scattered gamma-ray are E_γ and $\vec{g}$, the energy and direction of the recoil electron are K_e and $\vec{e}$, the scattering angle is ϕ, the recoil angle is ψ and the differential angle between $\vec{g}$ and $\vec{e}$ is α, where $\vec{g}$ and $\vec{e}$ are the unit vectors. Then, the incident energy E_0 and the incident direction $\vec{s}$ of the initial gamma-ray are described, respectively:

$$E_0 = E_\gamma + K_e, \tag{3.2}$$

$$\vec{s}_{\mathrm{rcs}} = \left(\cos\phi - \frac{\sin\phi}{\tan\alpha}\right)\vec{g} + \frac{\sin\phi}{\sin\alpha}\vec{e}, \tag{3.3}$$

$$= \frac{E_\gamma}{E_\gamma + K_e}\vec{g} + \frac{\sqrt{K_e(K_e + 2m_ec^2)}}{E_\gamma + K_e}\vec{e}. \tag{3.4}$$

where the scattering angle is ϕ, which is written as follows,

$$\cos\phi = 1 - \frac{m_ec^2}{E_\gamma + K_e}\frac{K_e}{E_\gamma}, \tag{3.5}$$

and the recoil angle ψ is

$$\cos\psi = \left(1 + \frac{m_e c^2}{E_\gamma + K_e}\right)\sqrt{\frac{K_e}{K_e + 2m_e c^2}}. \tag{3.6}$$

The differential angle α between $\vec{g}$ and $\vec{e}$ is described by the definition:

$$\cos\alpha_{\mathrm{geo}} = \vec{g}\cdot\vec{e}. \tag{3.7}$$

On the other hand, α is described with E_γ and K_e by the Compton kinematics:

$$\cos\alpha_{\mathrm{kin}} = \left(1 - \frac{m_e c^2}{E_\gamma}\right)\sqrt{\frac{K_e}{K_e + 2m_e c^2}}. \tag{3.8}$$

The angle α is a characteristic parameter of the electron tracking Compton imaging. The α makes it possible to select the Compton scattering events from the backgrounds. The α is obtained from the equation (3.7) and (3.8), where (3.7) depends on only the geometrical information, and (3.8) depends on only the kinematic information. Thus, the α_{geo} is independent from the α_{kin}. For this reason, we can select good events, in which Compton the scattering occurs in the tracker and scattered photon is absorbed perfectly in the absorber, by requiring the follows

$$\alpha_{\mathrm{geo}} = \alpha_{\mathrm{kin}}. \tag{3.9}$$

In the Electron Tracking Compton Imaging, the accuracy of the event reconstruction is estimated using two parameters. One is the Angular Resolution Measure (ARM), which is the accuracy of the scattering angle:

$$\Delta\phi_{\mathrm{ARM}} = \arccos\left(\vec{s}\cdot\vec{g}\right) - \arccos\left(1 - \frac{m_e c^2}{E_\gamma + K_e}\frac{K_e}{E_\gamma}\right). \tag{3.10}$$

The other is Scatter Plane Deviation (SPD), which is the accuracy of the determination of the scattering plane:

$$\Delta\nu_{\mathrm{SPD}} = \mathrm{sign}\left(\vec{g}\cdot\left(\frac{\vec{s}\times\vec{g}}{|\vec{s}\times\vec{g}|}\times\frac{\vec{s}_{\mathrm{rcs}}\times\vec{g}}{|\vec{s}_{\mathrm{rcs}}\times\vec{g}|}\right)\right)\arccos\left(\frac{\vec{s}\times\vec{g}}{|\vec{s}\times\vec{g}|}\cdot\frac{\vec{s}_{\mathrm{rcs}}\times\vec{g}}{|\vec{s}_{\mathrm{rcs}}\times\vec{g}|}\right). \tag{3.11}$$

where $\vec{s}$ is the real direction, and $\vec{s}_{\mathrm{rcs}}$ is the reconstructed direction of the incident gamma-ray. Thus, the error region of one event is a sector shape, as shown in Fig. 3.13.

In the previous sections, we assume that gamma-ray photon scatters with a free electron. That process is called unbound Compton scatter. However, in actual detectors, electrons are bounded in the potential energy of the nuclear or molecular orbits. Thus, electrons have a kinematic energy before the Compton scattering.

In Compton imaging, the scattering angle is obtained by the energy of scattered gamma-ray and the energy of recoil electron. Therefore, the accuracy of the scattering angle (ARM) is certainly affected by Doppler broadening, and Doppler broadening makes the intrinsic limit for the angular resolution of the ARM.

Since Doppler broadening is caused by the motion of the electron before the scattering, the energy distribution of scattered gamma-ray is changed at which orbit the electron recoils. Figure

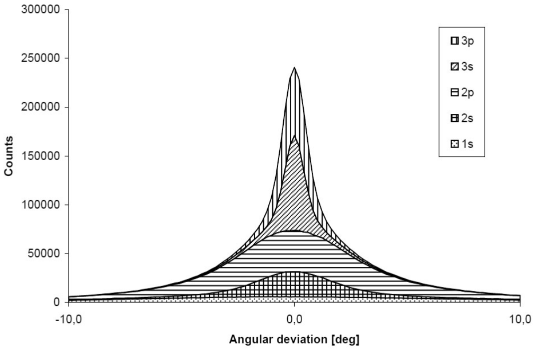

Figure 3.14: The ARM distribution of each electron orbit ($E_0 = 200\text{keV}$, Si) [95]

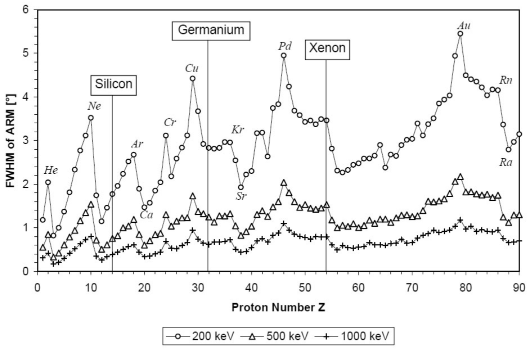

Figure 3.15: The Z dependence of the ARM [95]

3.14 shows the uncertainty of the ARM of each orbit. Because the electron at the outer orbit has the lower kinematic energy, the effect of Doppler broadening is smaller, and the uncertainty of the ARM is the smaller. The dependence of the uncertainty of the ARM on Z is shown in Fig. 3.15. Figure 3.16 shows the energy dependence of Doppler broadening. The energy of an incident gamma-ray is higher, the effect of Doppler broadening is smaller because the initial energy of an electron is smaller enough.

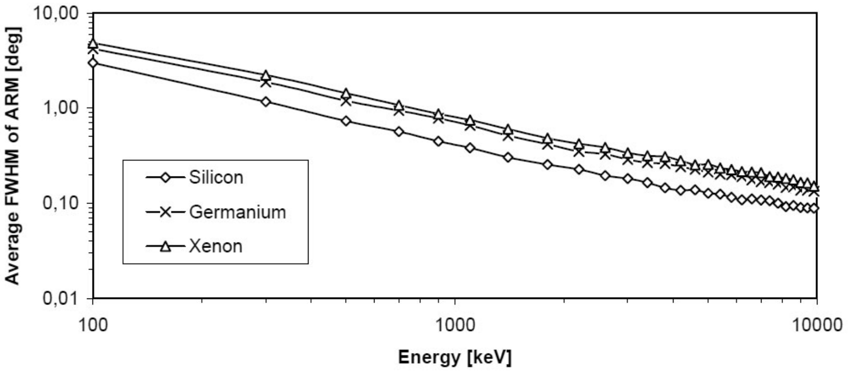

Figure 3.16: The energy dependence of Doppler broadening [95]

Due to the Doppler broadening, the gaseous detector has an advantage of the use for converter of the Compton camera than solid state detector such as semi-conductor. In addition, the gaseous detector have a better capability of electron-tracking than a solid state. Although, the density of solid is higher by an order of 3 than that of gas, a gaseous detector including a micro pattern gas detector is easy to expand the volume with a low cost. On the other hand, as an absorber, scintillator has better stopping power than semi-conductor.

Our aim to develop the ETCC is obtaining the higher sensitivity by a factor of 10 than CGRO. For the first step, we demonstrated the balloon-bone experiment in 2006, and we acquired the cosmic and atmospheric gamma-ray photons as expected. This balloon-bone experiment and the previous studies suggest the feasibility of being our expected sensitivity. Also our ETCC also has been applied to medical imaging. In fact, we have already demonstrated a RI imaging with small animals as the target. Since the ETCC is thus expected to useful for various applications, we have developed an ETCC with the improvement of performances such as detection efficiency and angular resolution.

Chapter 4

Gaseous TPC and Scintillator

4.1 μ-PIC (Micro Pixel Chamber)

The ETCC consists of a gaseous time projection chamber (TPC) as a converter, and a scintillator as an absorber. One of the features in the ETCC is to measure three-dimensional electron track in the TPC, which needs an enough position resolution of several hundred μm and time resolution of ~ 10 nsec Thus, we have developed a μ-TPC consisting of a micro pattern detector (μ-PIC), and a Gas Electron Multiplier.

Micro Pixel Chamber (μ-PIC) is a one of Micro Pattern Gaseous Detector (MPGD) [97]. Figure 4.1 shows the schematic view of μ-PIC. The μ-PIC has a pixel electrode like a sliced proportional counter. The substrate is made by polyimide, and the electrodes are Cu coated with Ni. μ-PIC is manufactured by the print circuit board technology, and thus the device with a very large area can be easily developed. Actually, a large μ-PIC with an area of 30 cm $\times$30 cm is already applied to several fields. Each pixel is aligned with the pitch of 400 μm. μ-PIC has ~ 65000 pixels in an area of 10 cm $\times$10 cm and $\sim 6 \times 10^5$ pixels in an area of 30 cm $\times$30 cm, respectively. The anode and cathode electrodes are connected on the strip, respectively, and these electrodes run perpendicularly. Therefore, μ-PIC has a 2 dimensional position sensitivity with a fine position resolution.

The small pixel structure causes a high gas gain (20000 at maximum, and 6000 in stable operation) and a long stability (with gain of 5000 for several years by exchanging the gas once

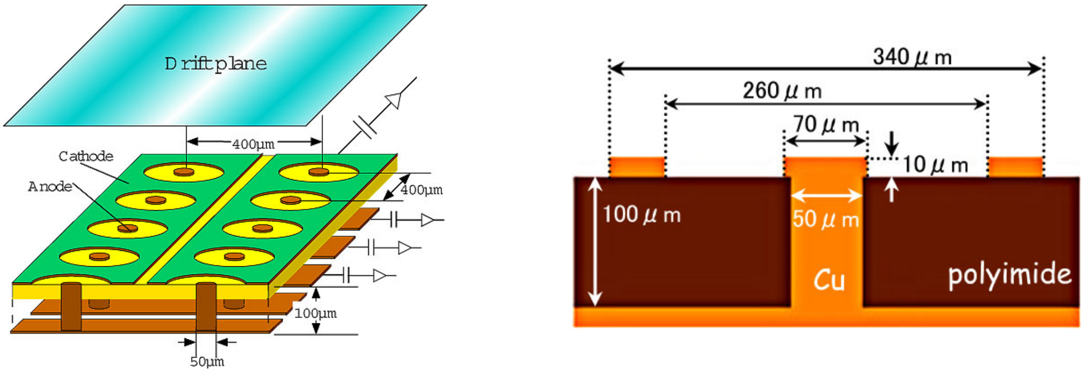

Figure 4.1: The structure of μ-PIC (left), and the cross section of the anode and cathode (right).

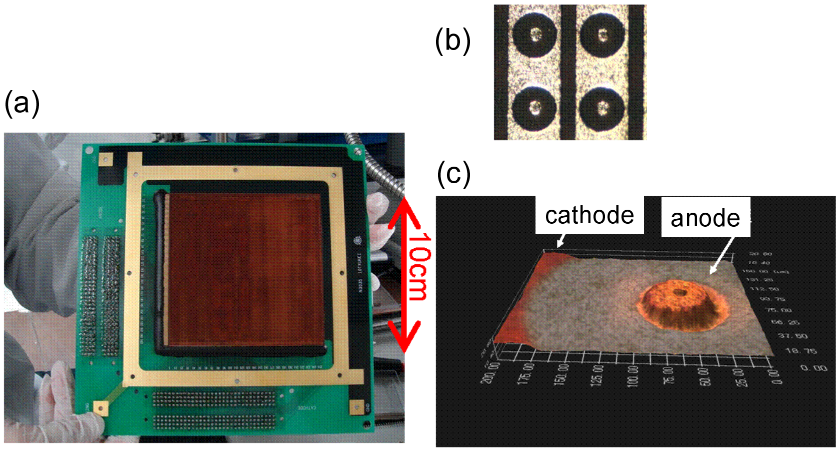

Figure 4.2: (a) Photograph of 10 cm ×10 cm μ-PIC. (b) and (c) are micrographs of anode and cathode.

approximately 1-2 month), because the pixel electrode is hardly damaged by discharge, which was a serious problem for micro strip gaseous chambers. Also μ-PIC is able to work under a high intensity of $\sim 10^7$ count/(sec mm^2) by the smallness of the pixel.

Since a μ-PIC has a lot of readout strips (a 10 cm ×10 cm μ-PIC has 512 ch, and a 30 cm×30 cm μ-PIC has 1536ch), we have developed a readout system for μ-PIC. The schematic view of this system is shown in Fig. 4.3.

Each of all strips connects to a preamplifier chip one-by-one, and the amplifier feeds both an analog signal and a discriminated digital signal. The analog signal is summed with every 16 channels on the board, and the wave form is digitized by Flash ADC (FADC) or Charge ADC. On the other hand, discriminated digital signals are sent to the position encoding module consisting of Field Programmable Gate Arrays (FPGA) with an internal clock of 100 MHz. The FPGA calculates the anode and cathode coincident position within one clock interval (10 ns), and here we say "position encoding mode-I". The number of the hit electrode is sent from the position encoder to a memory module ("VME Memory Board TMB-2" produced by ARKUS) on a VME system. We applied the low threshold level for 25 mV (corresponding to 3.6 mV at the comparator input) supplied to the ASDs. Then input charges sometimes cause the propagation delay at the comparator output. This propagation delay is the main reason for the counting loss due to the narrow coincidence of 10 nsec. Thus, the small gain variation leads to non-uniformity of the signal detection efficiency. Then we have improved a novel position encoding, mode-II, which measures all but points of both of anodes and cathodes without coincidence. Then the coincident position is calculated at the off-line [98]. Although we used mode-II, in the off-line analysis, we selected only coincident event within one clock interval as the same as mode-I,

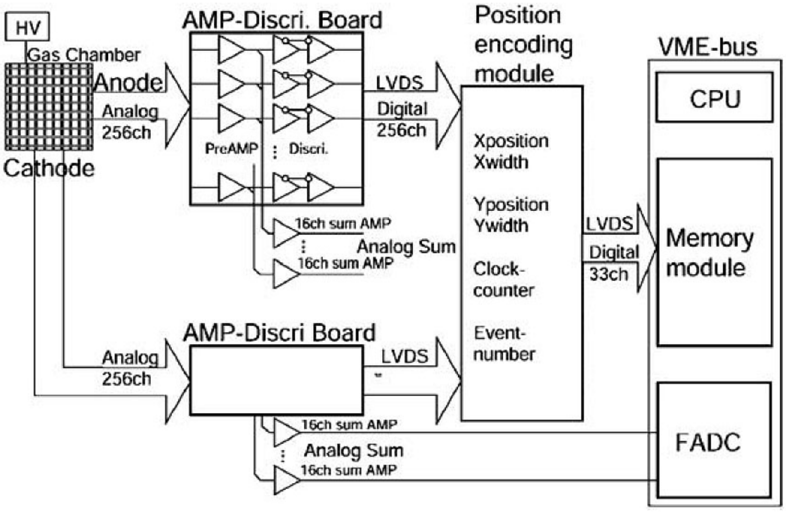

Figure 4.3: Data Acquisition System for μ-PIC [28]

because an analysis method for mode-II is not completed.

As a preamplifier for μ-PIC, we use ASD (Amplifier-Shaper-Discriminator) chips, which were developed by KEK for Thin Gap Chamber of ATLAS experiment in LHC at CERN [99]. The ASD chip has 4 input lines per 1 chip. Each line has a preamplifier, main-amplifier, discriminator, analog output and digital outputs. The preamplifier has a time constant of 16 nsec, and the analog signal is an output of this preamplifier. The digital outputs are the discriminator outputs in LVDS.

The gas gain of μ-PIC is shown in Fig. 4.4, where μ-PIC has a maximum gain of $\sim$ 20000. Also μ-PIC have realized a good stability with the gain of $\sim$ 6000 for more 1000 hours. Thus, μ-PIC is a stable detector with a high gas gain.

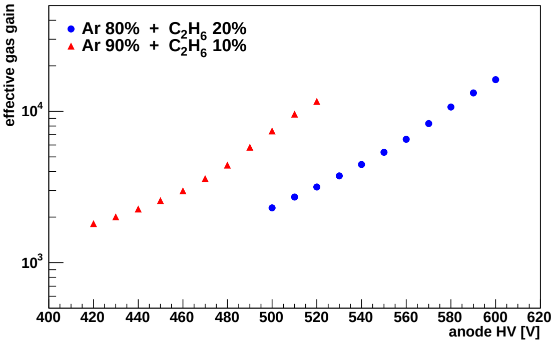

Figure 4.4: Effective gas gain as a function of the anode voltage (SN040223-1) [96].

Since a 10 cm ×10 cm μ-PIC has 65536 pixels (= 256 ch × 256 ch) and a 30 × 30 cm^2 one has 589824 pixels (= 768 ch × 768 ch). The non-uniformity of the pixel structure causes a non-uniformity of the gain on μ-PIC.

Figure 4.5 shows the gain map of the 10 cm ×10 cm μ-PIC. The Root Mean Square (RMS) of the gain variation on the whole area is $\sim$ 5 %, which surely indicates that μ-PIC has a good uniformity. On the other hand, Figure 4.6 shows the gain map for the 30 cm ×30 cm μ-PIC. The ratio of the gain between the minimum gain area and the maximum gain area is 2.2, and the gas gain uniformity is 16.7 % at the RMS.

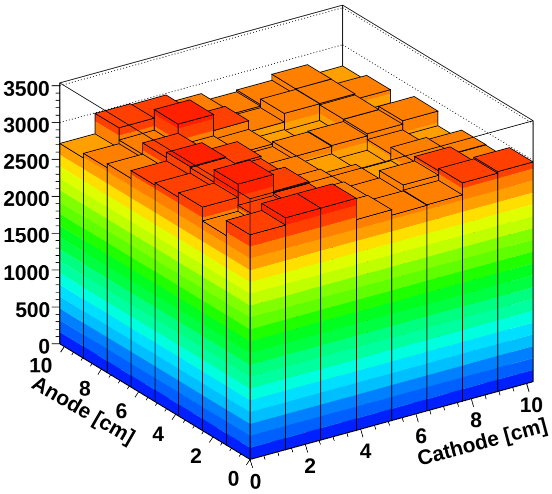

Figure 4.5: Effective gain map of 10 cm ×10 cm (SN040426-1) [96].

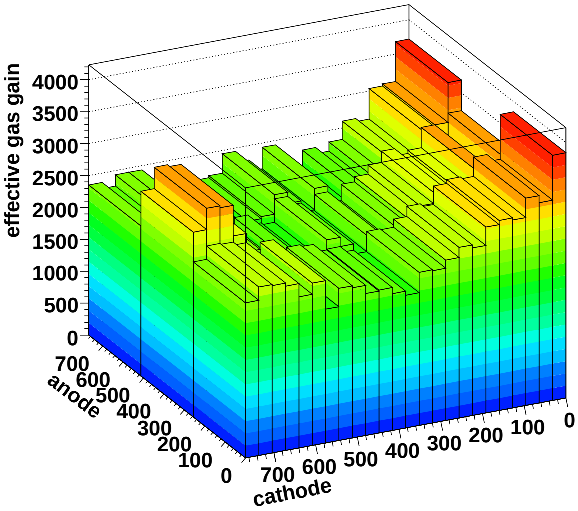

Figure 4.6: Effective gain map of 30 cm ×30 cm (SN041129-1) [96].

μ-PIC is used as an X-ray imaging detector. Figure 4.7 shows a spectrum of ^{55}Fe measured by 10 cm ×10 cm μ-PIC. The energy resolution for X rays of 5.89 keV is 30 % at FWHM for the whole area. Figure 4.8 is an X-ray image of a test chart irradiated by the X-ray generator where the shadow of 2 slits per 1mm can be distinguished clearly. Using the image of the edge of this test chart, we obtained the position resolution is $\sim$ 120 μm at σ. This value is quite equal to the predicted one from statistics, which is $\frac{400\mu\mathrm{m}}{\sqrt{12}} \simeq 115$ μm.

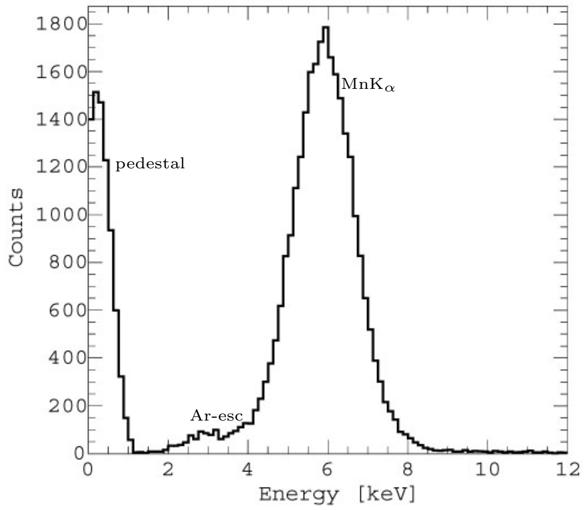

Figure 4.7: Spectrum of ^{55}Fe (whole area of 10 cm ×10 cm: Ar 90 % + C_2H_6 10 %, 1 atm).

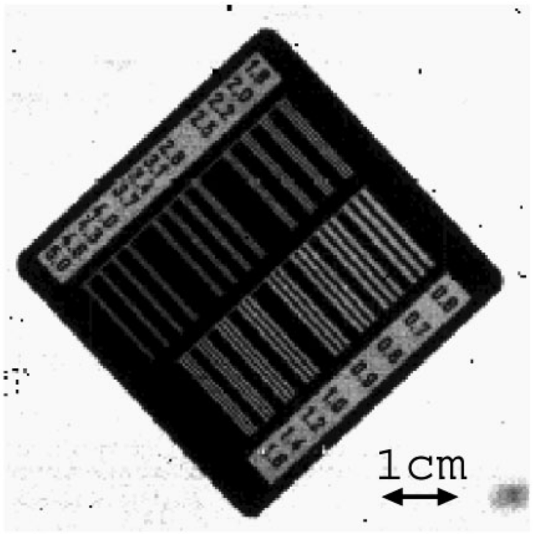

Figure 4.8: X-ray imaging of a test chart with 10 cm ×10 cm μ-PIC [26].

4.2 Gas Electron Multiplier

In order to obtain the three-dimensional track of the electron in Compton scattering, the tracking capability for a Minimum Ionizing Particle (MIP) is required at least. The energy deposit of a MIP in the argon gas is 2.54 keV/cm at the normal pressure, in which a MIP makes approximately 3.9 electrons per 400 μm. For the detection of MIP tracks, we must detect such few electrons in one pixel. Although the detection of MIP is needed with a high gas multiplication of 2×10^4 at least with the μ-PIC system, the stable gas gain of μ-PIC is only approximately 6×10^3. Then we use a Gas Electron Multiplier (GEM) [31, 32] to compensate this gain gap.

A GEM has been developed by Sauli and other groups, which is a polyimide foil with Cu-plated electrodes at both sides as shown in Fig. 4.9. A GEM foil has a lot of small holes as shown in right of the figure. If the different voltage are supplied to Cu electrodes on both sides, a strong electric field is generated inside of this hole. When the seed electron drifts into this hole, the gas multiplication is caused in such a strong electric field. The foil is very thin with a thickness of 50 μm and consists of the low-Z material. But the distance of both electrodes is too short for a GEM foil to get a high gain alone, and hence the typical gain of single GEM is approximately 100.

We used this GEM foil as a pre-multiplier for μ-TPC. A seed electron is multiplied by a

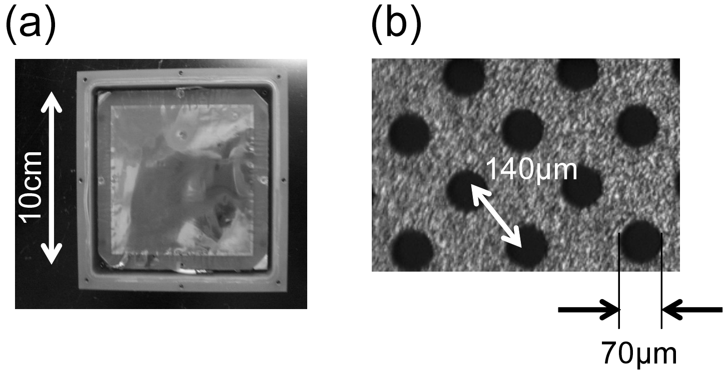

Figure 4.9: The photograph and microphotograph GEM. The hole diameter is 70 μm, and the pitch of holes is 140 μm.

strong-electric field between the hole of the GEM ($\sim$ 5 kV/cm) with a gain of approximately 10 (Fig. 4.10). After that, the multiplied electrons travel into μ-PIC, and second multiplication is caused by μ-PIC with a gain of thousands. Therefore, we can take an enough signal with a gas gain of above 2×10^4 . Figure 4.11 shows the gas gain of the GEM + μ-PIC system (Fig. 4.10).

4.3 Time Projection Chamber with μ-PIC (μ-TPC)

When a charged particle passes through a gas, the gas around the particle track is ionized, in which a group of ionized electrons are called "electron cloud". If an adequate electric field in the gas are applied from the drift space to the μ-PIC, the electron cloud drifts along the electric field. At this time, the drift time from the ionization point to the termination on the anode can be transferred to the distance between the ionization point and the termination point. Therefore, if we know the start timing of the drift, the distance between the ionization point and the anode (z-position) is measured by the drift time. Such a system is called a Time Projection Chamber (TPC). A two-dimensional detector, for example a Multi Wire Proportional Chamber (MWPC), is usually used to obtain x, and y positions, and the TPC can measure three-dimensional positions of a track of a charged particle.

μ-PIC is a two-dimensional gaseous detector, and is surely used as a readout detector of the TPC. A TPC with μ-PIC is called μ-TPC, and the schematic view is shown in Figure 4.12. In our advanced Compton camera, this μ-TPC is used as a tracker, which detects a fine recoil track of a recoil electron.

The electron drift velocity v is described such as:

$$v_{-} = \frac{eE}{m_e}\tau, \tag{4.1}$$

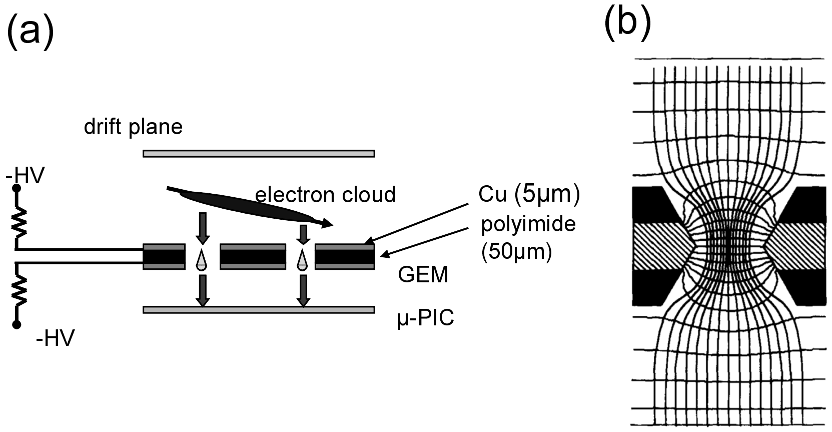

Figure 4.10: Schematic view of the GEM + μ-PIC system (a), and the line of electric force in the GEM hole (b).

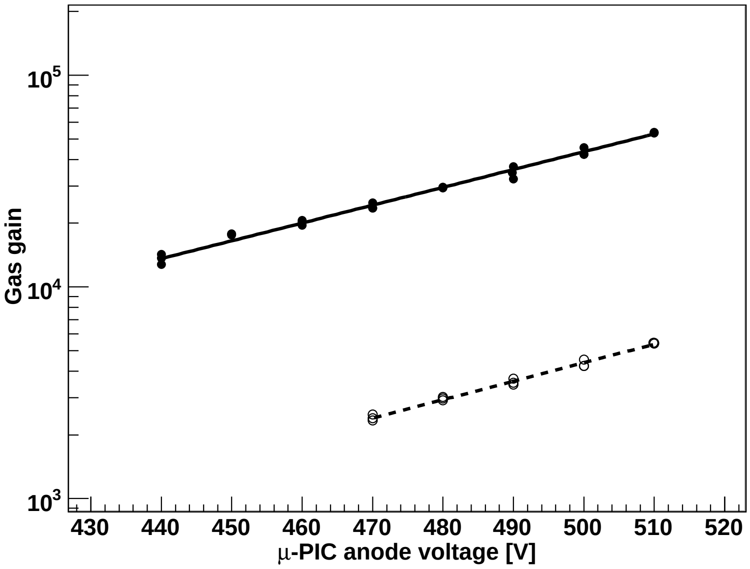

Figure 4.11: The comparison of the gain curve of a μ-PIC with a GEM (filled circles) and that of μ-PIC alone (open circles). (Ar 90 % + C_2H_6 10 % at 1 atm, $\Delta V_{\mathrm{GEM}} = 300$ V, 330 V/cm at Drift region).

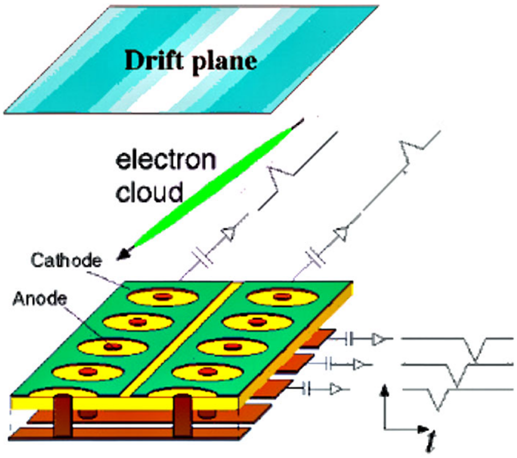

Figure 4.12: Schematic view of μ-TPC.

where, E, P, τ are the electric field intensity, the gas pressure, and the mean free time, respectively. Figure 4.13 shows the electron drift velocity as a function of the electric field. Since τ also depends on E/P, v depends on E/P. This figure says that the behavior of v strongly depends on the type of the gas even at the same E/P.

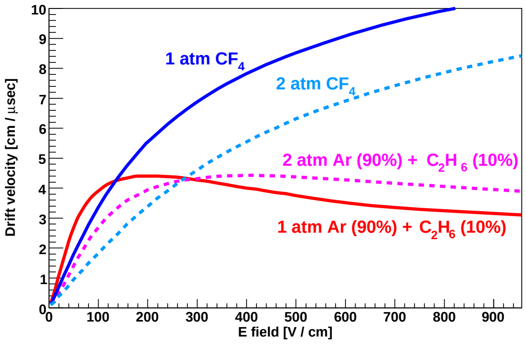

Figure 4.13: The electron drift velocity as a function of the electric field calculated by magboltz-7.1.

Drifting electrons, which at first localize in the ionization point at time $t = 0$, gradually diffuse by the collisions with a gas molecule. At the time t and position x, the transverse diffusion of electrons in the width of dx is described by

$$dN = \frac{N}{\sqrt{4\pi Dt}} \exp\left(-\frac{x^2}{4Dt}\right) dx, \tag{4.2}$$

where N is the number of electrons, D is a diffusion constant. The diffusion constant depends on the gas condition, and also it depends on the electric field in the case of an electron. Figure 4.14 (a) and (b) show the standard deviation of the longitudinal diffusion and transverse diffusion, respectively. Since the diffusion of electrons limits the position resolution for the TPC, a gas having a small diffusion, like CF$_4$, is better as a TPC gas.

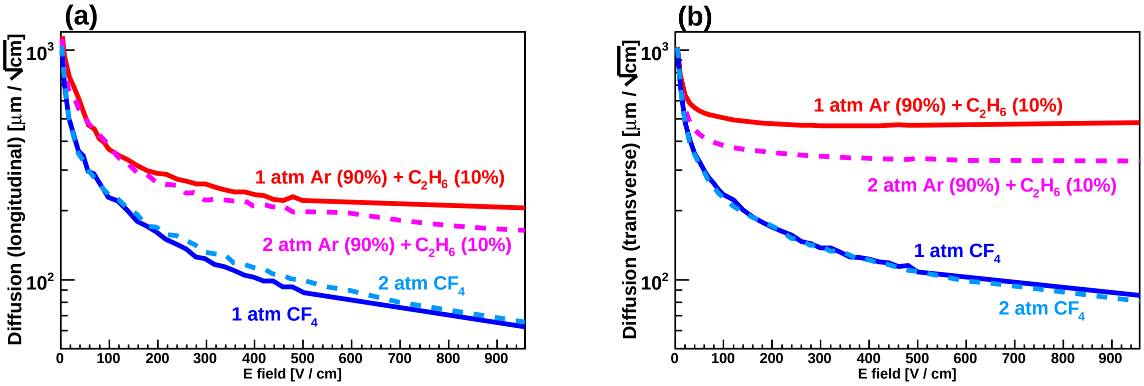

Figure 4.14: The standard deviations of longitudinal diffusion (a) and transverse diffusion (b) calculated by magboltz-7.1.

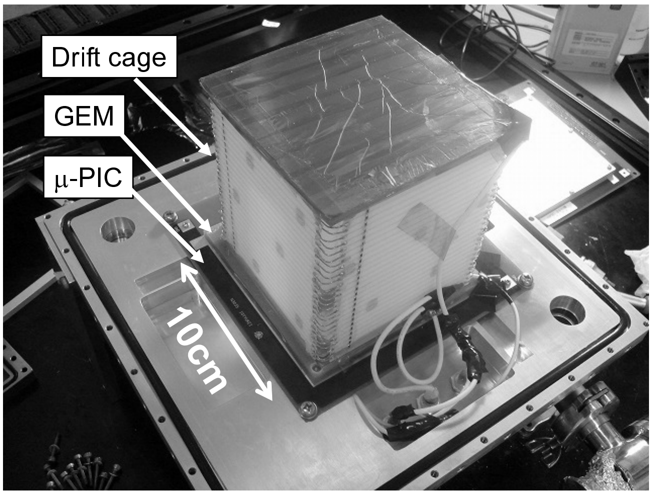

Figure 4.15: Photograph of the TPC without gas vessel.

Figure 4.15 shows the internal parts in the TPC consisting of a GEM and a μ-PIC. The TPC system has an enough gas volume to detect comparatively high energy X-rays, and X-ray spectra were measured with a wider energy range than only a μ-PIC detector.

The spectrum of TPC irradiated with X-rays from a ^{109}Cd source is shown in Fig. 4.16 (a). In this figure, (A), (B) denote ClKα and CuKα fluorescence lines, respectively. Chlorine is included in insulation tape which is used for prevention of discharge in the TPC, while copper is used in the GEM and μ-PIC. CdKα line is shown in (C).

Figure 4.16 (b) shows the FWHM energy resolution as a function of the energy, and the best-fit line for the data points are represented the following equation:

$$\frac{\Delta E}{E} = (29.5 \pm 0.8) \times \left(\frac{E}{22\mathrm{keV}}\right)^{-0.508 \pm 0.008} . \tag{4.3}$$

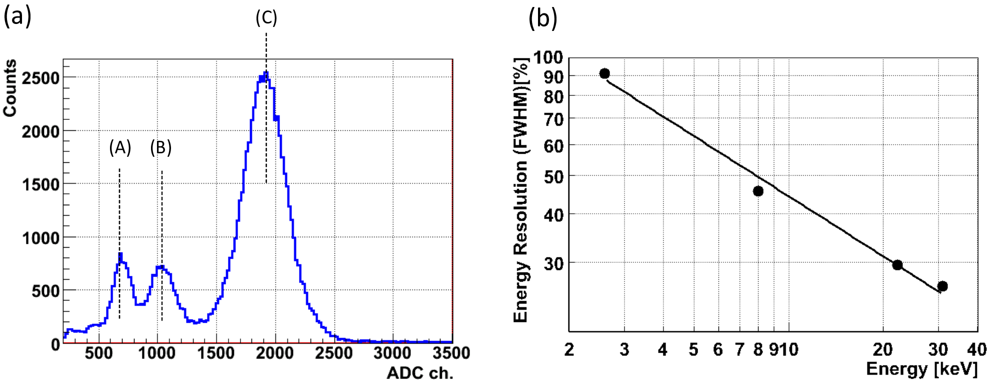

Figure 4.16: Energy spectrum of the TPC irradiated with X-rays from a ^{109}Cd source (a), and the FWHM energy resolution as a function of the energy (b). (A), (B), and (C) in (a) indicate 2.6, 8.0, and 22 keV peak.

4.4 Scintillation Camera

Scintillation camera for the absorber of the ETCC is required to measure the energy and hit position of the scattered gamma rays. Thus we selected the pixel array camera in which every pixel is read with a position-sensitive PMT. The reason of the use and the introduction of other types of position-sensitive camera are described in Chapter 6.

Table 4.1 lists the properties of various scintillators. As the scintillator for an absorber, the required properties are a good energy resolution and a high stopping power. For the use of the pixel structure, the scintillator can be easily handled. Also, for the balloon loading, and a satellite in the future experiment, the scintillator is required to have radiation hardness. For these purposes, we selected GSO:Ce scintillator. Table 4.1 indicates that GSO:Ce scintillator has several good features such as a high effective atomic number, a high density, a high stopping power, reasonable energy resolution, fast decay time, strong radiation hardness and no hydroscopic. Therefore GSO:Ce is suitable for the array camera as an absorber of our ETCC.

For matching the PMT pixel size with the scintillator pixel size, we selected a 5.9 ×5.9 mm GSO:Ce pixel. Usually, we use a 13 mm long pixel due to the radiation length of GSO:Ce, while a 26 mm long one were adopted in the proton beam test in order to measure higher energy gamma rays (1 MeV). A GSO:Ce array consists of 8 × 8 pixels, and a reflector is inserted between each pixel (Fig. 4.17).

The GSO:Ce array was then coupled to a 64-channel multi-anode PMT H8500 with optical grease (OKEN6262A) (Fig. 4.17). The H8500 had an effective area of 49 mm ×49 mm, an external size of 52 mm×52 mm, with a 1.5-mm thick borosilicate glass window. The photocathode in the PMT was bialkali, and the quantum efficiency is over 20 % at 300 - 450 nm (24 % at 420

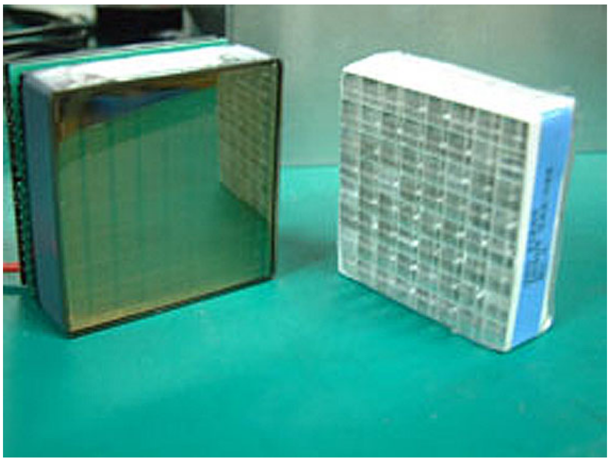

Figure 4.17: Hamamatsu multi-anode PMT H8500 (left) and GSO:Ce pixel array (right)

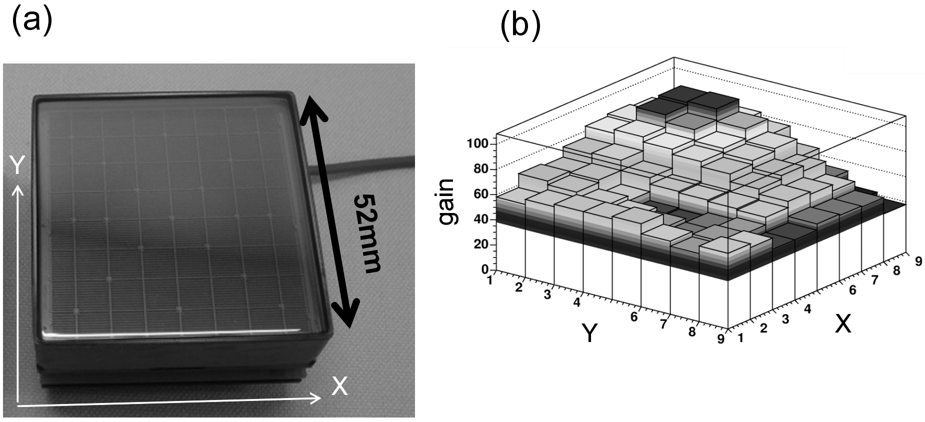

Figure 4.18: (a) Top view of H8500, (b) map of the anode gain for each pixel.

nm). The typical gas gain is $\sim 1.5 \times 10^6$ with a supply voltage of $-1,000$ V at 25 °C, and the gain uniformity of H8500 among 64 anodes is approximately 3 (Fig. 4.18).

Table 4.1: The properties of various scintillators [100]

scintillator	Density [g/cm^3]	Abs. coefficient 511keV [1/cm]	Decay time [ns]	wave length [nm]	light yield (relative)	hydroscopic	radiation hardness [Gray]	refraction index
NaI(Tl)	3.67	0.34	230	415	1	strong	10	1.85
CsI(Tl)	4.53	0.44	1050	550	0.85	weak	10	1.8
CsI(Na)	4.53	0.44	630	420	0.90	strong		1.8
BGO	7.13	0.92	300	480	0.07-0.12	no	10^{2-3}	2.15
LSO:Ce	7.4	0.87	40	420	0.4-0.75	no	10^5	1.82
YSO:Ce	4.45	0.38	40	420	0.3-0.45	no	10^4	1.79
YAP:Ce	5.35	0.46	28	370	0.4	no	10^{2-3}	1.94
YAG:Yb	4.57		3	330/500	0.02	no		1.82
GSO:Ce	6.71	0.70	30-60	440	0.18	no	$> 10^6$	1.85
LGSO	7.2		43	420	0.4	no		
$LaBr_3$:Ce	5.3	0.45	28	385	1.30	strong		1.9
$LaCl_3$:Ce	3.79	0.34	26	385	0.7-0.9	strong		1.9
CWO	7.9	0.92	5000	475	0.3-0.4	no	10	2.3
PWO	8.28	1.15	$< 3 < 20$	430	0.04	no	10^{5-6}	2.2
BaF_2	4.89	0.48	0.6/620	220/310	5/16	no	10^{4-5}	2.2

The 64-anode signals of the PMT were reduced to four channels with a resistor-chain board connecting the 64 anodes with 100 Ω chips as shown in Fig. 4.19 [101]. The output signal from each of the four corners was preamplified with an integrating time of 5.4 μs, and the signals were shaped in a shaping time of 0.5 μs (Hoshin Electronics Co., LTD. N016-V). Then they were digitized with a peak-hold analog-to-digital converter (ADC) (Hoshin V014). Four signals (a, b, c, and d) were used to calculate the two-dimensional positions (x, y) and the light yield corresponding to the energy of an incident gamma ray (E) using the following equations:

$$x = \frac{(c+d)-(a+b)}{a+b+c+d} \tag{4.4}$$

$$y = \frac{(a+c)-(b+d)}{a+b+c+d} \tag{4.5}$$

$$E = a+b+c+d \tag{4.6}$$

Here, the relation between (a, b, c, d), and (x, y) is defined in Fig. 4.19.

For the balloon experiment a compact high voltage power system for PMTs is inevitable. We selected EMCO Q12N-5 as a direct current - high voltage (DC-HV) converter (Figure 4.20), and its specification is listed up in Table 4.2. We control this DC-HV converter by supplying DC level from DAC, which is operated by a VME CPU. We connect this converter to PMT one-by-one, and control the HV of each PMT individually.

In order to extend a detection area, we construct a scintillation wall consisting of GSO:Ce arrays. For example, 3×3 arrays were installed in the ETCC for proton beam test (see Chapter 5). The details of the performance of the GSO:Ce array camera such as reconstructed image and the energy resolution are described in chapter 6.

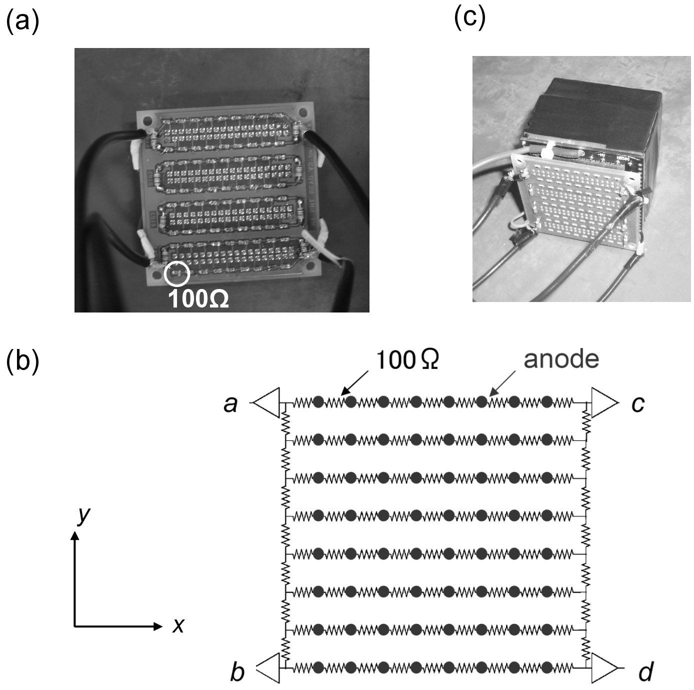

Figure 4.19: Photograph and schematic view of the resistor-chain board as shown in (a) and (b), respectively. (c) shows the chain board coupled to H8500.

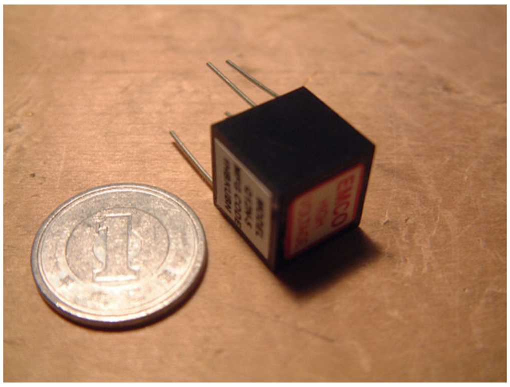

Figure 4.20: DC to HV convertor (EMCO Q12N-5)

Table 4.2: The properties of EMCO Q12N-5

parameter	value
Input Voltage	0.7 - 5 V
Input Current	$<$ 50 mA (No load)
	$<$ 175 mA (Full load)
Output Voltage	0 - -1.2 kV
Output Current	$<$ 0.4 mA
Conversion Factor	$\sim$ 60 %
Ripple Noise	$<$ 0.25 %
Weight	4 g
Size	$1.27 \times 1.27 \times 1.27$ cm^3
Operating Temp.	-25 - $+70$ °C

Chapter 5

Performance of a Real-Time Monitor of Continuum Spectral Gamma Rays in Proton Therapy

5.1 Verification of Dose in Proton therapy

Radiation therapy using protons can damage a tumor efficiently due to its Bragg peak, while normal cells are safe. In order to ensure this advantage and to prevent unwanted exposure, the verification of the energy deposit only on the tumor is strongly important. At the moment, there is no established method to observe the proton dose in the body directly.

In the current treatment planning, the calculation of the proton dose is based on the X-ray CT data or PET imaging. However these calculations still include the uncertainty of 1 - 2 cm, while a 1-cm-size tumor is treated.

For the safer treatment, several groups studied the application of PET imaging to the verification whether the tumor position is irradiated with the proton beam correctly. However the distribution of positron emitters did not match the Bragg peak position as shown in Fig. 5.1, because the positron emitters (e.g. ^{11}C, ^{15}O, ^{45}Ca) have different cross sections as described in chapter 2. In addition, each tissue consists of different ratio of the elements. For example, bone has more calcium(Ca) than other tissues, and much more positron emitters of ^{45}Ca tend to be created. In spite of the mismatch between the annihilation distribution and the Bragg curve, several groups have shown the rough feasibility of the PET for monitoring of proton therapy using a phantom [21, 20, 103, 104, 105]. Figure 5.2 shows the PET imaging for a polymethyl methacrylate (PMMA) target irradiated with 172.63-MeV proton beam, which was calibrated using a time-activity curve for relative isotope abundances from the measurement after the end of the irradiation. Although the results showed a good agreement between measurement and prediction, the acquisition with the PET was in general prolonged over 10 to 20 min after stopping the irradiation in order to collect sufficient statistics up to 10^6 to 10^7 true coincidences [104].

Moreover, generated annihilation gamma rays is fewer than other gamma rays which generated by nuclear reaction during proton irradiation. This was why it could not be realistically

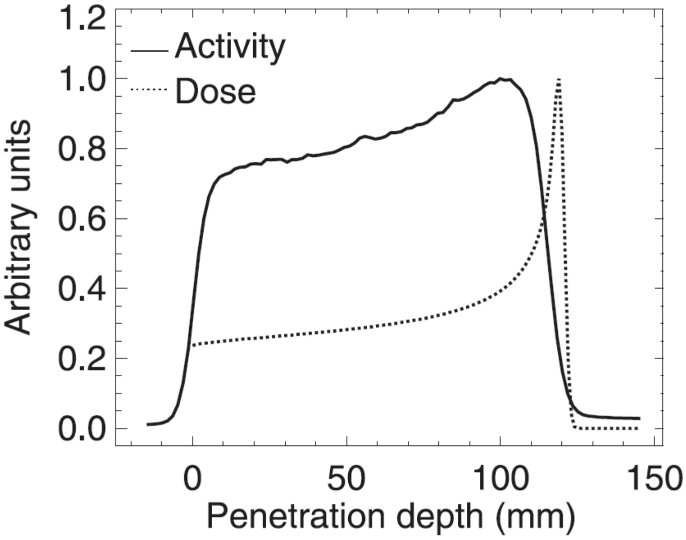

Figure 5.1: Measured β^+-activity depth profiles (solid line) for proton irradiation of PMMA targets at 140 MeV initial energy. The dotted line shows the calculated relative dose distributions [104].

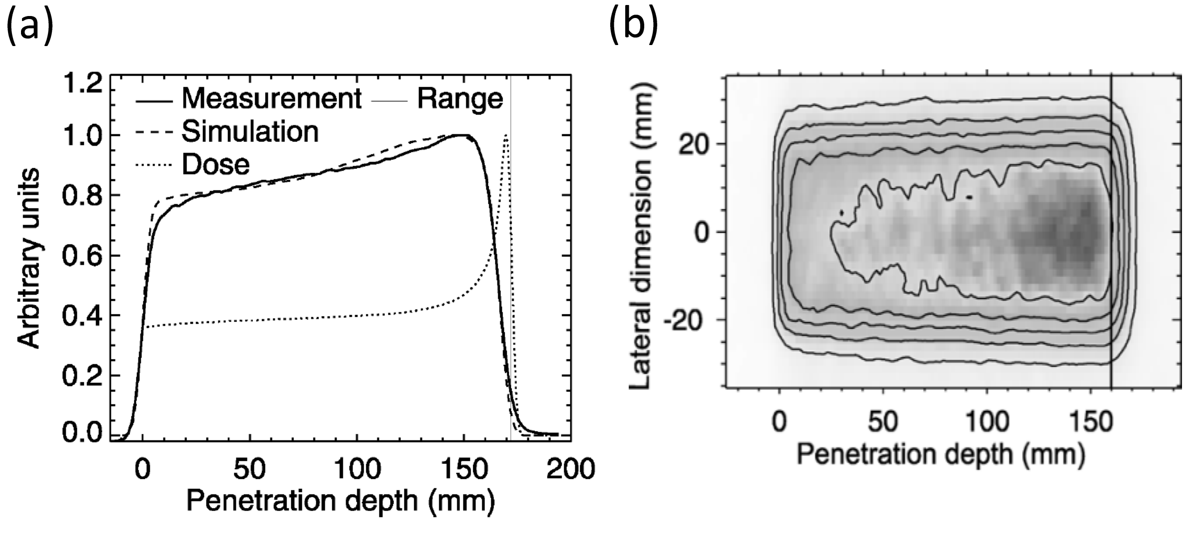

Figure 5.2: (a)Measured (solid) and predicted (dashed) β^+-activity depth profiles irradiated with (maximum) energy of 171.62-MeV proton. The dotted line depicts the expected dose, calculated by means of FLUKA. The thin solid line shows the expected range from [106], corrected for the material in the beam path as the simulated data. (b) PET image reconstructed from the data exclusively measured during the about 300 sec delivery of the proton [104].

applied in clinical use [107].

Prompt-gamma ray imaging reported as a good candidate to be a dose monitor for proton therapy [22, 109], because the distribution of the prompt gamma rays correlates closely with the proton dose distribution, in the end of the range (fall-off) especially. Moreover use of the prompt gamma rays is expected to provide us the accurate information of the proton dose, because the gamma-ray emission yields are the same order of magnitude as the number of fragmentation events [110].

Several groups measured a prompt gamma-ray distribution for the proton therapy using not a imaging detector but only a photon counting detector with a collimator [22, 109]. For example, Fig. 5.3 shows a prompt gamma scanner (PGS) which had three layers of shielding against neutrons and gamma rays generated from a water phantom regarded as human body. The paraffin layer moderated the high energy neutrons, and the B_4C powder captured the neutrons by the $B(n,\gamma)$ reaction. Finally the lead layer prevented from the unwanted gammas. The gamma detector was a CsI(Tl) scintillator. The PGS measured gamma ray distributions in the water phantom irradiated with three different energy protons (100, 150, and 200 MeV), and a parallel-plate ionization chamber (IC) also measured the beam intensity in the water in order to find out the correlation between the actual dose distribution and the response of the PGS as shown in Fig. 5.4 (a). Here the PGS data was selected with a gamma-ray energy of over 4 MeV, and it was noticed that the gamma ray distribution with an energy of over 4 MeV was more sharp as shown Fig. 5.4 (b). Fig. 5.4 (a) shows that the peaks of prompt gamma distributions were well correlated with the Bragg peaks of the dose distributions within 1 - 2 mm at 100 MeV [22].

However, the scan by the PGS took much time to measure the dose distribution, and it was not a practical detector for the medical imaging. Thus, a detector with a wider energy dynamic range up to a few MeV is required for the measurement of continuum gamma rays above 1 MeV. Therefore we need the imaging detector which can measure the continuum gamma rays.

Here, the PET does not have the ability to obtain the continuum gamma rays. Although the SPECT is studied as prompt gamma-ray monitor using simulations [111], no one demonstrate the monitor. In fact, the SPECT is also difficult to image the continuum gamma rays, and usually their energy range is only below $\sim$ 300 keV. In order to detect the prompt gamma rays, we must measure the gamma rays during the beam therapy, and there are a lot of backgrounds out of the target owing to the nuclear interaction or scattering. Thus, classical Compton cameras are also hard to image due to the low gamma-ray background rejection. Although Richard et al. proposed a double scattering Compton camera as a simulation study [107], any detectors have not yet developed.

Our ETCC is expected to satisfy the above requirement, because the ETCC has imaging ability with a wide energy dynamic range in the sub-MeV and MeV region and the rejection ability of background gamma rays. In addition, the ETCC is expected to identify the particle from the measurement of the energy deposit (dE/dx) of the charged particle and three-dimensional

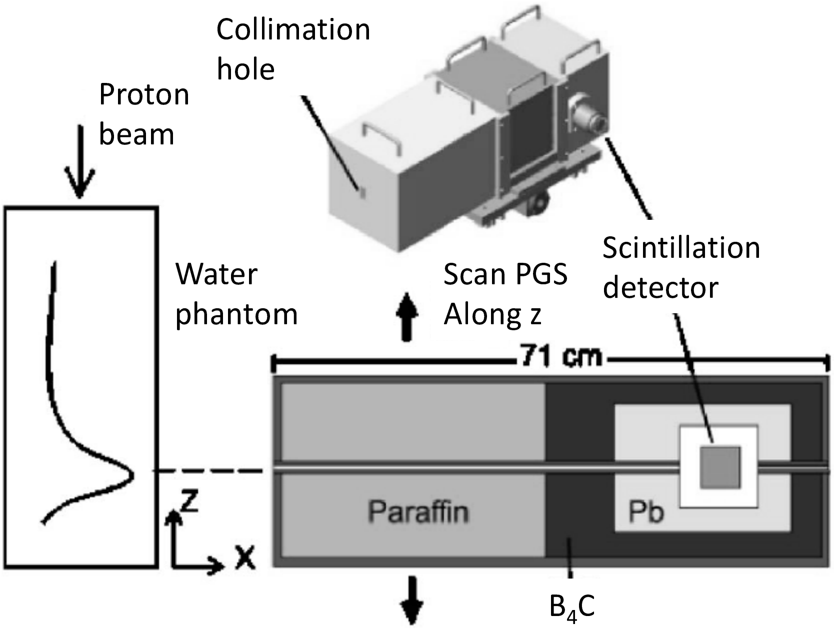

Figure 5.3: Schematic view of PGS [22].

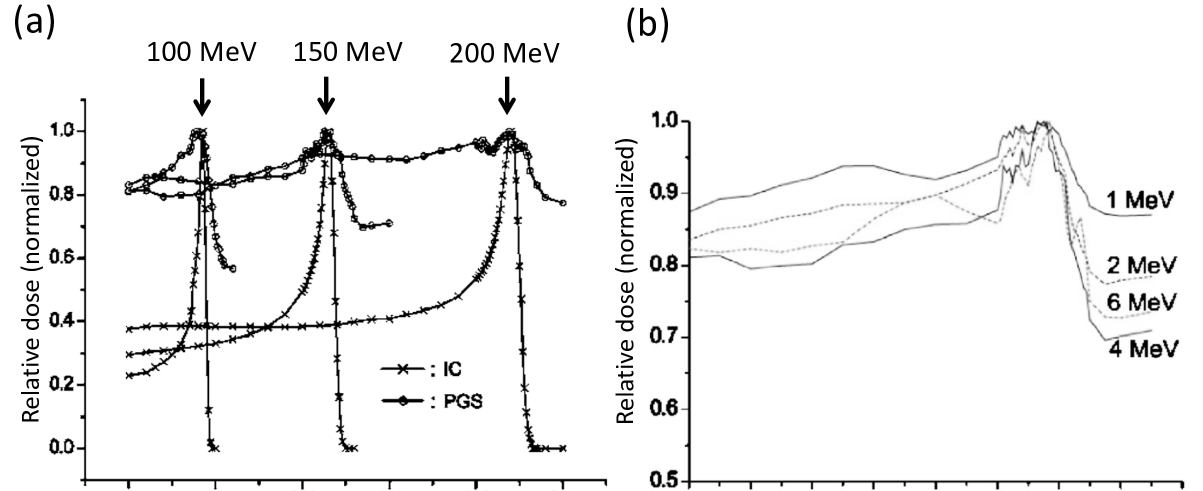

Figure 5.4: The results of the PGS. (a) Comparisons of the depth-dose distributions measured by the ionization chamber with the PGS measurements at three different proton energies of 100, 150, and 200 MeV. (b) Distributions of gamma-ray counts as a function of depth with different minimum gamma energies as indicated [22].

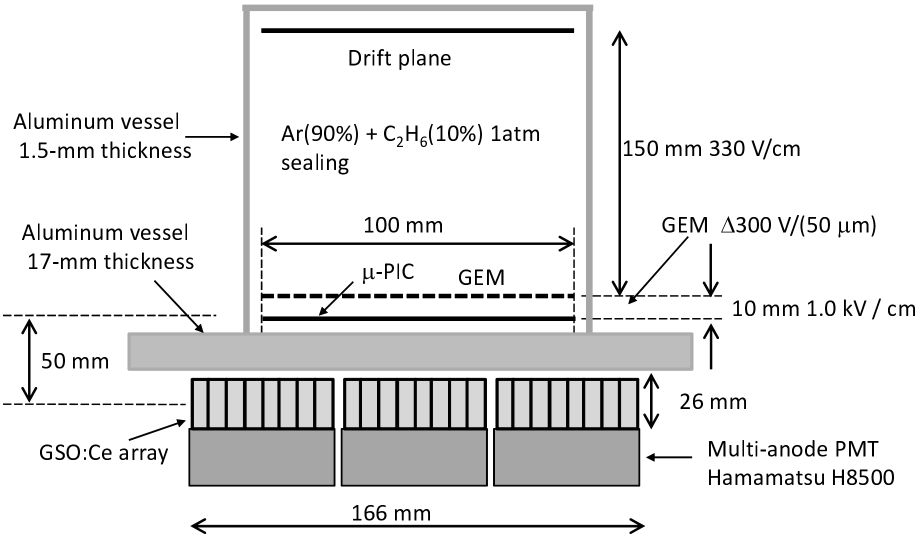

Figure 5.5: Schematic view of the ETCC for the proton therapy monitor.

tracking in the gaseous TPC, which enables to reject the background under the proton irradiation. Therefore, the ETCC is expected to be used for the real-time monitoring system in proton therapy [108], and then we tested the performance of the ETCC for the proton therapy using a water phantom irradiated with proton beam, and we compare the gamma rays distribution between the measurement and simulation.

5.2 Setup of the Beam Experiment Using the Compton Camera

In order to demonstrate feasibility for proton dose monitor, we measured the continuous gamma rays from a water phantom irradiated with proton beam. Several groups reported the necessity of a detector of higher energy gamma rays over $\sim$ 1 MeV described in chapter 2 and the previous section. However, our ETTC had not been studied for a higher energy gamma-ray imaging above 1.2 MeV from an ^{59}Fe source. Therefore, we first tested the high energy gamma ray imaging using a gamma-ray point sources up to 1.8 MeV (^{88}Y) in the experiment room at Kyoto University.

5.2.1 Performance of the ETCC

We have prepared an ETCC consisting of 3 × 3 GSO:Ce arrays, and a gaseous TPC as shown in Fig. 5.5. The TPC had a detection area of 10 cm×10 cm and a height of 15 cm, and the gas volume was enclosed in a sealed aluminum vessel and filled with an argon-ethane gas mixture (9:1) at 1 atm. A drift voltage of -5500 V was supplied to the drift plane. The 50-μm-thick GEM had an effective area of 10 cm ×10 cm. The voltages of the top and bottom planes of the GEM were set at -830 V and -530 V, respectively, for a gas gain of approximately 10. The

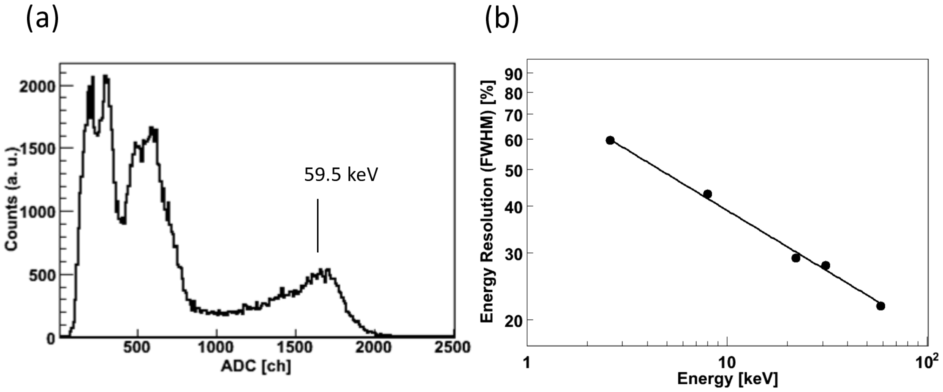

Figure 5.6: (a) TPC energy spectrum irradiated with X-rays from an ^{241}Am source. (b) Energy resolution as a function of the energy.

separation between the GEM and μ-PIC was 0.5 cm.

The μ-PIC, with an effective area of 10 cm ×10 cm, was operated at 470 V with a gain of approximately 3500. The total gas gain of the TPC was $\sim 3.5 \times 10^4$. Figure 5.6 (a) shows the energy spectrum irradiated with X-rays from an ^{241}Am source using a charge ADC, where a 59.5 keV line is measured. We also irradiated the TPC with ^{109}Cd (22 keV), ^{133}Ba (31 keV), and then the energy resolution was shown in Fig. 5.6 (b). The best-fit line for the data points were represented as the following equation:

$$\frac{\Delta E}{E} = (30.0 \pm 0.9) \times \left(\frac{E}{22\mathrm{keV}}\right)^{-0.32\pm0.01} . \tag{5.1}$$

To obtain the high energy gamma rays efficiently, we used 26-mm-thick GSO:Ce arrays, while other structure of the GSO:Ce array camera was the same as a 13-mm thick prototype array of which detail are described in Chapter 6. 3×3 GSO:Ce arrays were set at 5 cm front of the μ-PIC and the center of pixel. The average and standard deviation of energy resolution was $12.6 \pm 1.4\%$ at 662 keV (FWHM) for the all pixels, and the dependence of the energy resolution as a function of the energy is shown in Fig. 5.7. The energy resolution was worse than the 13-mm-thick ones with a typical energy resolution of $\sim 11\%$ at 662 keV (FWHM), because the gain of the preamplifier was set lower than the typical use by a factor of approximately 0.5 in order to obtain a wider energy range up to 2 MeV at least. In addition, aspect ratio of the pixel scintillator, which defined as the ratio of the pixel-height h to the reading area A (h/A) here, was longer than the 13-mm-thick one, which also degraded the energy resolution. The best-fit line in Fig. 5.7 was represented the following equation:

$$\frac{\Delta E}{E} = (12.7 \pm 3.4) \times \left(\frac{E}{662\mathrm{keV}}\right)^{-0.28\pm0.2} . \tag{5.2}$$

Using this ETCC, gamma-ray images were obtained by following analysis.

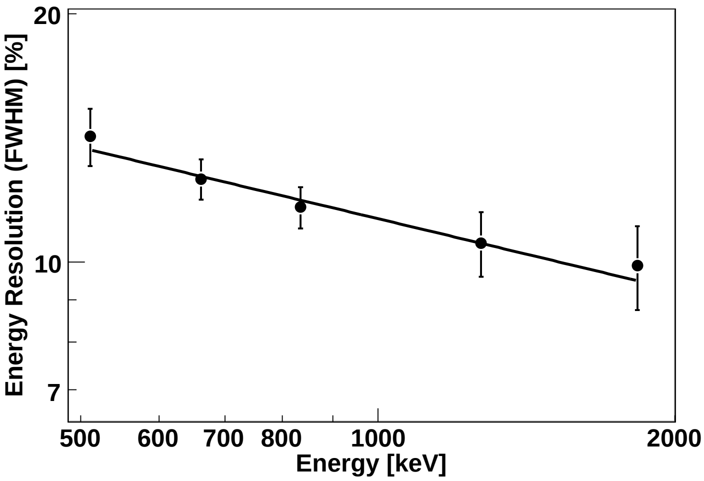

Figure 5.7: Average-energy resolution (FWHM) of the 26-mm thick GSO:Ce arrays as a function of the energy. The error bars denote the standard division of the energy resolutions among GSO:Ce 64 pixels.

Trigger number To obtain a real Compton scattering event, one electron track in the TPC and one hit in the GSO:Ce unit individually are required. When the two or more GSO:Ce array hits in the one Compton event, this event would be the background such as a charged particle event, a multiple scattering event or a random coincidence. Thus, we used the scintillator information from only one GSO:Ce array units in each Compton event.

Hardware threshold In this beam test, our target energy band was more than $\sim$ 400 keV as described previously,since 511-keV gamma rays are necessary to compare with the PET imaging. Thus, we set a hardware threshold for the scintillator cameras corresponding to $\sim$ 350 keV, while a threshold of TPC analog signal was $\sim$ 1 keV.

N-hit cut To obtain the electron tracking, We required three or more than three hit points of the electron track in the TPC (Nhit ≥ 3).

Fiducial cut The edge of the gas detection region near the drift cage or GEM tend to generate some backgrounds. For example, the Compton scattering in the drift cage is hard to reconstruct. Then we selected an event in which all hit points in the TPC are within a fiducial volume with an area of 7 cm $\times$7 cm and from 2 to 14 cm above the μ-PIC. This cut is also effective to select the escape event of the recoil electron from the TPC.

dE/dx cut For the electron-tracking measurement in the TPC, dE/dx is calculated based on the Bethe-Bloch formula. Figure 5.8 shows the recoil-electron track length as a function of the energy when the ETCC is irradiated with 662-keV gamma rays. (a) and (b) are simulation (GEANT4) results of all hit events, and only Compton events in which the recoil-electron energy is measured with the TPC, respectively. These figures suggest that

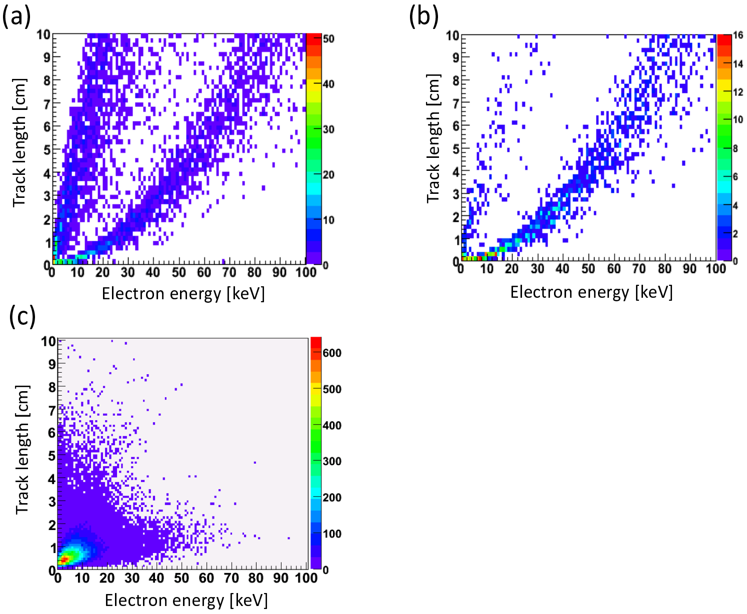

Figure 5.8: Recoil-electron track length as a function of the energy when the ETCC is irradiated with 662-keV gamma rays (simulation data) or gamma rays from a ^{137}Cs source (real data). (a) Simulated hit events in the TPC, (b) Compton events selected from (a), (c) raw data of measured events with the ETCC.

the restriction on the length l and energy E of the electron (dE/dx cut) is efficient for the rejection of gamma-ray backgrounds such as random coincidence and escape events of a recoil-electron escaping from the TPC. (c) shows the dE/dx for the experimental data, where the selection region is drawn by red liens as represented by following inequalities:

$$1.671 \times E^{8.056\times10^{-3}} + 0.5 \geq l \tag{5.3}$$

$$1.779 \times E^{2.100\times10^{-3}} - 1.0 \leq l, \tag{5.4}$$

where these parameters are determined by the simulation study.

Using above selected events, we obtained resultant gamma-ray images. Figures 5.9 (a) and (b) show the reconstructed images for an ^{88}Y point source (1836 keV) located 34 cm from the center of the μ-PIC surface and also at 5-cm off-center, where we reconstructed gamma rays with an energy band between 1712 - 1918 keV. These images show the ETCC had imaging ability for higher energy gamma rays than 1 MeV.

The ETCC had an energy resolution of $15.3 \pm 0.5\%$ at 662 keV (FWHM). ARM and SPD were $(5.1\pm0.2)^\circ$ and $(119\pm2)^\circ$ at 662 keV (FWHM), respectively. Figure 5.10 shows the energy resolution as a function of the gamma-ray energy, and the angular resolutions (ARM and SPD) are shown in Fig. 5.11. This ARM $\Delta\phi$ corresponded to an FWHM spatial resolution Δx of 2.2 cm at 662 keV when the distance between the center of 15-cm-high TPC and the target was 25 cm [1]. In addition, the position accuracy in the center position was determined to be

---

[1] $\Delta x = 25 \times tan(\Delta\phi/2) \times 2$

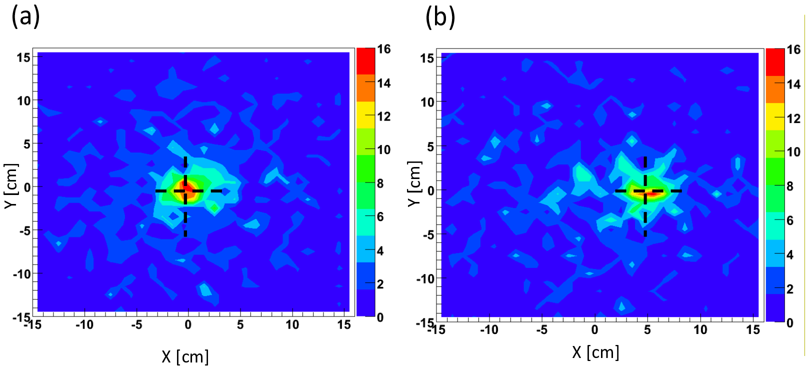

Figure 5.9: Gamma-ray images obtained with the ETCC for an ^{88}Y point source at the center (a) and 5-cm off center. Cross marks denote the target point.

approximately 3 mm (FWHM) at 835 keV by accumulating a few hundreds events from a ^{54}Mn point source.

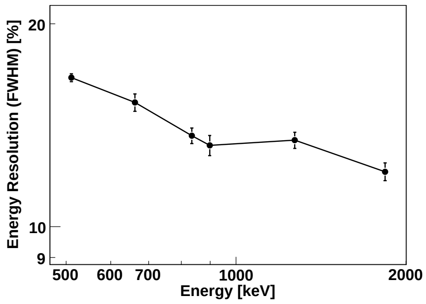

Figure 5.10: FWHM energy resolution of the ETCC as a function of the energy.

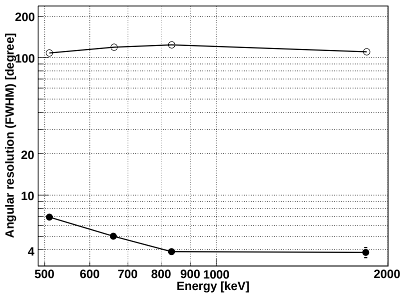

Figure 5.11: FWHM angular resolution of the ETCC as a function of the energy. (filled circle):ARM, (open circle):SPD.

5.2.2 Setup of Beam Test

Figures 5.12 and 5.13 show the setup for the proton beam test using ”ES Course” at Research Center for Nuclear Physics (RCNP) of Osaka University. The beam energy was 140 MeV. The proton beam target was a water phantom with a volume of ϕ20 cm ×30 which made from polymethyl methacrylate (PMMA) with a thickness of 0.5 cm except a ϕ20-cm surface in the opposite side of beam entrance (1-cm thickness). Roughly the water phantom was regarded as human body which consists of approximately 70 % water. From GEANT4 calculation, the water depth in the Bragg peak position was 12 cm, taking into account the obstacles such as the wall of water tank and the flange of the vacuum tube made of PMMA. Then the TPC center was set in front of the Bragg peak.

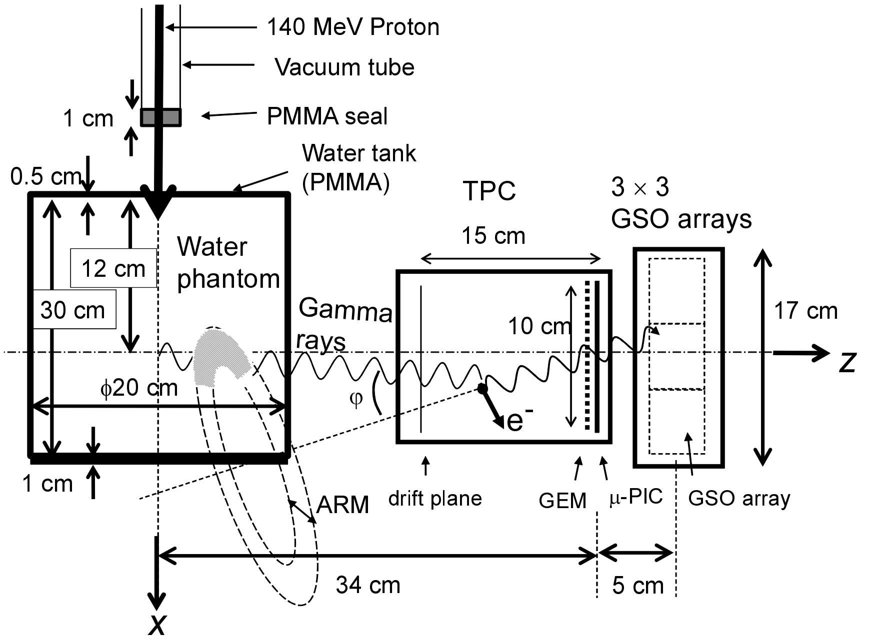

Figure 5.12: Schematic view of the setup for proton beam test at RCNP.

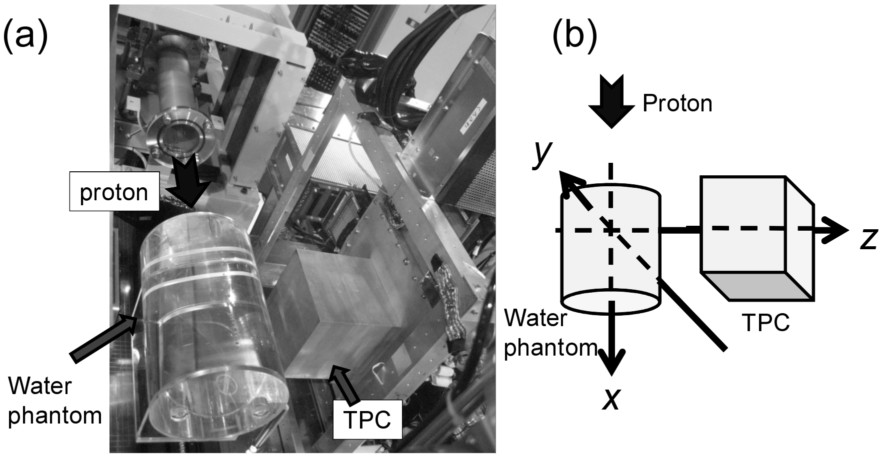

Figure 5.13: (a) Photograph of the setup, (b) definition of the axis.

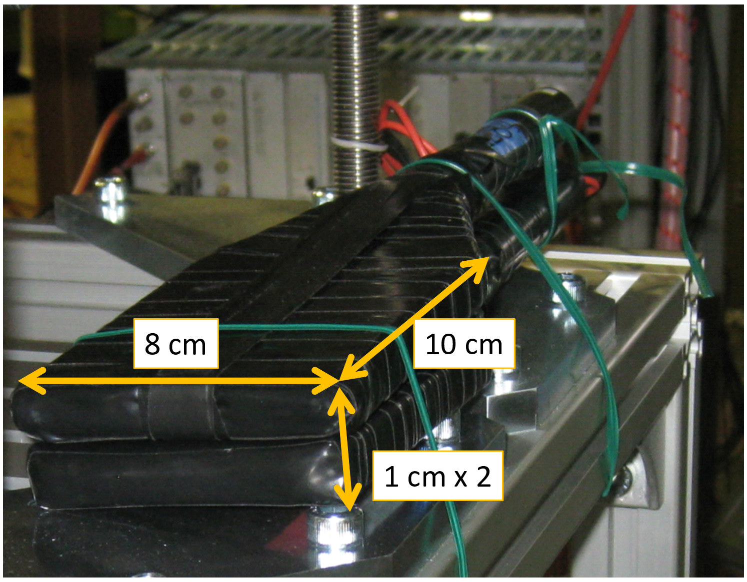

Figure 5.14: Photograph of plastic scintillators for a beam current monitor.

5.2.3 Beam Current Monitor

Since a beam current monitor as a laboratory equipment in the beam line does not work below the sub nA range, we set two monitor sets named #1 and #2. Each set consists of two plastic scintillators (ELJEN EJ-200) with a size of 8 cm ×10 cm ×1 cm read by a single anode PMT (Hamamatsu R1166A, ϕ 19-mm tube) which was operated with a gain of $\sim 10^6$ (Figs. 5.14 and 5.15). In each monitor set, the coincidence event of two plastic scintillators was counted, and they measured the relative proton beam current indirectly.

These monitors were installed at two points as shown in Fig. 5.16. Here #1 usually measured the relative beam current during a Compton camera imaging, while #2 was used for a high count-rate proton beam for which a current monitor equipped in RCNP was available. In order to calibrate the relation between the coincidence count rates of each plastic scintillator monitor and the proton beam intensity, at first #2 was calibrated by the monitor equipped in RCNP. Then using the correlation between #1 and #2, we roughly estimated the absolute current during the Compton imaging roughly.

Before the beam experiment in RCNP, we tested the beam monitor in Kyoto University. Each monitor set was irradiated with gamma rays from a ^{60}Co source (1173, 1333 keV) with several intensities by use of sources with different activities or change of the distance. Figure 5.17 shows the count rate as a function of estimated gamma-ray intensity. Best-fit lines for the data points in the Figs. 5.17 (a) and (b) were represented the following equations:

$$\text{count rate} = (2.591 \times 10^4) \cdot I^{1.228} \qquad (\text{for } \#1) \tag{5.5}$$

$$\text{count rate} = (3.267 \times 10^4) \cdot I^{1.306} \qquad (\text{for } \#2), \tag{5.6}$$

where I is gamma-ray intensity. Although the gamma-ray intensity and count rate were out of

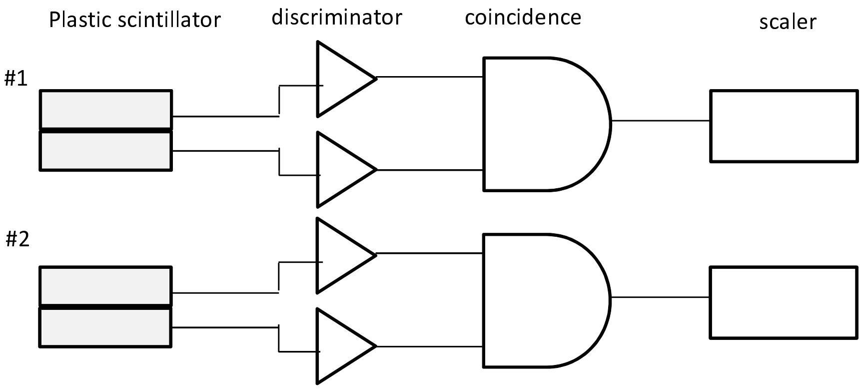

Figure 5.15: Schematic view of set up.

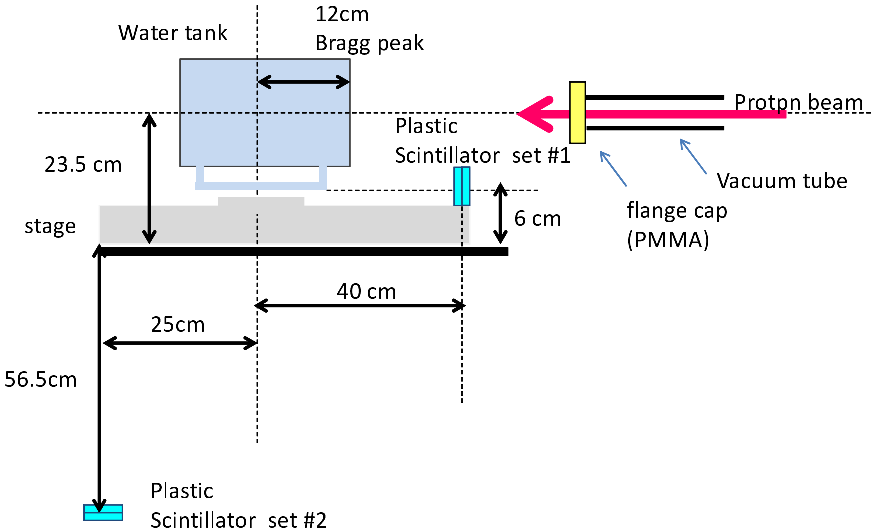

Figure 5.16: Schematic view of set up in the RCNP.

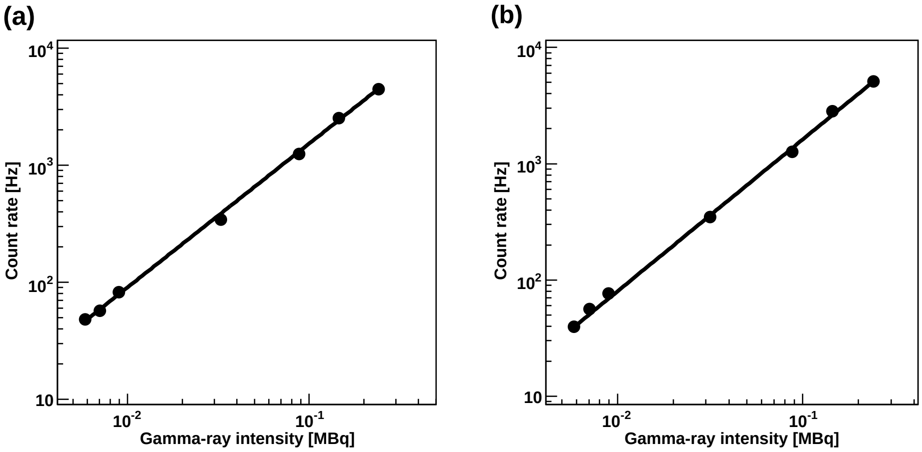

Figure 5.17: Count rate as a function of the gamma-ray intensity for the beam experiment monitor set # 1(a) and 2 (b).

proportion with a linear function, this results result showed a strong correlation between them. Thus these scintillators had the feasibility for the beam monitor.

Table 5.1: Beam time schedule

day	Beam start	Beam Stop	time
April 28	10:02	12:1	2:10
	12:22	13:09	0:46
	13:19	16:32	3:13
	17:42	18:52	1:10
	19:10	19:24	0:13
	20:04	20:16	0:12
	22:30	1:34	3:04
April 29	1:42	7:05	5:22
	7:22	8:48	1:26
	8:54	13:51	4:56
	14:00	14:44	0:44
	14:56	20:01	5:04
	20:09	20:26	0:17
	0:37	1:23	0:45
April 30	1:30	8:59	7:29

5.3 Results of the Beam Test

We irradiated the water tank with a 140-MeV proton beam on April 28 - 30 in 2010 as shown in Table 5.1, where the beam did not continue the whole time due to the maintenance of the beam accelerator or entrance into the beam room by other groups. Figure 5.18 shows the count rate of the plastic scintillators (the proton-beam current monitors) #1 and #2 during the beam-on and off as a function of elapsed time from the beam start at 10:02 on April 2010, and the sampling time was 10 sec per a one measurement. Sometimes data acquisitions were in failure, and spike peaks were seen in the Fig. 5.18. These monitor #1 and #2 had averages and standard deviations of count rates of 107 ± 13 and 2.1 ± 0.5 Hz, respectively.

The current monitor # 2 were calibrated by a laboratory equipment of the current monitor in the RCNP using $\sim$ 1-nA proton beam (Fig. 5.19), and the count-rate correlation between monitor # 1 and 2 are shown in Fig. 5.20. Best-fit lines for the data points in the Figs. 5.19 and 5.20 were represented the following equation:

$$p_2 = (4.535 \times 10^3) \times R^{1.366} \qquad \text{(for Fig.5.19)} \tag{5.7}$$

$$p_2 = (2.732 \times 10^{-2}) \times p_1^{0.8326} \qquad \text{(for Fig.5.20)}, \tag{5.8}$$

where $p1$, and $p2$ Hz denote count rate of # 1, 2, respectively, and R nA is proton beam current measured by the RCNP's current monitor. This results showed that the beam current during the measurement with the ETCC was $\sim$ 2 pA.

For the ETCC, the beam duration time was 32 hours (live time), and dead time due to the data acquisition was 6 %. Figure 5.21 shows the energy spectrum of the ETCC during the beam time. This spectrum had a 511-keV peak. However other peaks such as 2.2-MeV neutron capture peak were not detected, because of large background gamma rays.

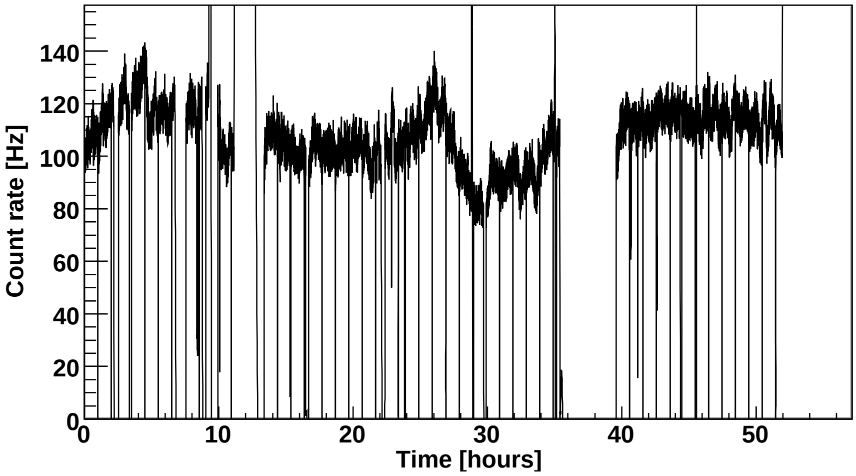

Figure 5.18: Count rates of plastic scintillator monitor #1. start time (time 0) is 10:02 on April 28.

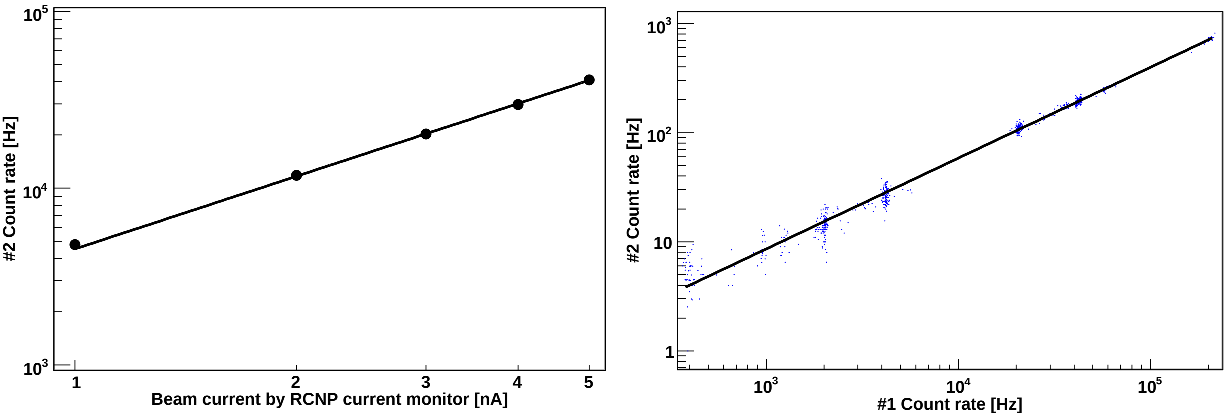

Figure 5.19: Count rates of plastic scintillator #2 as a function of the proton beam current measured by RCNP's current monitor.

Figure 5.20: Count rates of plastic scintillator #2 as a function of the count rates of plastic scintillator #1.

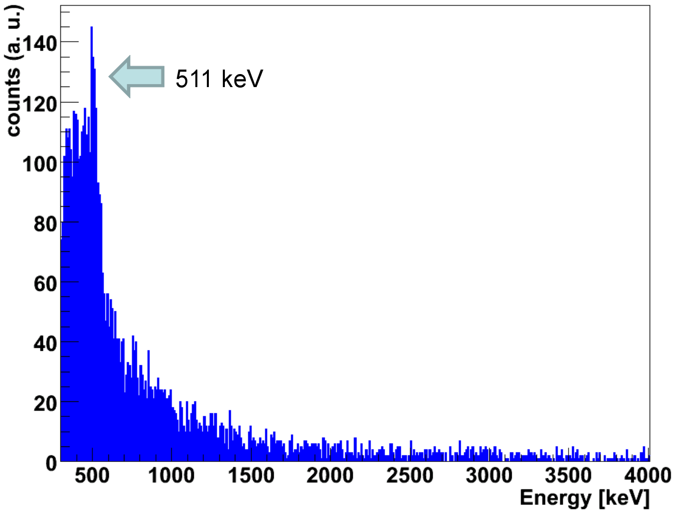

Figure 5.21: Energy spectrum of the ETCC.

Figure 5.22 shows the water phantom imaging with the ETCC. In the region from 463 to 559 keV, which corresponds to the twice width of a FWHM energy resolution of the ETCC at 511 keV, we obtained 890 final events, while in the 0.8 - 2 MeV range, 1288 events were detected. We succeeded in obtaining the individual images for two different energy band (463 - 559 keV and 0.8 - 2 MeV).

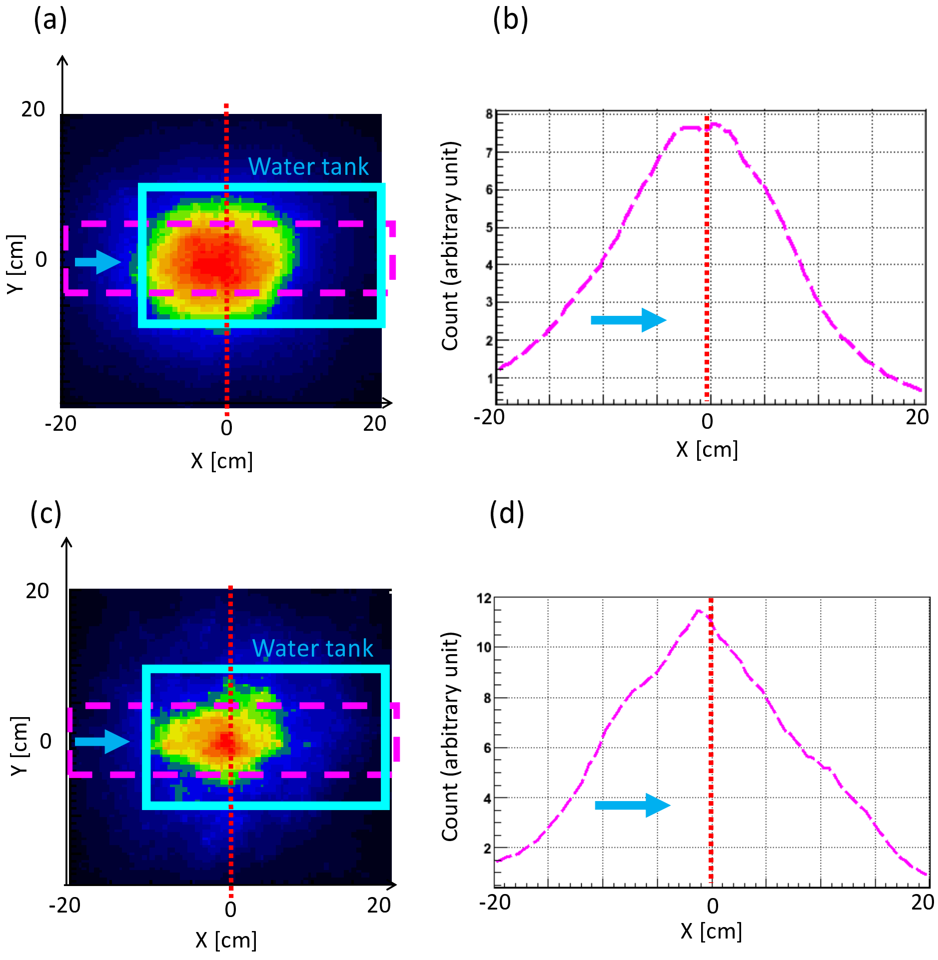

Figure 5.22: Imaging results of the proton beam test. Left side images are reconstructed images with an energy band of 463 - 559 keV (a) and 0.8 - 2 MeV (b), respectively. (b) and (d) are image profiles on the beam axis, indicated by the dashed square in (a) and (c), respectively. Dotted lines and arrows denote the Bragg peak and the direction of the proton beam, respectively. X and Y axes are defined in Fig. 5.13 (b).

5.4 Analysis of Imaging

5.4.1 Gamma-ray Distribution in the Water Phantom

For the discussion of the imaging results, we used the GEANT 4 simulation (version 9.3.patch-01). Here our simulation code was based on the hadron therapy as an example consisting of the hadron physics package, "G4HadronElastic" and "Binary Cascade model". In addition, we used Livemore Library as a low energy model, because low energy Compton scattering ($\sim$ 100 - 300 keV) also occurs in the ETCC. The set up for the simulation was drawn in Fig. 5.12 which is schematic view of a real set up.

Since a full-simulation was estimated to take so long time of more than a year using our four PCs (CPU $\sim$ 3 GHz $\times$ 4), not super computers, we only simulated the interaction between the incident proton beam and some atoms in the air, the water phantom, and the ETCC. Here, the full-simulation includes also the reconstruction of the image with the ETCC using its imaging method and performances such as energy resolutions and some noises in the electronics.

When the water phantom was irradiated with 140-MeV proton beam, the gamma rays were generated as shown in Fig. 5.23, which was distributions of generated gamma rays in the all energy, 6 - 10, 0.8 - 2, and 0.50 - 0.52 MeV. Slice images of the Figs. 5.24 are shown in Fig. 5.23. Although higher energy gamma rays formed a sharper peak near the Bragg peak, the distribution of 0.8 - 2-MeV gamma rays, especially the fall-off, also correlated to the Bragg peak. However, the distribution of around 511-keV gamma rays was found to be a more diffuse image.

5.4.2 Method of Gamma-ray Imaging with the ETCC

In order to obtain the realistic results for the ETCC measurement, we processed the position data of incident simulated gamma rays in the TPC using some statistical weights or detector performance as followings:

1. energy resolution of the ETCC
2. detector responses function
3. point-spread function
4. detection efficiency as a function of energy

The response function represented the sensitivity as a function of the detection position in the ETCC. The center of a field-of-view was higher sensitivity than the edge, and the count rate depends on the source position. To make a response function, I used the real point source images measured by the ETCC. Figures 5.25 and 5.26 showed the ETCC response functions along x and y axes, respectively. Those functions represented the dependence of count rate on the position, and they were made by a ^{54}Mn point source imaging in the several points on the

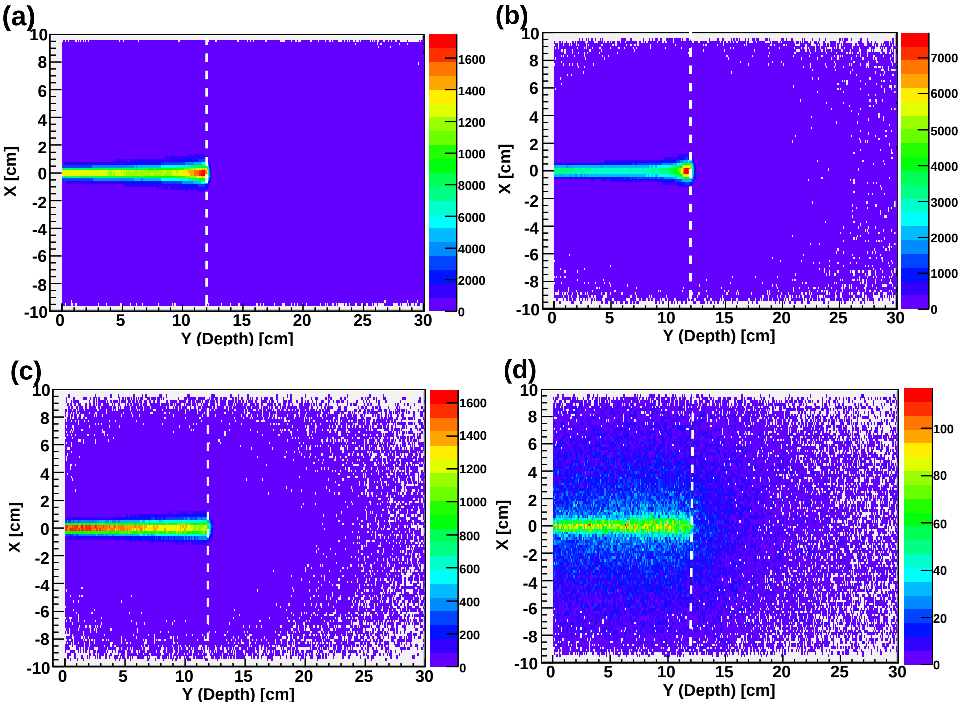

Figure 5.23: Distributions of generated gamma rays with an energy of all energy (a), 6-10 (b), 0.8 -2 (c), and 0.50 - 0.52 MeV (d). Dotted lines indicate the Bragg peak position.

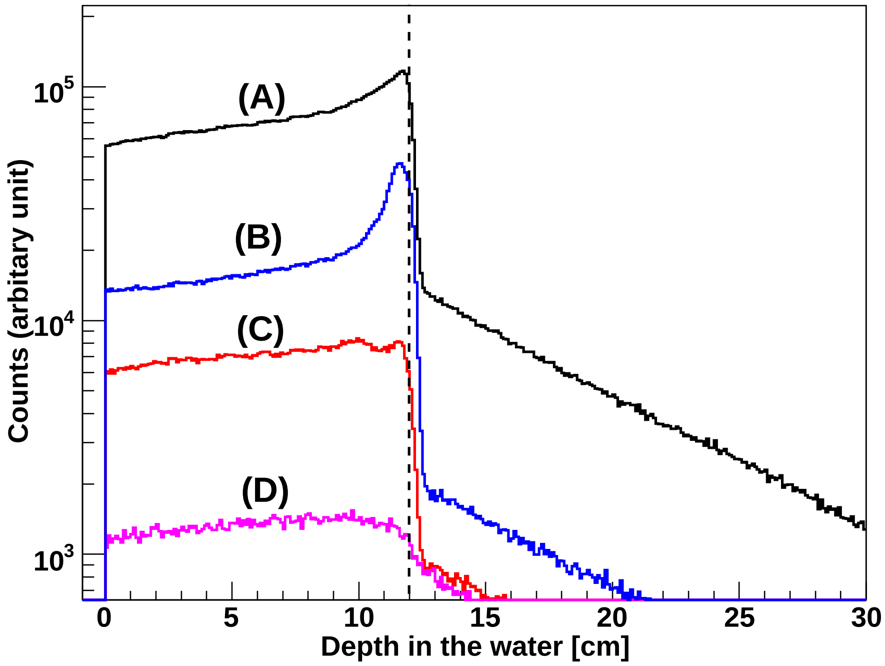

Figure 5.24: Slice image in the Fig. 5.23 from $x = -9$ to 9. (A) to (D) denote the data of (a) to (c) in the Fig. 5.23, respectively. Dotted line indicates the Bragg peak position.

Table 5.2: Fitting parameters in equation 5.9

	a	b	c	d	e	f	g
x-axis	0.002096	-0.4345	5.952	0.00136	-0.05418	19.92	3.96×10^{-5}
y-axis	0.001791	1.198	6.86	0.00087	1.496	15.67	3.989×10^{-5}

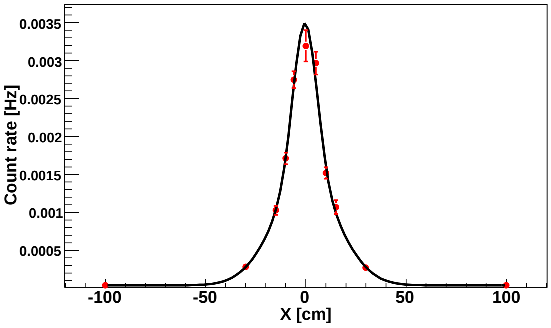

Figure 5.25: Response function for x-axis.

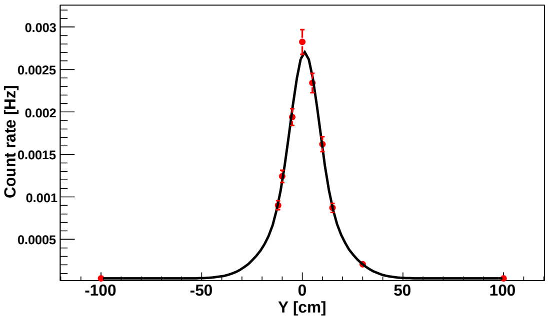

Figure 5.26: Response function for y-axis.

x and y axes. Phenomenological best-fit lines for the data points in Figs. 5.25 and 5.25 were represented by the following equation which is double-Gaussian function:

$$\text{count rate} = a \exp\left(-0.5\left(\frac{x-b}{c}\right)^2\right) + d \exp\left(-0.5\left(\frac{x-e}{f}\right)^2\right) + g, \tag{5.9}$$

where a - g are fitting parameters, and each value was listed in Table 5.2.

Using the two best-fit function f_x and f_y, we assumed that the two-dimensional response function f_2 is represented as following equation and shown in Fig. 5.27 Then simulated point was multiplied by the two-dimensional response function.

$$f_2 = \frac{(f_x(r) + f_y(r))}{2} + 0.5\,(f_x(r) - f_y(r)) \cdot \left(\frac{|x| - |y|}{|x| + |y|}\right), \tag{5.10}$$

where $r = \sqrt{(}x^2 + y^2)$.

Point-spread function (PSF) represents the performance of the imaging. Using this function as a probability density function, a simulated point position was spread into the real image.

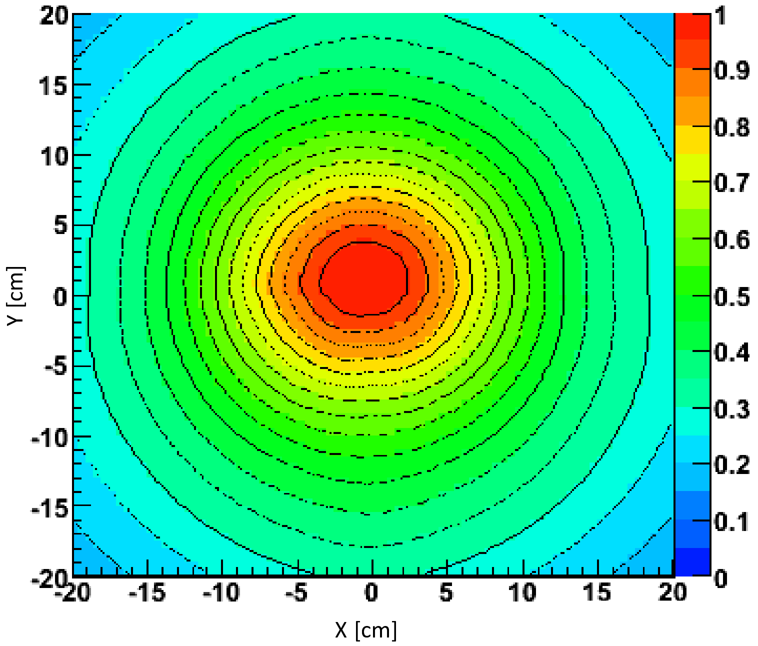

Figure 5.27: Map of the two-dimensional response function.

PSF was also made by point source imaging. Figure 5.28 shows the reconstructed imaging of a ^{54}Mn point source at the center of the TPC ($x = y = 0$), and histogram of its slice image. Here, the slice image was fitted with a best-fit function f_{center} phenomenologically as described following equation consisting of Gaussian G and Lorentzian L

$$\begin{aligned} f_{center} &= \frac{p_1}{\pi}\left(\frac{p_3/2}{(x-p_2)^2+(p_3/2)^2}\right) + p_4 \exp\left(-0.5\left(\frac{x-p_5}{p_6}\right)^2\right) && (5.11) \\ &:= L(x, p_{1,2,3}) + G(x, p_{4,5,6}), && (5.12) \end{aligned}$$

where p_1 to p_6 are fitting parameters.

However, Fig. 5.29 shows ^{54}Mn point source images from the various positions along x-axis, and their functions had an asymmetry form except the center position ($x = y = 0$) of the point source in Fig. 5.28. Thus phenomenological fitting was used following equation instead of equation 5.12.

$$f_{pointspread} = p_8\left(t_1 L(x, p_{1,2,3}) + t_2 \frac{p_7}{p_3} L(x, p_{1,2,7}) + G(x, p_{4,5,6})\right), \tag{5.13}$$

where (t_1, t_2) are $(1, 0)$ for the $0 < x < p_2$ or $0 > p_2 > x$, and $(0, 1)$ for the otherwise.

Here, when we fitted the slice images in Fig. 5.29, we assumed that only p_7 and p_8 are free parameters and the other are fixed parameters which is obtained by fitting in the center position source imaging using the equation 5.12. In addition, the components of the Gaussian fitting was fixed.

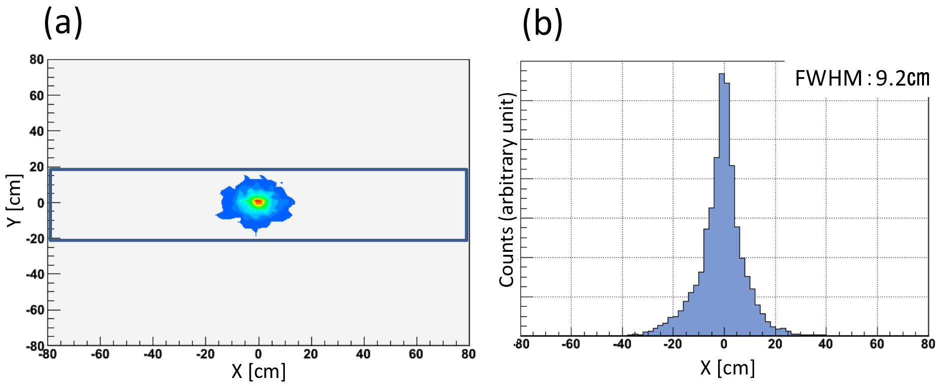

Figure 5.28: (a) Reconstructed image of a ^{54}Mn point source and (b) a projection image from square region in the (a).

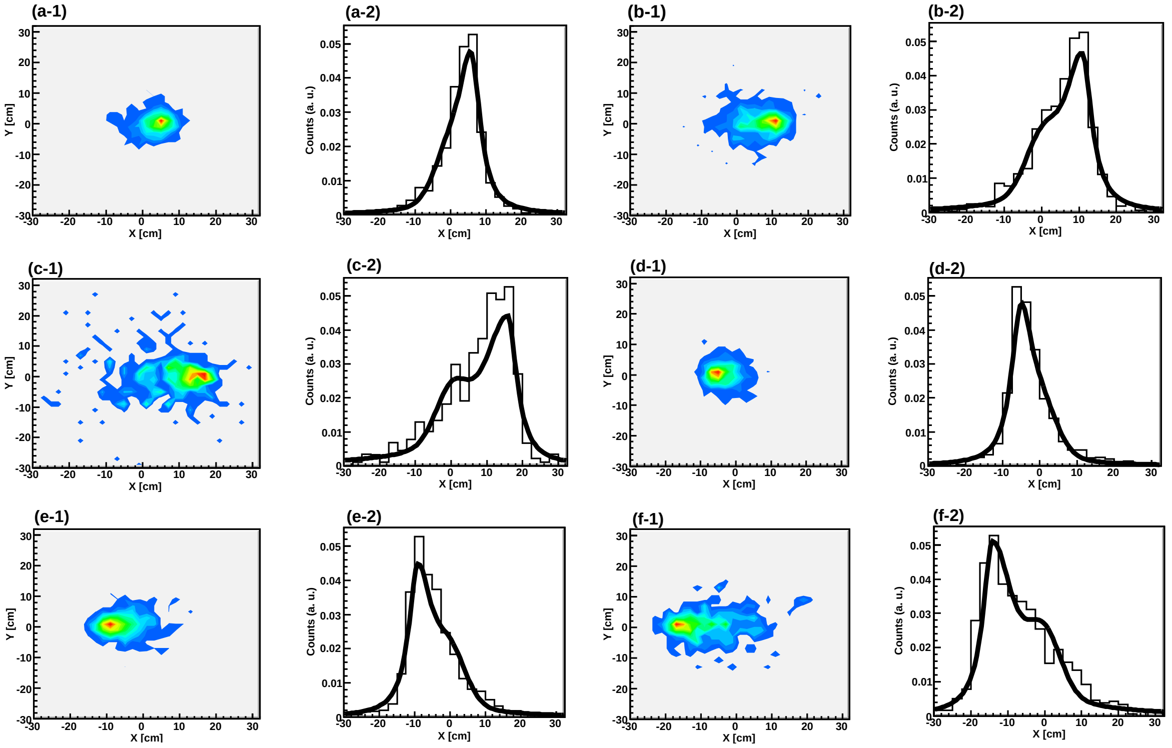

Figure 5.29: ^{54}Mn point source images from various position and their projection images. The setting points of the ^{54}Mn point source were (a):(x [cm],y [cm]) = (5, 0), (b):(10, 0), (c):(15, 0), (d)(-6,0), (e)(-10, 0), (f)(-15,0).

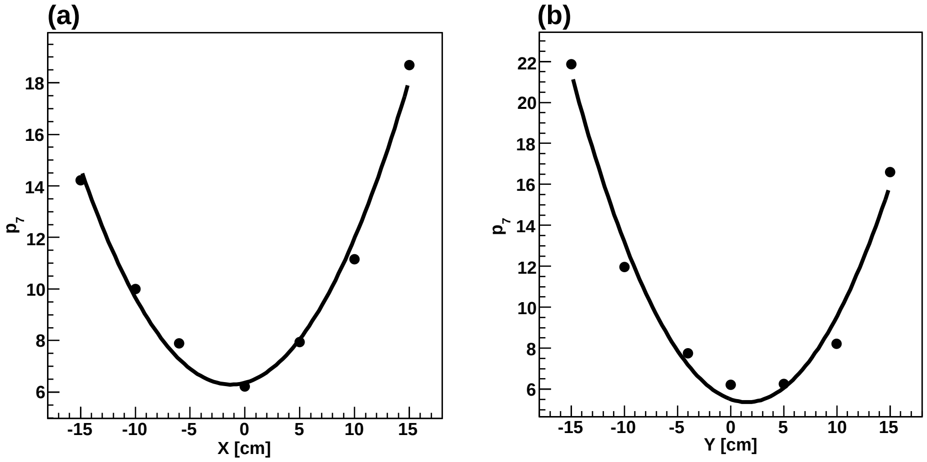

Figure 5.30: Parameter p_7s as a function of the source position for x (a) and y-axis (b).

From the fitting results, the parameter p_7s as a function of the source position along both x and y-axes (Fig. 5.30) were fitted using quadratic functions which are represented the followings

$$p_7(x) = 0.0446x^2 + 0.114x + 6.36 \qquad (\text{for x} - \text{axis}) \tag{5.14}$$

$$p_7(y) = 0.0586y^2 + 0.182y + 5.51 \qquad (\text{for y} - \text{axis}). \tag{5.15}$$

Using the equations 5.14, 5.15, distribution function was described all position along x and y-axes, in fact, Fig. 5.29 shows the fitting results with only a free parameter p_8. In addition, using an assumption of equation 5.10 for the equation 5.14, 5.14, simulated gamma-ray position was spread to the realistic image.

Figure 5.31 shows the energy dependence of the point image for ^{22}Na (511 keV), ^{137}Cs (662 keV), ^{54}Cs (835 keV), (d) ^{22}Na (1275 keV), and (e) ^{88}Y (1836 keV). Like a ^{54}Mn, these images were fitted with f_{center} as shown the equation 5.12, where the Gaussian G part was fitted by fixing the same parameters as the fitting for a ^{54}Mn source image. Figure 5.32 shows the fitting results for slice image of various point sources along x and y-axes. Here, in some energy except the point source energy (511, 662, 835, 1275, and 1835 keV), these parameters were obtained by the arithmetic mean of the parameters between the two point source images. Using the parameters (p_1 to p_6) and equations 5.14, 5.14, a simulated point was also spread to realistic image.

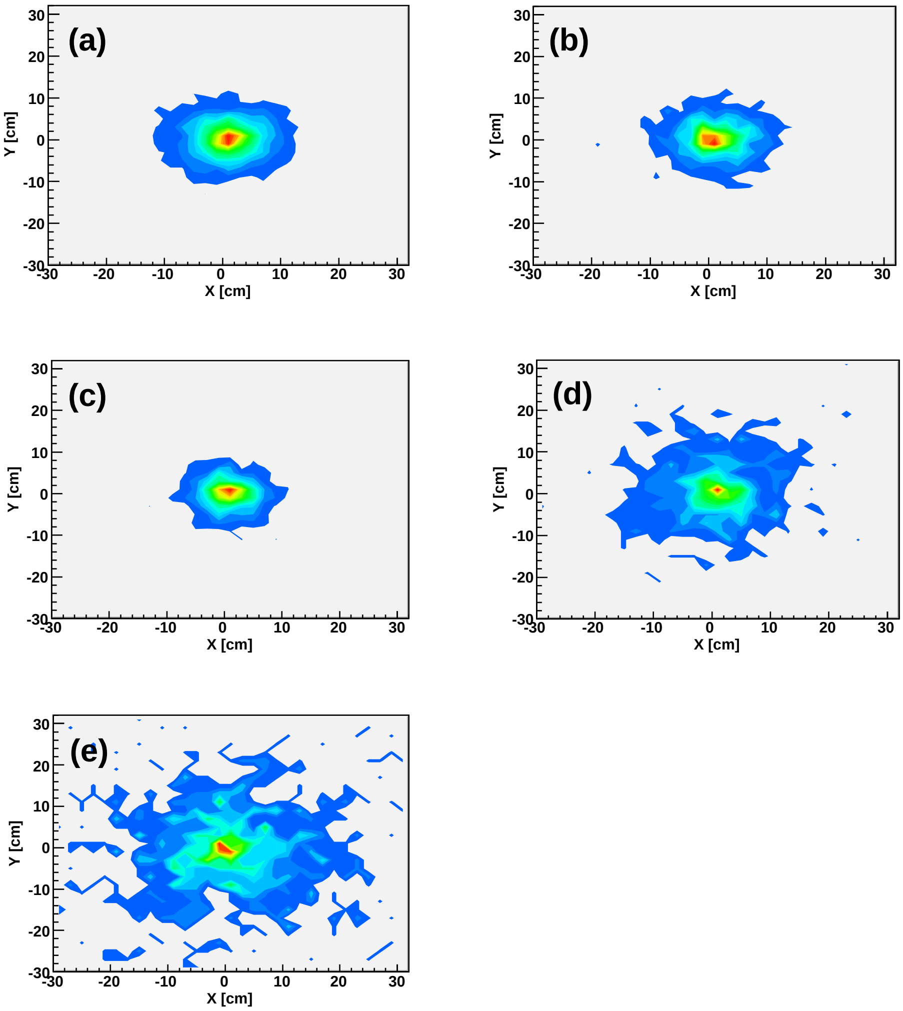

Figure 5.31: Several point source images at $x = y = 0$. (a) ^{22}Na (511 keV), (b) ^{137}Cs (662 keV), (c) ^{54}Cs (835 keV), (d) ^{22}Na (1275 keV), and (e) ^{88}Y (1836 keV).

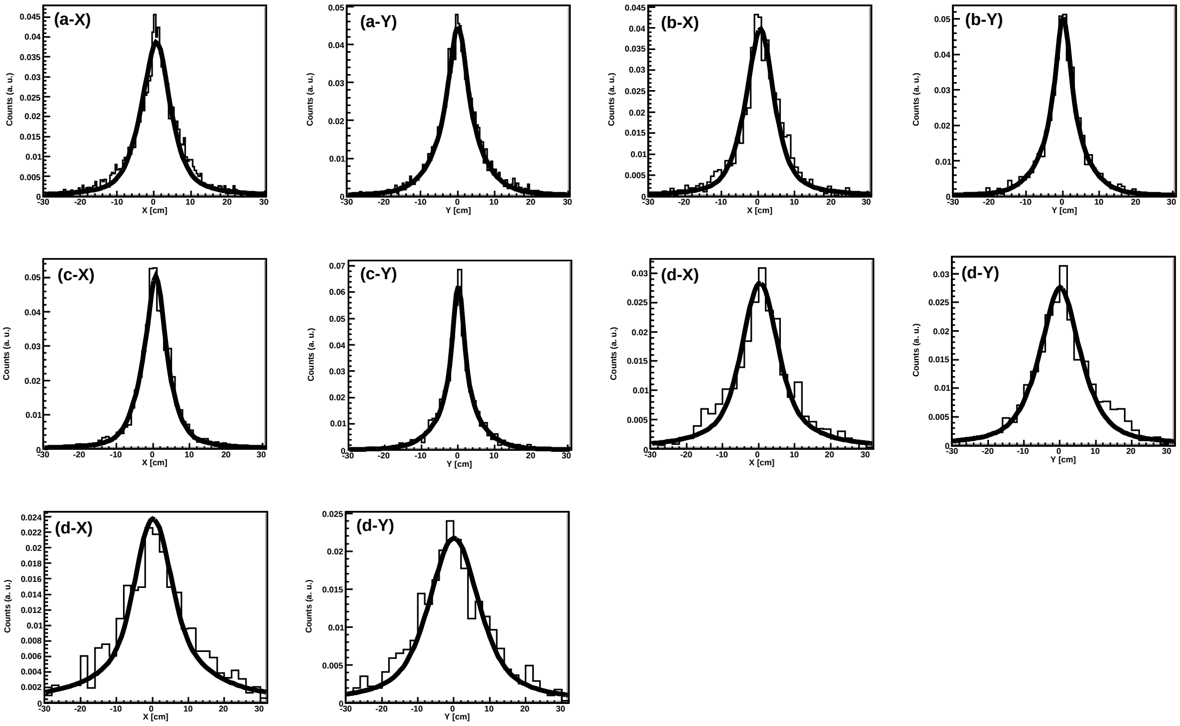

Figure 5.32: Slice image of various point sources along x (X) and y-axes (Y) and their fitting results. (a) ^{22}Na (511 keV), (b) ^{137}Cs (662 keV), (c) ^{54}Cs (835 keV), (d) ^{22}Na (1275 keV), and (e) ^{88}Y (1836 keV).

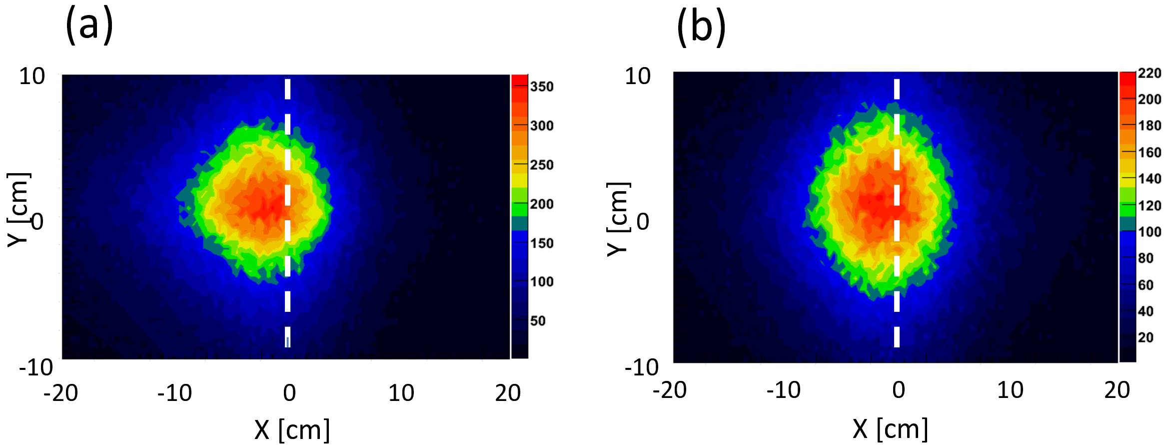

Figure 5.33: simulated images for water phantom irradiated with 140-MeV proton beam. Energy bands are 0.8 - 2 MeV (a) and 463 - 559 keV (b). Broken lines denote the Bragg peak position.

5.4.3 Gamma-ray Imaging

We obtained the simulated images, and Figs. 5.33 (a) and (b) show the images in the gamma-ray energy band of 0.8 - 2 MeV, and 463 - 559 keV, respectively. Their slice images is shown in Fig. 5.34. These results indicated that a peak of gamma-ray distribution for 0.8 - 2 MeV was sharper than for 463 - 559 keV, and this result was consistent with the real data. In addition, both the real data and simulation were found that the position of the gamma-ray peaks for 0.8 - 2 MeV were in upstream of the proton beam at $\sim$ 1 cm from the Bragg peak, while the flat peak ($\sim$ 4-cm width) for 463 - 559 keV was around the TPC center. However, these gamma-ray distributions between the real data and simulation were not the same perfectly. The simulated distributions were sharper than real ones, because we did not consider the random coincidence by neutrons or gamma rays in the simulation. Now we optimize the simulation including the random coincidence.

In Fig. 5.33, we considered reaction functions of the ETCC, $F(X, Y, E)$ including PSFs, and the reaction functions depended on the emission position and the gamma-ray energy (Fig. 5.35).

Conversely, the real map of the gamma-ray emission distribution can be reconstructed from the measured images with the ETCC using the inverse reaction function $F^{-1}(X, Y, E)$. In deed, some reconstruction methods corresponding to $F^{-1}(X, Y, E)$ such as the maximum likelihood expectation maximization (ML-EM) algorithm [162] is available in medical imaging such as PET and SPECT. Figure 5.22 was not applied to $F^{-1}(X, Y, E)$, and the deconvolution to the ETCC image is also required like PET and SPECT images.

In medical imaging, the line gamma-ray source is used, while we need detect continuum gamma rays. Thus the inverse function $F^{-1}(X, Y)$ for medical imaging dose not depend on only the position. However, these reconstruction methods have not been applied to continuum

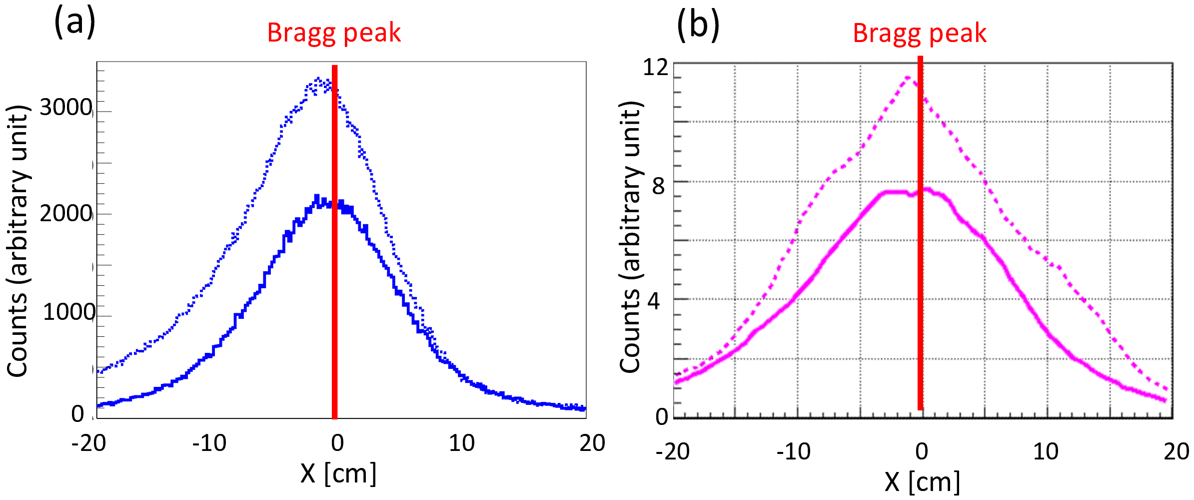

Figure 5.34: (a)simulated slice images for Fig. 5.33. (b) measured slice images for Fig. 5.22. (dotted line:0.8 - 2 MeV, solid line:463 - 559 keV).

gamma-ray image, and it is difficult to optimize the inverse function $F^{-1}(X, Y, E)$. Therefore I study the inverse function $F^{-1}(X, Y, E)$ for proton therapy using point gamma-ray source images with various energies that I set and measured in various positions.

Due to a wide energy range, we succeeded in imaging for higher energy band and around 511 keV simultaneously, and we obtained the different images between the high energy prompt gamma rays and low energy including annihilation gamma rays. However the spatial resolution of the ETCC was 2.2 cm (FWHM) at 835 keV in this experiment, and it was not sufficient to estimate quantitative position and to use in medical. At least the spatial resolution is required to be 1.0 cm in medical, Therefore we should improve the angular (spatial) resolution of the ETCC, and we have developed an ETCC with a better angular resolution as described in Chapter 6.

5.5 Future Works

For proton therapy and astronomy, we need an ETCC with a higher detection efficiency. In addition, the ETCC should measure the higher energy gamma rays ($\geq$ a few MeV) with a sufficient detection efficiency in order to verify the proton dose more clearly. However, we did not measure higher energy gamma rays more than 2 MeV, because of the low efficiency of the ETCC. Then we improve several factors for the detection efficiency as written followings.

Multi-head imaging Measurement of a target using several ETCCs simultaneously is not only effective to have higher detection efficiency, but to obtain a three-dimensional imaging.

Larger size ETCC We have developed a larger size TPC up to 40 cm-size by combining four 20-cm-size μ-PICs.

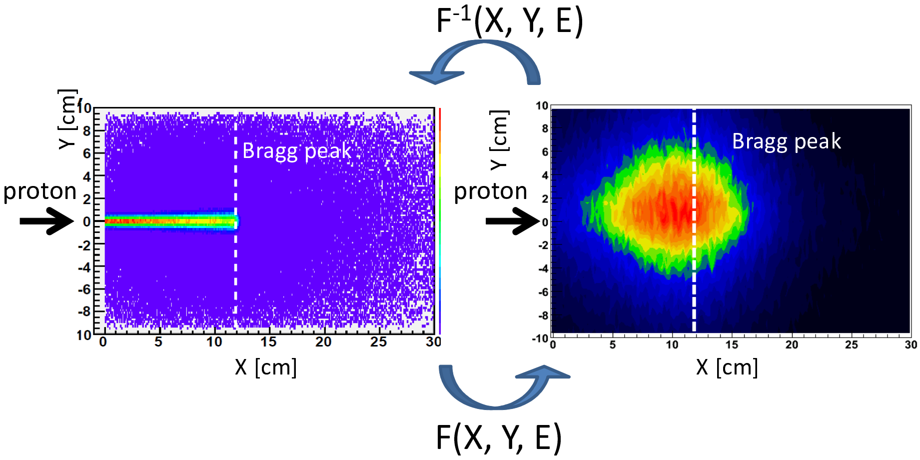

Figure 5.35: Ideal gamma-ray and simulated image with the reaction function of the ETCC.

Optimization of the gas Optimizations of the gas such as CF_4-based gas, and its pressure are also effective to obtain the higher detector efficiency. Actually, a detection efficiencies of 356-keV gamma rays were 2.44×10^{-5}, 3.51×10^{-5}, and 1.81×10^{-5} for CF_4-based mixture gas (Ar (54%) + CF_4 (40%) + isoC_4H_{10} (6%)) at 1, 1.4 atm, and Ar (90%) + C_2H_6 (10%) gas at 1 atm, respectively [113].

Optimization of data acquisition logic The coincidence between the anode and cathode hit information in the TPC is sometimes not effectively detected, and we improve a novel logic as shown in section 4.1.

In this beam test, we used low current proton beam than usual current in the therapy ($\sim$ 1 nA) by an order of 2 to 3, because of keeping imaging quality due to the random coincidence. In this test, we operated with an ETCC count rate of approximately $20 - 30$ Hz, and the dead time of the ETCC is over 50% when the count rate become approximately 50 Hz. In order to use the ETCC as clinical applications in proton therapy, we must overcome to endure the high count rate, and reduce the random coincidence. Then the solutions and improvement points as a future works are shown as followings.

(a) Optimization of the gas and data acquisition logic The drift time of the recoil electron is up to 4 - 5 μsec in the TPC (10 cm $\times$10 cm $\times$15 cm), Thus in the Field-Programmable Gate Array (FPGA) code of the encoder, we now set a time window of 8 μsec after the trigger to determine (hereafter referred to as "drift waiting"). The total dead time, defined as the veto time duration, was 10.5 μsec per a trigger. CF_4-based gas (e.g. CF_4 + Ar + C_2H_6) has a faster drift velocity by roughly 2 times as compared to the current setup (Ar + C_2H_6 gas). Thus, we can reduce the "drift waiting" in the TPC by a factor of $\sim$ 2.

(b) Pixel reading for scintillation array In order to prevent random coincidence, it would be effective to read each pixel scintillator without a resister chain board and charge-division method described in section 4.4 .

(c) Optimization of the signal digitalization of scintillation A charge analog-digital converter (CADC) is expected to read signals from scintillator faster than a peak-hold ADC (PHADC), because the gate duration of CADC is shorter. (PHADC: a few μsec, CADC: $\sim$ 100 nsec). Although the PHADC is used generally in our ETCC, we will test the CADC.

(d) Hardware threshold / Lead shield for the monitor of proton therapy, the target gamma rays has higher energies ($\geq$ 1 MeV). Thus rejection of the lower energy gamma rays with a hardware threshold or lead shield in front of the TPC is effective to reduce the dead time.

(e) Detection of the energy distribution along the electron track The energy of the recoil-electron is measured only total energy for a one Compton event now. When the energies are measured at each hit point in the μ-PIC, we obtain the Bragg curve of the recoil-electron Compton event-by-event. Thus, the μ-PIC and TPC would discriminate between the recoil-electron event and the random coincidence, and then the tracking ability is expected to improve.

(f) Trigger Since scintillation hit is used for an ETCC trigger, it is likely to be contamination of the background gamma rays coming out of the TPC. Here, Gas scintillation light in the TPC might be used as the trigger.

We already began to test the solutions (a) and (b). As a first step of (a), we measured a point source with an ETCC containing the above CF_4-based at 1 and 1.4 atm with the same data acquisition logic which is "drift waiting" of 8 μsec. The FWHM ARMs were 11.7 ± 0.4, 11.2 ± 0.3, and 10.4 ± 0.7 for the CF_4-based gas at 1, 1.4 atm, and Ar (90%) + C_2H_6 (10%) gas at 1 atm, respectively [113]. The ETCC with CF_4-based gas did not have a worse angular resolution remarkably. Therefore, these gas is expected to reduce the dead time.

For the solution (b), we have developed a 64-ch read out system named Head Amp Unit CP80190 (Clear Pulse) as shown in Fig 5.36, and we measure each pixel signal from an 8×8 $LaBr_3$:Ce array coupled to an 8×8 multi-anode PMT. The FWHM energy resolution was 5.4% at 662 keV, and it is similar resolution as compared to a conventional reading as described in Chapter 4 and 6. As a next step, we estimate an ETCC using the this system. The solution (c) is not difficult technique. However, (c) is not needed when we succeeded in the improvement with (b), because the 64-ch read out system include the ADC.

(d) is also not difficult technique, and we tested it in the next experiment. The solution (e) have been developed, and we have already applied to the neutron imaging [114]. Then we apply the solution (e) to the ETCC. The solution of (f) is just difficult technique, because the gas scintillation light is so week, and the spark light near the GEM or μ-PIC might contaminate the

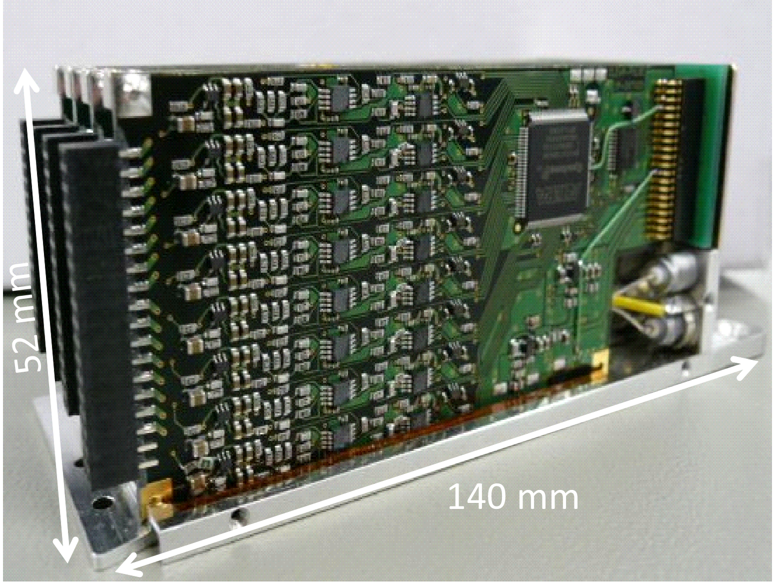

Figure 5.36: Photograph of the 64-ch read out system named Head Amp Unit CP80190 (Clear Pulse).

gas scintillation light. Due to the discrimination of the gas scintillation light efficiently, many photon detectors might be required in the TPC, because the distribution of the gas scintillation emission is different from the that of other noise. Thus we research and develop the a novel trigger using some photon detectors such as a PMT, an avalanche photodiode, and Multi-Pixel Photon Counter.

From the above improvement, the ETCC is expected to endure the beam current with over 150 times higher than that of current measurement. This will allow the ETCC to monitor the location after a few seconds at the beam current of $\sim 0.5 - 1$ nA. As a result, the ETCC would be used in proton therapy after the further developments.

Chapter 6

Improvement of Scintillator

6.1 Position-Sensitive Scintillation Camera

In this section, I have developed a new scintillation camera with position sensitivity, in order to obtain a better angular resolution of the ETCC. At first, I briefly mention which type of the position-sensitive scintillation camera is suitable for the ETCC.

Position-sensitive scintillation cameras are used in various fields such as medical imaging [115] and gamma-ray astronomy [116, 117, 118]. Figure 6.1 shows the various types of a position-sensitive scintillation camera as listed below.

(a) Anger-logic camera [119, 120]

(b) Photomultiplier tube (PMT)-Quadrant-Sharing technology [121, 122]

(c) Planar type [123]

(d) Array camera consisting of a scintillator array in which every pixel is read with a position-sensitive PMT [124, 125]

The Anger logic camera consisting of a large one crystal plate and PMTs as shown in Fig. 6.1 (a), measures the position by calculating a weighted centroid of the charge deposited in several photo-sensors such as a PMT. This algorithm looks simple, but causes several problems of the spatial non-linearity, especially near the image edges [125]. Figures 6.1 (b) and (c) are one of the improved Anger-logic cameras, which have pixellation structures. These structures limit the scintillation light path, and hence improves the spatial non-linearity at some level. This crystal with the structures is called "planar" (Fig. 6.1 (c)). In particular, when the positioning system, which uses four single-anode PMTs on the four corners of the crystal, is called PMT-Quadrant-Sharing technology (Fig. 6.1 (b)). Pixel array type measures the position of a hit pixel directly from the hit position of a position-sensitive detector as shown in Fig. 6.1 (d).

In this paper, I describe a crystal without pixellation structures as a "continuous crystal". The continuous crystal is read with Anger-logic, and it has the advantages of structural simplicity, and lower cost. On the other hand, a pixel array camera has the advantages of an intrinsic spatial resolution dictated by crystal pixel width. Emitted light was focused within the pixel

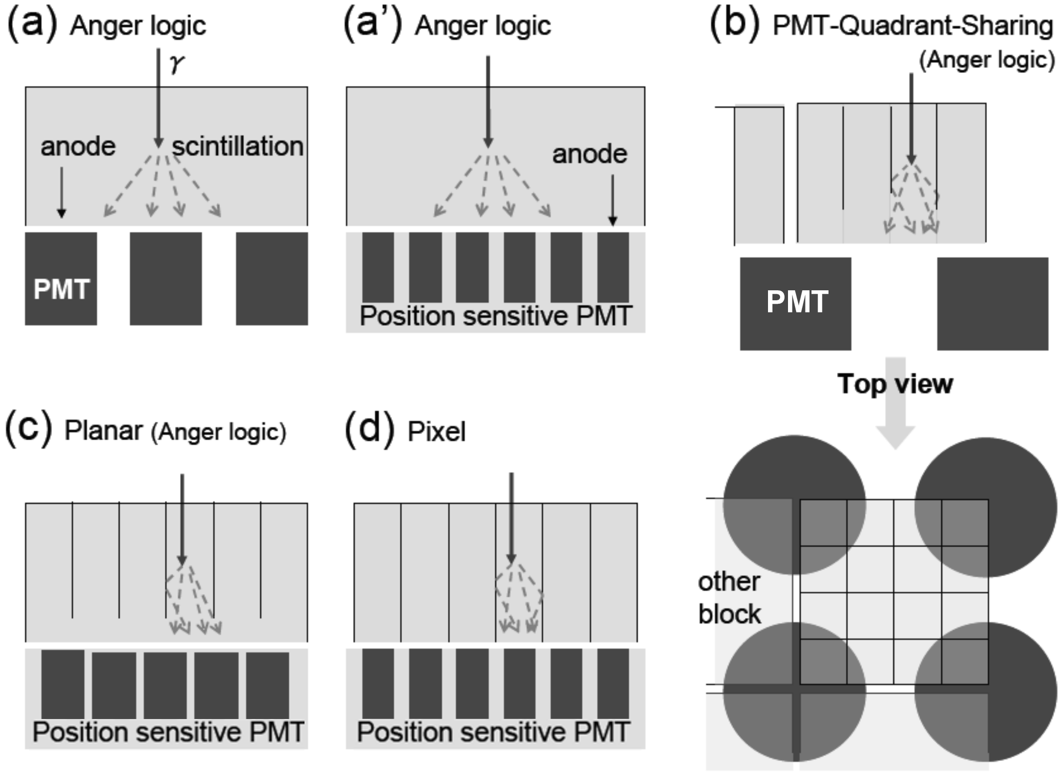

Figure 6.1: Schematic view of position-sensitive scintillation camera. (a)and (a') are Anger logic system using single anode PMTs and a multi-anode PMT, respectively. (b), (c), and (d) are PMT-Quadrant-Sharing, planar, and pixel type, respectively.

area via a reflector [126]. In addition, a thick continuous crystal has a three-dimensional position sensitivity because PMT signals in an Anger camera have a marked dependence on the depth of gamma-ray interactions [127]. However, a thick continuous crystal generally has a worse spatial resolution near the edges of the detector than near the center [125, 128, 130]. Approximately, 30 % area in the continuous crystal is not an effective area keeping a good and uniform spatial resolution [125, 130]. On the other hand, an array camera has a uniform spatial resolution over the whole area [128].

In our Compton camera, we adopted the array type scintillation camera because of the uniform spatial resolution over the entire area. The array camera is able to avoid the necessity of the position calibration in space. The array also has the ability to discriminate multi-hit events when multiple scattering occurs between different pixels by Compton scattering in the pixels or the detector is under the high count rate condition especially in medical imaging. Also from the limitation of the weight in space, an array camera is superior to an Anger camera due to the use of the whole area of the scintillator.

6.2 Optimizing the Scintillator and the Pixel Size

6.2.1 Use of Hygroscopic Scintillator

Owing to the feasibility of the array type camera for the ETCC, we first developed an array camera consisting of an 8 × 8 array of GSO:Ce scintillator pixels using a 3M Vikuiti ESR^{TM} reflector. The pixel size was 5.9 mm ×5.9 mm ×13.0 mm, and a pixel pitch was 6.1 mm.

GSO:Ce has some merits for the ETCC as followings. GSO:Ce has a shorter radiation length of 13.8 mm and a shorter decay time of 30 - 60 ns (depending on the amount of doped Ce) than NaI:Tl and CsI:Tl [132, 133, 134, 135]. In addition, GSO:Ce is nonhygroscopic, and no hermetic package is needed. Therefore, an assembly of an array is simpler. On the other hand, NaI:Tl and CsI:Tl are hygroscopic and needed a hermetic package. Moreover, GSO:Ce is less susceptible to radiation damage than either NaI:Tl or CsI:Tl [136]. These are inevitable requirements for detectors used in space.

Here, we have to optimize the angular resolution measure (ARM) of a Compton camera, which depends on the the energy resolution of the scintillator. In principle, a better energy resolution scintillator certainly improves the angular resolution of the ETCC.

Owing to pixellation structures, the array camera tends to have a lower energy resolution than a continuous crystal. Especially, the energy resolutions of hygroscopic scintillators are more likely to be worse. However, some array cameras already provided a better energy resolution. For example, Lee et al. have reported that a NaI:Tl array with a pixel size of 2 mm ×2 mm ×10 mm achieved a FWHM energy resolution of 7.37% at 662 keV using a crossed-wire anode PMT (Hamamatsu R3292)[137]. In contrast, our GSO:Ce array coupled to a multi-anode PMT (H8500) had an FWHM energy resolution of $\sim$ 10.5% at 662 keV [131]. Although the NaI:Tl has hygroscopic nature, and the pixel size is smaller than ours, the NaI:Tl array keep energy resolution that monolithic one has. In addition, it has a better energy resolution than GSO:Ce array.

Since NaI:Tl scintillator has a week radiation hardness, the use of the NaI:Tl array is difficult in the space. In addition, because a decay constant time of NaI:Tl is long (approximately 250 nsec) than other scintillators, the signal from the NaI:Tl is likely to pile-up under the high-count rate condition, especially for medical imaging. Therefore we tried to develop a new scintillator array with a better energy resolution except NaI:Tl, even if the crystal has hygroscopic nature.

6.3 ARM Calculation for the Selection of a Scintillator and the Pixel Size

For the designing the new array, I studied the detail of the ARM of an ETCC by simulation. The ARM depends on not only the energy resolution, but also the pixel size of the scintillator. Therefore, I estimated which factor mentioned below is more efficient for the improvement of the angular resolution.

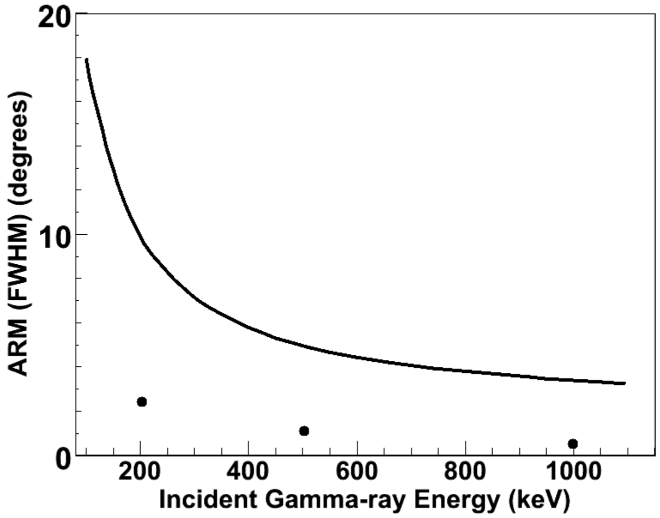

Figure 6.2: Dependence of the angular resolution measure (ARM) on the incident gamma-ray energy (solid line), using a scintillator with an FWHM energy resolution of 10.5 % at 662 keV. Filled circles denote the lower limit by Doppler broadening for argon gas [95]

The first factor is the pixel pitch. Figure 6.2 shows the simulated ARM as a function of the incident gamma-ray energy for 6 mm ×1 mm ×13 mm pixels. Here, this calumniation has been done based on the following assumptions:

1) Compton scatterings occur in the TPC with a volume of 10 cm ×10 cm ×10 cm, filled with argon (90%) and ethane (10%) gas at 1 atm.

2) We arrange 3 × 3 arrays, which consist of 8 × 8 pixels, below 5 cm from the bottom of the TPC.

3) The energy resolution of the scintillator is 10.5% at 662 keV (FWHM), which is typical for GSO:Ce.

4) The energy resolution of the recoil electron in the TPC is 30% at 22 keV (FWHM).

5) There is no error in the measurement of the Compton scattering position with the TPC.

6) Doppler broadening is taken into account.

Table 6.1 summarizes the dependence on the spatial resolution of the GSO:Ce scintillator array. The dependence of the ARM angular resolution on the pixel pitch shows that even if the pixel size is 1 mm ×1 mm ×13 mm, the ARM is improved only from 5.2° to 4.9° at 662 keV (FWHM).

Second, the ARM dependence on the thickness of (height) the scintillator is listed in Table 6.2, for 6-mm pixel pitch. It is found that thinner pixel has a better angular resolution of

Table 6.1: ARM dependence on the spatial resolution of the GSO:Ce array

pixel size length × width × thickness [mm × mm × mm]	FWHM ARM at 662 keV [degrees]
6 × 6 × 13	5.2
3 × 3 × 13	5.0
2 × 2 × 13	4.9
1 × 1 × 13	4.9

Table 6.2: ARM dependence on the pixel height with an FWHM energy resolution of 10.5 % at 662 keV.

pixel height [mm]	FWHM ARM at 662 keV [degrees]
15.0	5.4
13.0	5.2
6.5	4.9
3.0	4.7

the Compton camera, though a thinner crystal have a lower detection efficiency. Here, the attenuation length of the GSO:Ce is 14.2 mm at 511 keV [151], and a height shorter than ∼10 mm is not enough to detect gamma rays with an energy of over 500 keV.

The dependence of the ARM angular resolutions on the energy resolution of the scintillator is listed in Table 6.3, assuming a 6 mm ×6 mm ×13 mm scintillator pixel and the above assumptions 1), 2) and 4) - 6). For the scintillator with an energy resolution of 3.0 %, the ARM is improved to 3.8° at 662 keV (FWHM).

In the above calculations, we ignored the contribution of the spatial resolution of the TPC on the ARM. The contribution of the TPC spatial resolution of ∼ 0.4 mm (1 σ) [38] to the ARM was estimated to be ∼ 0.3° at 662 keV, which is small compared to the contribution to scintillator here.

Tables 6.1, 6.2 and 6.3 show that the improvement of the energy resolution of the scintillator is more effective in obtaining a better angular resolution than improving the position resolution of the scintillator. Table 6.2 suggests that the improvement due to the determination of the depth of interaction (DOI) [138, 139, 140, 141], looks small for GSO:Ce. Table 6.3 also shows

Table 6.3: ARM dependence on the energy resolution of the scintillator

FWHM energy resolution of scintillator at 662 keV [%]	FWHM ARM at 662 keV [degrees]
10.5	5.2
7.0	4.5
5.0	4.0
3.0	3.8

that the effect of the improvement is small when a scintillator has an energy resolution of better than ~ 5 % (FWHM) at 662 keV.

Therefore, those studies indicate the necessity of a new scintillator with a better energy resolution and the goal of the energy resolution is ~ 5 % (FWHM) at 662 keV in order to achieve an ARM of approximately 4° (FWHM) at 662 keV. Additionally the pixel pitch is enough to be 6 mm which is the same size as a GSO:Ce array.

6.4 $LaBr_3$:Ce Camera

In the chapter 4, Fig. 4.1 shows the features of various scintillators. A $LaBr_3$:Ce looks a better candidate as a replacement for a GSO:Ce, because of its excellent energy resolution. The typical energy resolution is 3% (FWHM) at 662 keV [142, 143, 144, 145, 146], which is independent of the crystal size from 4 mm $\times$4 mm $\times$5 mm up to ϕ 51 mm $\times$76 mm [144, 147].

$LaBr_3$ crystals doped with 0.5 mol% and 5 mol% Ce have primary (~ 90 %) decay times of 26 and 15 nsec, respectively. In addition, they have high light yields of $\sim 6 \times 10^4$photons/MeV (~ 160% of NaI:Tl; ~ 820 % of GSO:Ce) [142, 143, 144, 145, 146, 148]. The radiation hardness of $LaBr_3$:Ce is also very good [149, 150].

On the other hand, $LaBr_3$:Ce has several disadvantages. One is hygroscopic, and another is a long attenuation length of $LaBr_3$:Ce of 2.1 cm at 511 keV, which is 1.4 times longer than that of GSO:Ce [151, 152]. Therefore the detection efficiencies for gamma rays in $LaBr_3$:Ce through photo-absorption and Compton scattering are 0.21 and 0.51 at 500 keV for a thickness of 5 and 15 mm, respectively. However, the main aim is to improve the angular resolution of ETCC. Although the detection efficiency is worse, we have developed a $LaBr_3$:Ce array camera without DOI as a first step.

Position-sensitive detectors made of $LaBr_3$:Ce have been reported by several groups [153, 129, 150, 155, 130, 156, 157, 158]. Kuhn et al. measured a $LaBr_3$:Ce 10×10 array with a pixel size of 4 mm $\times$4 mm $\times$30 mm in an Anger-logic detector [154]. Pani et al. [129] and Bloser et al. [153] measured a 10-mm thick continuous $LaBr_3$:Ce crystal with 3-mm and 1-mm thick optical windows, respectively, using a multi-anode PMT. Case et al. [157] and Budden et al. [158] used layers of wavelength-shifting fibers arranged parallel to the surface of the $LaBr_3$:Ce crystal to measure a two-dimensional position. Two orthogonal layers were used and read out at the end of the fibers by a multi-anode PMT. On the other hand, to measure the energy, the $LaBr_3$:Ce crystal was read out using a single-anode PMT viewing through the fiber layers. However, a $LaBr_3$:Ce array has not yet been measured with a multi-anode PMT which has the same area of the anode as the pixel.

To improve both the energy and angular resolutions of the ETCC, we have assembled a $LaBr_3$:Ce array. The array has the same pitch of crystal pixel as that of the anode array in a multi-anode PMT, and a thickness of pixel was chosen to be 15 mm for detecting sub-MeV gamma rays. Here, I describe the evaluation of the energy resolutions of the $LaBr_3$:Ce array coupled to a multi-anode PMT (H8500) for gamma-ray energies between 122 and 835 keV. Also obtained results are compared to those obtained with the GSO:Ce array described above using the same PMT and readout system.

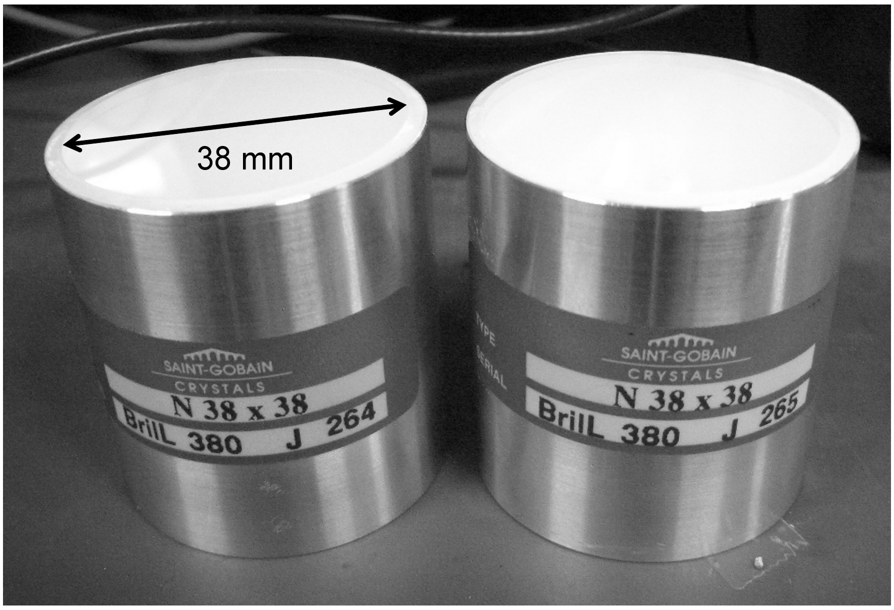

Figure 6.3: Photograph of LaBr$_3$:Ce crystals #1 (left) and #2 (right) with sizes of ϕ38 mm ×38 mm.

6.5 Materials for LaBr$_3$:Ce Array Camera

6.5.1 Energy resolutions of the monolithic LaBr$_3$:Ce crystals by whole irradiation

Our array was constructed from two blocks of LaBr$_3$:Ce crystal, hereafter #1 and #2, of a 5 mol% Ce-doped monolithic LaBr$_3$ BrilLanCe 380^{TM} [159] crystal with a size of ϕ38 mm ×38 mm (Fig. 6.3).

First we checked the energy resolutions of those monolithic crystals. Two monolithic crystals were measured using a 2-inch single-anode PMT (Hamamatsu R6231 [160]) with an optical grease (OKEN 6262A [69]). for irradiation of the entire crystal by gamma rays from radioisotopes.

Table 6.4 lists the FWHM energy resolutions of #1 and #2. Figure 6.4 shows the FWHM energy resolutions of the crystals from 81 to 1275 keV. Best-fit lines for the data points of #1 and #2 are represented as the following equation 6.1 with $\alpha = 3.10 \pm 0.03$, $\beta = 0.545 \pm 0.002$, and $\alpha = 3.06 \pm 0.03$, $\beta = 0.543 \pm 0.002$, respectively,

$$\text{resolution}(\%) = \alpha \times \left(\frac{E}{662\text{keV}}\right)^{-\beta} \tag{6.1}$$

There was no significant difference in the energy resolutions between #1 and #2. In addition, this results is the same as the typical FWHM energy resolution of the LaBr$_3$, which shows the goodness of those two monolithic crystals.

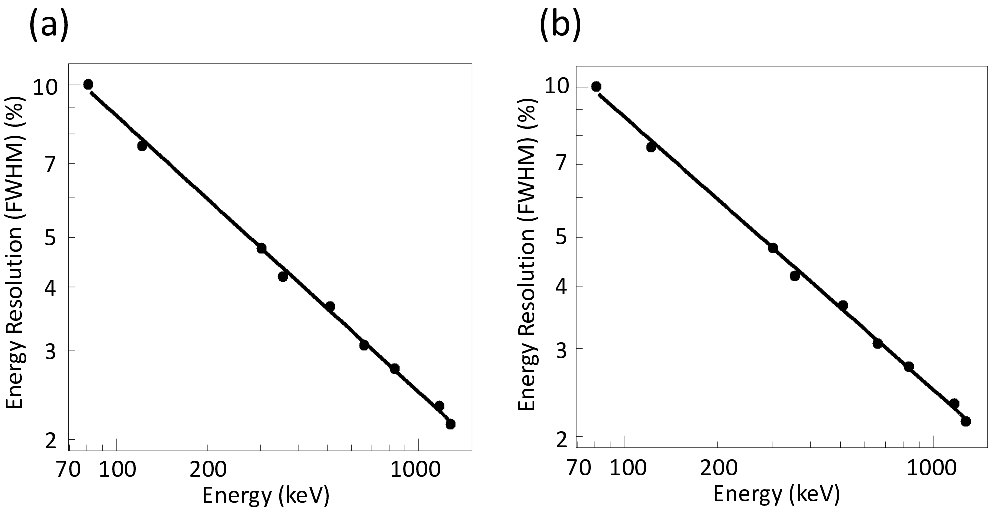

Figure 6.4: Energy resolutions of $LaBr_3$:Ce crystals #1 (a) and #2 (b), which were cut into pixels in an array.

Table 6.4: FWHM energy resolutions of monolithic $LaBr_3$:Ce

crystal number	Energy (keV)	Energy resolution (%)
# 1	356	4.19 ± 0.02
	662	3.06 ± 0.01
# 2	356	4.12 ± 0.02
	662	3.01 ± 0.01

6.5.2 Uniformity of Light Output and Energy Resolution

Since those crystals have a large size of ϕ38 mm ×38 mm, there is a possibility that they have a position dependences of the light output and energy resolution. Thus we measured the uniformity of the light output and energy resolution by irradiating the crystals with gamma rays from a collimated ^{133}Ba source. The beam was formed using a 70-mm long Pb collimator with a 2-mm diameter opening. The points from d1 to d6 in Fig. 6.5 were irradiated with gamma rays from the vertical direction to the side of the crystals.

The ratios of the light output at each point to the value at point C of Fig. 6.5 are shown in Fig. 6.6. The difference was plotted within 2%. The average and standard deviation (SD) of #1 and #2 are listed in Table 6.5. The FWHM energy resolutions at 356 keV are shown in Fig. 6.7. The average and SD values of #1 and #2 are also listed in Table 6.5. The SD of the light output are approximately 0.5 % of the mean at 356 keV, while Iltis et al. reported that the SD

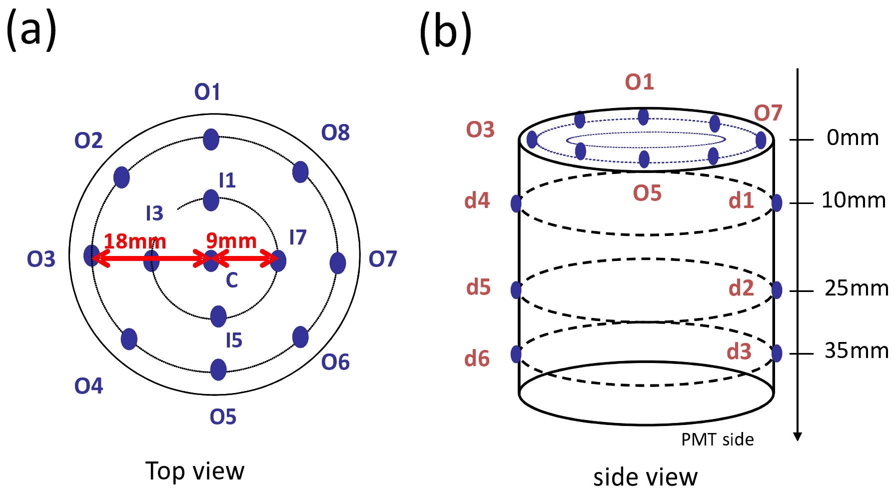

Figure 6.5: Filled circles denote points where collimated gamma rays from a ^{133}Ba source were irradiated. (a) top view, (b) side view.

Table 6.5: Uniformity of Monolithic LaBr$_3$:Ce

		mean ± SD
Light output at 356 keV	#1	1.003 ± 0.005
	#2	1.006 ± 0.005
FWHM Energy resolution at 356 keV	#1	4.10 ± 0.07
	#2	4.08 ± 0.07

is 0.4 % at 662 keV.

Although we and Iltis et al. used different gamma-ray sources and the materials including PMT, the both variations for the light output are similarly small [147]. Also the energy resolutions of #1 and #2 have small variations. Thus our crystals are considered good to make a pixel material for an array. In addition, the array is expected to have a uniformity of energy resolution within a few percent, if we make a pixel ideally.

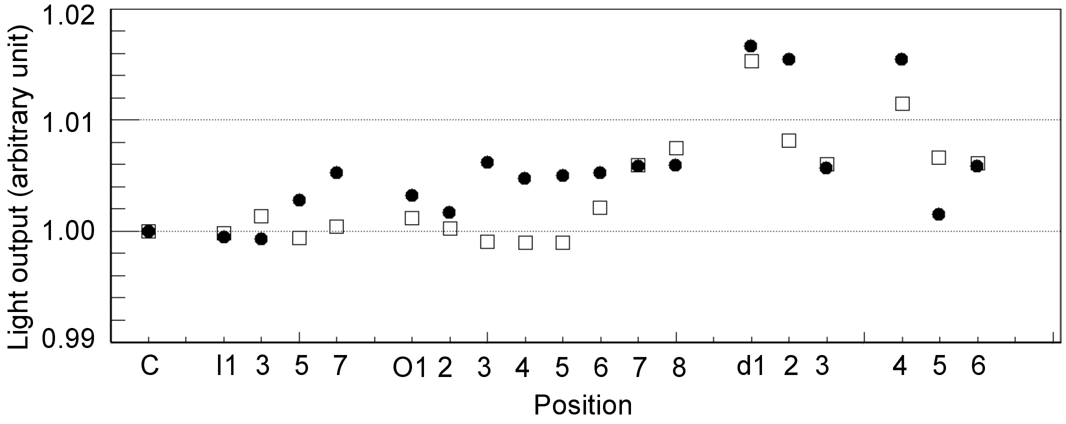

Figure 6.6: Uniformities of light outputs of the LaBr$_3$:Ce crystals #1 (squares) and #2 (filled circles) at positions shown in Fig. 6.5.

6.6 Assembly of LaBr$_3$:Ce and GSO:Ce arrays

These ϕ 38-mm LaBr$_3$:Ce crystals were cut into 64 pixels with a size of 5.8 mm ×5.8 mm ×15 mm. At the same time, we studied what kind of crystal surface is able to keep the energy resolution. In this process, we had to develop the cutting and polishing method by ourselves, though we cannot describe the details for claiming the patents. In this study, we adopted a rough surface of the pixel. Figure 6.8 shows the photograph of LaBr$_3$:Ce pixels cutted by our own technique. Each pixel is wrapped with TETRATEX^{TM} as a reflector. Figure 6.9 shows an FWHM energy resolution of LaBr$_3$:Ce pixel without hermetic package as a function of the energy measured by the 2-inch single-anode PMT (Hamamatsu R6231). Owing to hygroscopic nature, the pixel was measured under dry condition. Best-fit line for the data points in Fig. 6.9 is represented as $\alpha = 3.5 \pm 0.5$,and $\beta = 0.47 \pm 0.02$, where α and β are described in equation 6.1. We succeeded in keeping the energy resolution of LaBr$_3$:Ce after the cutting. For comparison with a LaBr$_3$:Ce, we also measured a GSO:Ce pixel with a size of 5.9 mm ×5.9 mm ×13 using the 2-inch single-anode PMT (Hamamatsu R6231). Best-fit line for the FWHM energy resolution as a function of the energy was represented as $\alpha = 8.2 \pm 0.1$, $\beta = 0.497 \pm 0.003$.

Next the pixels were assembled into an 8 × 8 array with a pixel pitch of 6.1 mm using a TETRATEX^{TM} reflector as shown in Figs. 6.10, and 6.11. The total volume of the crystal was 49 mm ×49 mm ×15 mm. Due to hygroscopicity, the array was sealed in a hermetic package

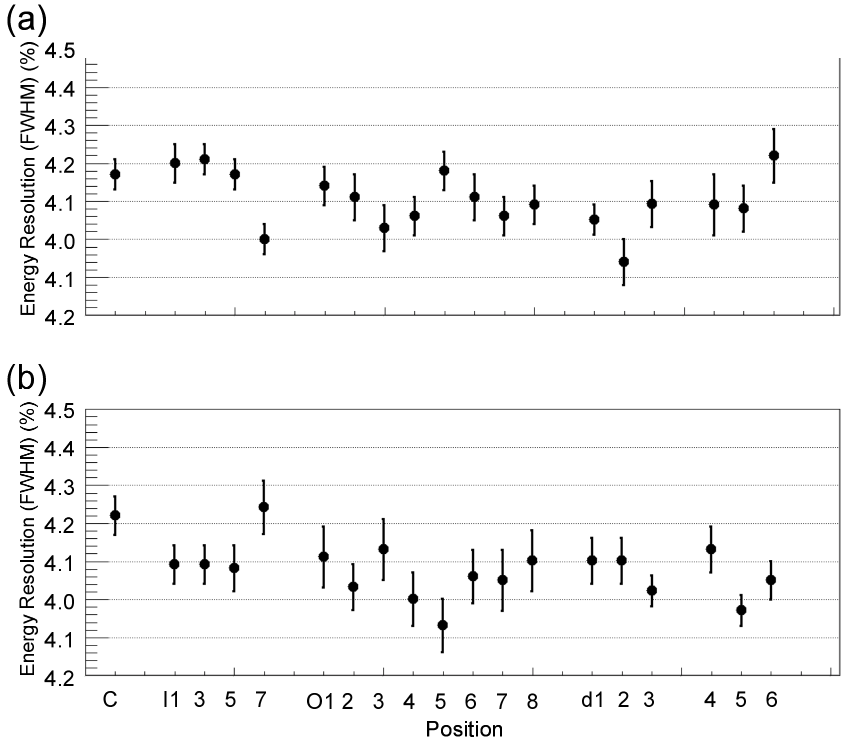

Figure 6.7: Uniformities of energy resolutions of the LaBr$_3$:Ce crystals #1 (a) and #2 (b) at positions shown in Fig. 6.5.

with a volume of 62 mm ×62 mm ×20 mm, which had a quartz window with a volume of 58 mm ×58 mm ×3 mm on the PMT side, and aluminum plates with a thickness of 0.5 mm on the remaining sides. Because sealing the LaBr$_3$:Ce crystal requires an adhesive-bonding surface between the window and the aluminum package, the area of the window was larger than that of the crystal array.

For comparison with the LaBr$_3$:Ce array, we also assembled an 8 × 8 array of 0.5 mol% Ce-doped GSO pixels with a size of 5.9 mm ×5.9 mm ×13 mm with a pitch of 6.1 mm using a 3M Vikuiti ESR^{TM} reflector (Fig. 6.12) [131]. The GSO:Ce array had neither a hermetic package nor a quartz window without hygroscopicity.

Since the anode gains of a multi-anode PMT H8500 was varied by a factor of approximately 3 among 64 anodes, we measured the light output and energy resolution of each pixel in the LaBr$_3$:Ce and GSO:Ce arrays using a 2-inch square single-anode PMT (Hamamatsu R6236) with optical grease (OKEN 6262A). Here each pixel was irradiated with gamma rays from the collimated ^{133}Ba source as described before. The R6236 was operated with high voltages of 800 and 1000 V for the LaBr$_3$:Ce and GSO:Ce arrays, respectively. Figure 6.13 shows the energy spectra of the center pixel in the LaBr$_3$:Ce and GSO:Ce arrays. Moreover, Figs. 6.14 (a) and

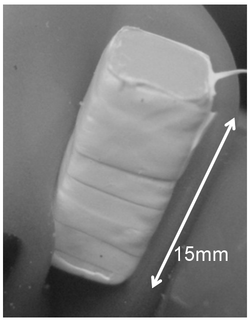

Figure 6.8: Photograph of $LaBr_3$:Ce pixel

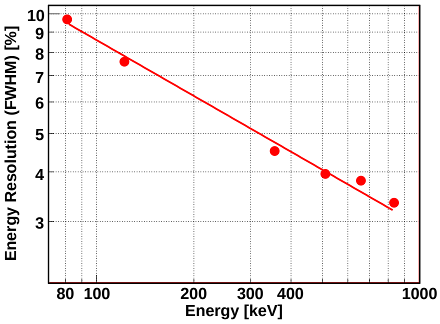

Figure 6.9: FWHM Energy resolution of $LaBr_3$:Ce pixel as a function of the energy.

(b) show light outputs normalized to each maximum pixel in the $LaBr_3$:Ce and GSO:Ce arrays, respectively. The average and SD values of the FWHM energy resolutions of all 8×8 $LaBr_3$:Ce and GSO:Ce pixels were $5.8 \pm 0.9\%$ and $11.3 \pm 0.9\%$ at 356 keV, respectively (Fig. 6.14 c, d).

This results showed that the FWHM energy resolution of $LaBr_3$:Ce was worse by approximately 1 % point, after the assembly. On the other hand, that of GSO:Ce is not changed. It suggests that the $LaBr_3$:Ce crystals might be damaged due to moisture during the assembly or glass window worsens the resolution.

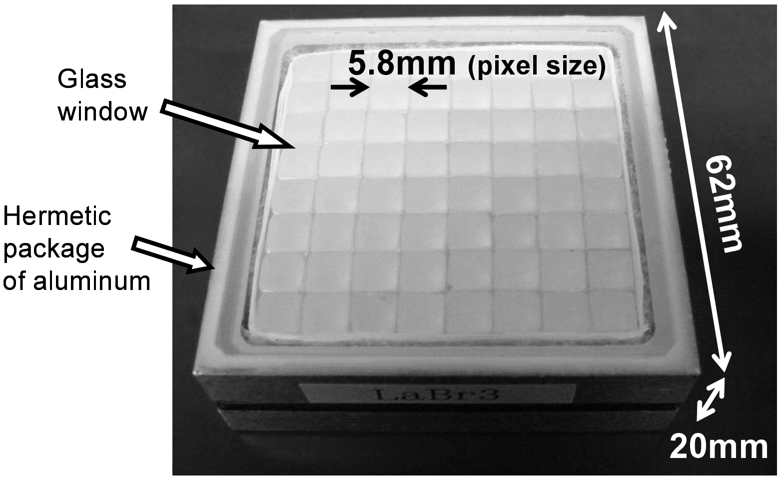

Figure 6.10: Photograph of an 8 × 8 array of LaBr$_3$:Ce pixels in a hermetic package.

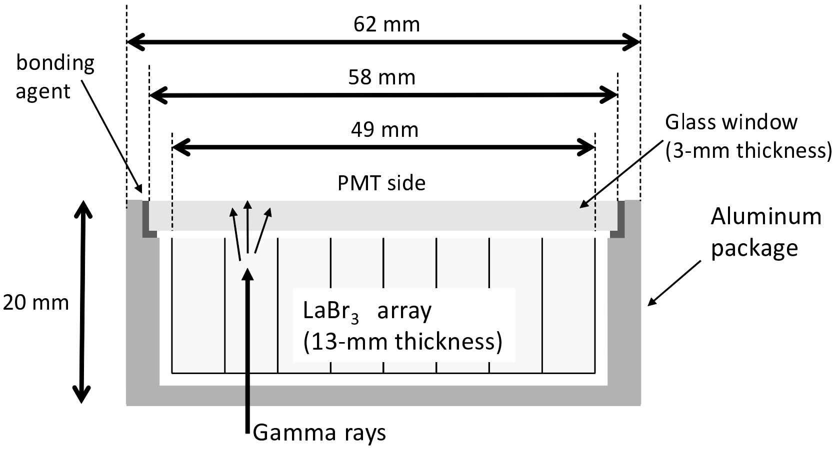

Figure 6.11: Schematic view of an 8 × 8 array of LaBr$_3$:Ce pixels.

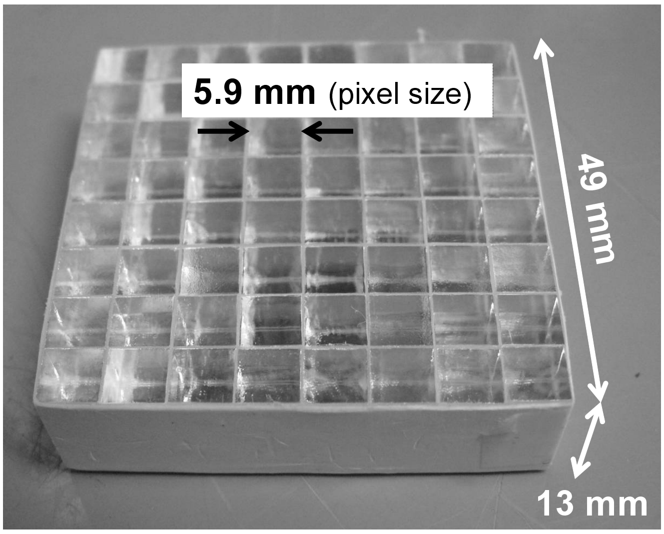

Figure 6.12: Photograph of an 8 × 8 array of GSO:Ce pixels in a hermetic package.

6.7 Performance of Array Camera

To estimate the energy resolution of $LaBr_3$:Ce array, the $LaBr_3$:Ce array was then mounted to a 64-channel multi-anode PMT H8500 with optical grease (OKEN6262A) as shown in Fig. 6.15. The H8500 had an effective area of 49 mm ×49 mm, an external size of 52 mm × 52 mm, and a 1.5-mm thick borosilicate glass window. The outer part of the quartz window of $LaBr_3$:Ce array than the PMT surface was covered with a Teflon^{TM} reflector. The PMT had a bialkali photocathode and 8 stages of metal channel dynodes for electron multiplication. The relative uniformity of the PMT anode-gain were 2.4 among 64 anodes. To reduce the number of signals, the 64-anode signals of the PMT were reduced to four channels using a resistor-chain board connecting the anodes with 100Ω chips [101]. Each output signal of the four corners was preamplified with an integrating time of 5.4 μsec, shaped in a shaping time of 0.5 μsec with a module (Hoshin Electronics Co., LTD. N016-V). This shaped signal was digitized with a peak-hold analog-to-digital converter (ADC) (Hoshin V014). The values of the four signals (a, b, c, and d) were used to calculate the both two-dimensional positions (x, y) and the light yield corresponding to the energy of an incident gamma ray (E). The detail of the calculation, called the charge-division method, is as shown in Chapter 4.

Although we have calculated the position of the hit anode without any correction of the anode gain uniformity, it was shown that all pixels in 9 GSO:Ce arrays were found to be clearly resolved in the reconstructed images [131]. We used the same PMT H8500 in the measurements

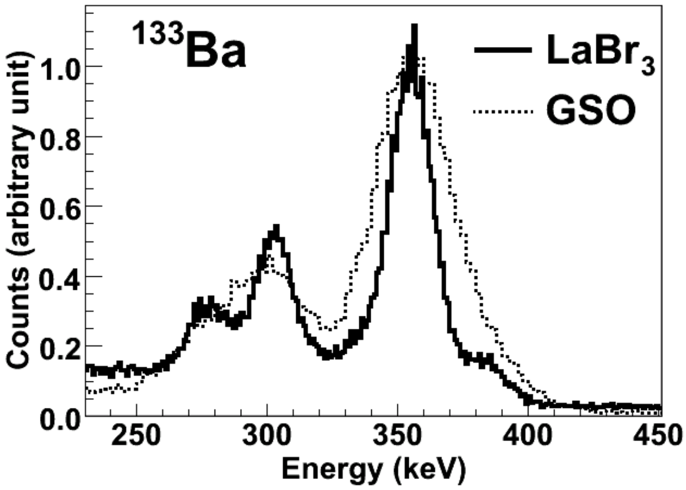

Figure 6.13: Energy spectra of the center pixel (x = 4, y = 4 in Fig. 10) in the $LaBr_3$:Ce (solid line) and GSO:Ce (dotted line) arrays coupled to a single-anode PMT (Hamamatsu R6236) and irradiated with collimated gamma rays from a ^{133}Ba source.

of the $LaBr_3$:Ce and GSO:Ce arrays. The H8500 was operated with a gain of $\sim 5 \times 10^5$ at a high voltage of ~ -800 V for the $LaBr_3$:Ce array, and with a gain of $\sim 1 \times 10^6$ at a high voltage of ~ -900 V for the GSO:Ce array. These gains were adjusted within the dynamic range of the preamplifier considering a larger light output of $LaBr_3$:Ce than that of GSO:Ce.

The arrays were irradiated with gamma rays from ^{57}Co (122 keV), ^{356}Ba (81, 356 keV), ^{22}Na (511 keV), ^{137}Cs (662 keV), and ^{54}Mn (835 keV) sources. Figs. 6.16 and 6.17 show flood-field irradiation images taken with the $LaBr_3$:Ce and GSO:Ce arrays, histograms of events with pixels in the central row of the array (image profile), and spectra from the center pixel in the array for a ^{137}Cs source. Here, we used the imaging method as mentioned in Chapter 4. The image profile was obtained using approximately 50-150 keV energy deposit events depending on the anode gain. In addition, an image profile in flood-field irradiation from a ^{57}Co source is shown for the events above approximately 25-75 keV. The peak-to-valley ratios of the image profiles of the $LaBr_3$:Ce array were 21 and 36 on the average for ^{137}Cs and ^{57}Co sources, respectively, whereas those of the GSO:Ce array were 20 and 17 using the same sources.

6.7.1 Energy Resolution

The FWHM energy resolutions at 662 keV of the $LaBr_3$:Ce and GSO:Ce arrays are also shown in Figs. 6.18 (a) and (b). There found a significant difference in the energy resolutions between

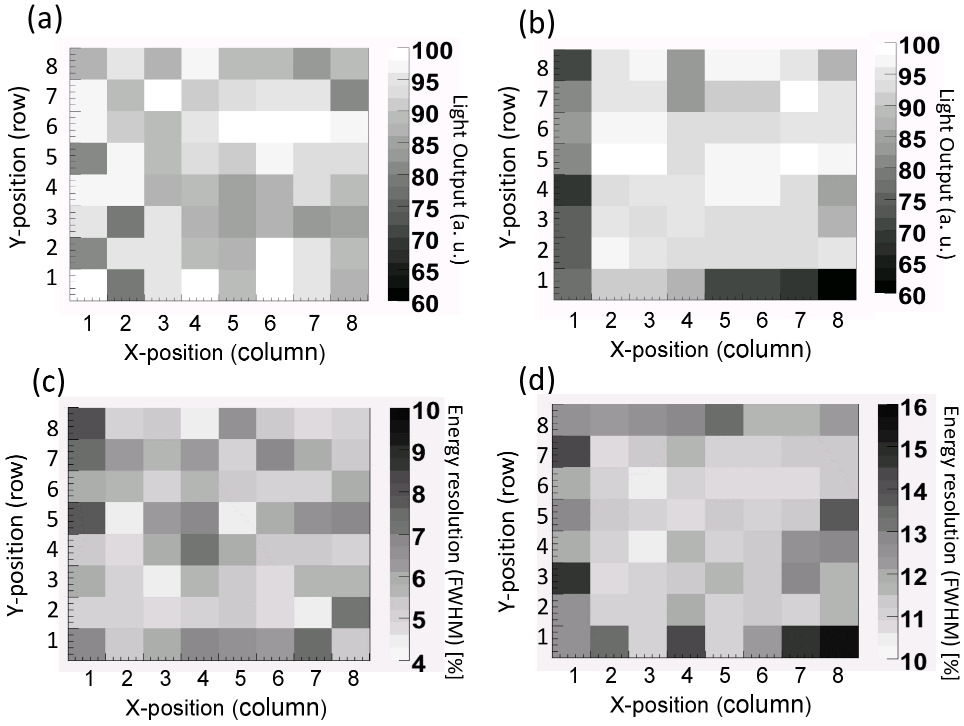

Figure 6.14: Light output of each pixel of the LaBr$_3$:Ce (a) and GSO:Ce (b) arrays (each maximum value is normalized to 100), and FWHM energy resolution at 356 keV of each pixel of the LaBr$_3$:Ce (c) and GSO:Ce (d) arrays, which were coupled to a single-anode PMT (Hamamatsu R6236).

the inner and outer pixels for the LaBr$_3$:Ce array. Fig. 6.18 (c) shows the average and SD values of the FWHM energy resolutions at several energies. The results of a fit by equation 6.1 are represented by the lines in Fig. 6.18 (c) and the resulting parameters are listed in Table 6.6. The LaBr$_3$:Ce array had a higher energy resolution than the GSO:Ce array by a factor of approximately 1.5.

There are two possible reasons why the outer 28 LaBr$_3$:Ce pixels had poorer energy resolutions than the inner ones. First, the intensity of light emitted in the outer pixels is lower than that of the inner pixels. Or second, although the outer light intensity is the same as the inner intensity, a smaller fraction of light from the outer pixels enters the PMT window.

The second reason is supported by the measurement of the array using a single-anode PMT R6236 with a larger window than the quartz window of the scintillator array, as described in section 6.5.2. This measurement shows that the energy resolutions were uniform among all 8×8 pixels. To improve the energy resolution of the outer pixels of the LaBr$_3$:Ce array, we will need to develop a new package for the LaBr$_3$:Ce array with a quartz window the same size as the PMT window (see section 6.8).

We also measured the energy resolution as an array, where sum of all 8×8 pixels were used. In addition, the sum of the inner 6×6 LaBr$_3$:Ce pixels is also measured, because the energy

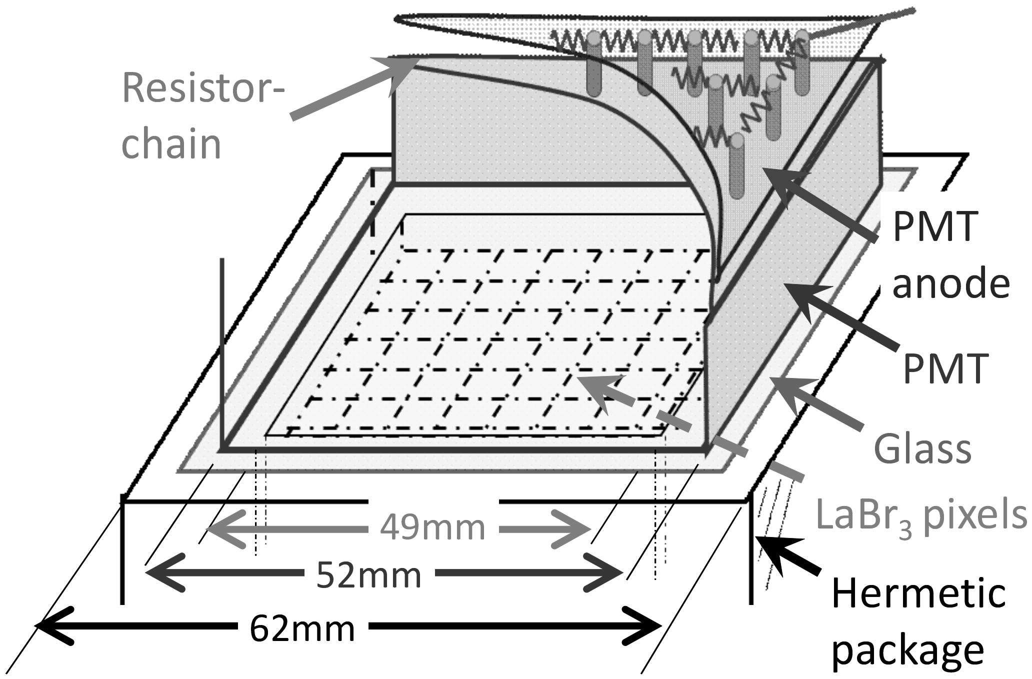

Figure 6.15: Schematic view of the LaBr$_3$:Ce scintillation camera.

resolution of the inner ones is better clearly. Fig. 6.19 (a) shows the sum of energy spectra taken with all LaBr$_3$:Ce pixels, inner 6×6 LaBr$_3$:Ce pixels, and all GSO:Ce pixels in flood-field irradiation from a ^{137}Cs source. The FWHM energy resolutions of these spectra at 662 keV are $6.4 \pm 0.2\%$ with all LaBr$_3$:Ce pixels, $5.4 \pm 0.3\%$ with inner 6×6 LaBr$_3$:Ce pixels, and $10.4 \pm 0.2\%$ with all GSO:Ce pixels. Figure 6.19 (b) shows the dependence of the resolutions on the energy. The parameters for the best-fit lines in Fig. 6.19 (b) are listed in Table 6.6.

Although the outer pixels have poorer energy resoluteness than the inner ones, the energy results of LaBr$_3$:Ce array is still better than GSO:Ce array. For the use of LaBr$_3$:Ce array in the ETCC, the FWHM ARM at 662 keV is expected to be 4.6° and 4.3° for the LaBr$_3$:Ce array

Table 6.6: Parameters of best-fit lines

	crystal		$\alpha^\star$	$\beta^\star$
Average of 64 pixels	LaBr$_3$:Ce	All pixels	7.0 ± 0.5	0.44 ± 0.01
	inner 6×6	5.8 ± 0.4	0.47 ± 0.03	
	GSO:Ce	All pixels	10.8 ± 0.3	0.48 ± 0.01
Sum of 64 pixels	LaBr$_3$:Ce	All pixels	6.5 ± 0.5	0.57 ± 0.01
	inner 6×6	5.4 ± 0.3	0.60 ± 0.01	
	GSO:Ce	All pixels	10.4 ± 0.9	0.51 ± 0.01

*:α and β are defined by equation 6.1

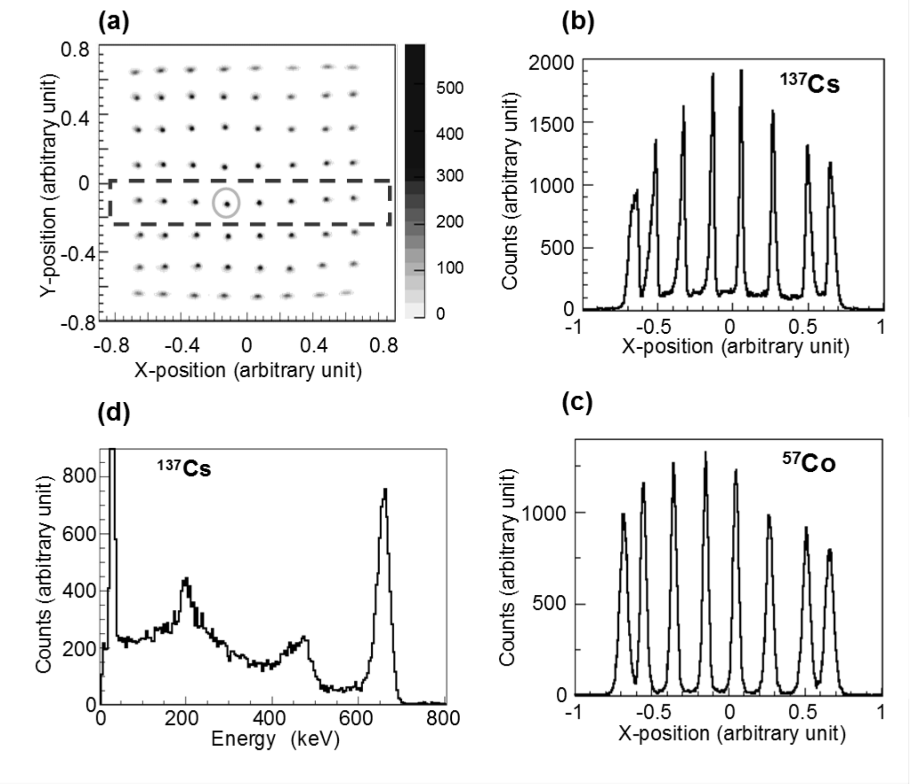

Figure 6.16: Reconstructed images and energy spectra with the $LaBr_3$:Ce array coupled to a PMT H8500. (a) 2-D image in flood-field irradiation of gamma rays from a ^{137}Cs source. Image profile with pixels in the center row of the array, indicated by the dashed square, when the array was irradiated with gamma rays from ^{137}Cs (b) and ^{57}Co (c) sources. (d) Energy spectrum of ^{137}Cs from the central pixel in the array indicated by the circle in (a).

with all pixels and the inner 6 × 6 pixels, respectively. On the other hand, ETCC using the GSO:Ce array produce the resolution of 5.3° (FWHM) at 662 keV.

6.8 Improvement of a $LaBr_3$:Ce Array

As described in the previous section, we have developed the $LaBr_3$:Ce array (hereafter first generation). However, the outer pixels in the first generation has lower energy resolution than inner. In order to improve energy resolution of the outer pixels, we have developed a second-generation $LaBr_3$:Ce array with a compact hermetic package. Here, we changed the design of the hermetic package as shown in table 6.7. We developed two second generation arrays.

As materials of the two arrays, we also used four monolithic $LaBr_3$ BrilLanCe 380^{TM} [159] crystals (hereafter I describe #3 - #6) with a size of ϕ38 mm ×38 mm as the same as the first generation. We measured the energy resolutions and the light-output uniformities of #3 to #6

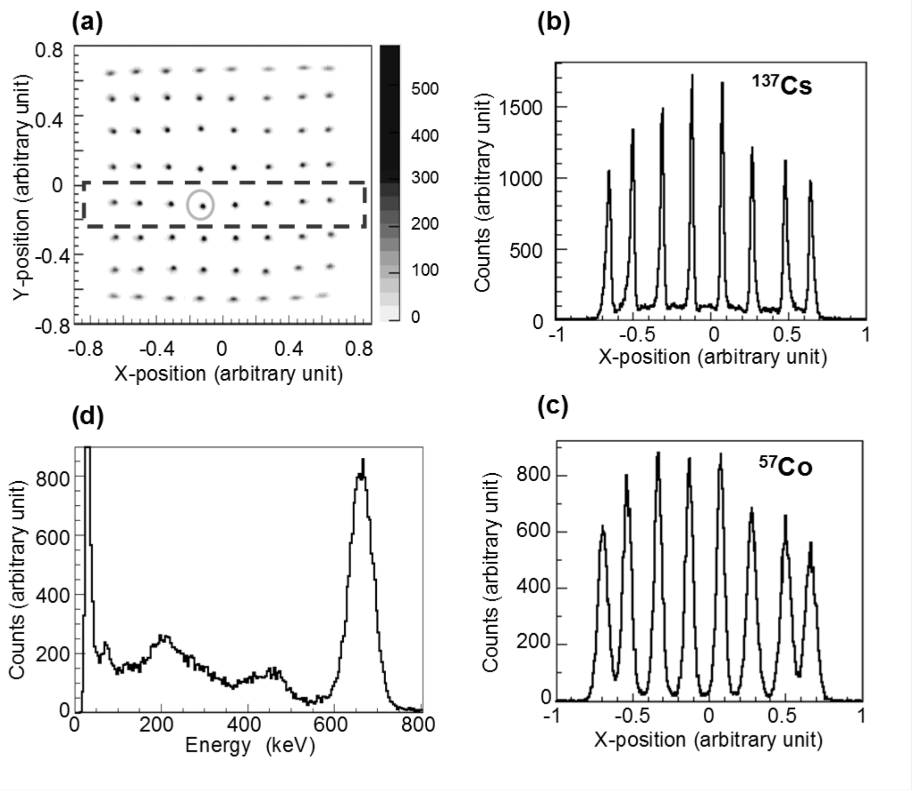

Figure 6.17: Images and energy spectra with the GSO:Ce array coupled to the PMT H8500. Captions are the same as in Fig. 6.16.

using the same method when we measured the #1 and #2. The parameters of the best-fit lines for the FWHM energy resolution of #1 to #6 as a function of the energy are listed in Table 6.8. Additionally, the uniformities of the light output and the energy resolution are listed in table 6.9. The light-output uniformity of #3 was worse than the others. However, this uniformity is enough to assemble the array, because this uniformity is better than the light-output uniformity of the LaBr$_3$:Ce array measured by single anode PMT as described in section 6.6. Therefore, both #3 and #6 were used as an appropriate material for the new array.

Thus we have developed two arrays (hereafter array A and B). The array A and B were made from #3, #4 and #5, #6, respectively. Figure 6.20 shows the second generation LaBr$_3$:Ce array

Table 6.7: Parameters of the structures in the LaBr$_3$:Ce array

generation	whole volume	glass volume
1st.	62 mm ×62 mm ×20 mm	58 mm ×58 mm ×3.0mm
2nd.	54 mm ×54 mm ×19 mm	52 mm ×52 mm ×2.3mm

Table 6.8: Parameters of best fit for the monolithic $LaBr_3$:Ce crystals

crystal	$\alpha^\star$	$\beta^\star$
#1	3.10 ± 0.03	0.545 ± 0.002
#2	3.06 ± 0.03	0.543 ± 0.002
#3	3.25 ± 0.05	0.501 ± 0.002
#4	3.08 ± 0.05	0.504 ± 0.002
#5	3.11 ± 0.06	0.511 ± 0.003
#6	3.17 ± 0.05	0.499 ± 0.002

$\star$:α and β are defined by equation 6.1

Table 6.9: Uniformity of the monolithic $LaBr_3$:Ce

		mean ± SD
Light output at 356 keV	#1	1.003 ± 0.005
	#2	1.006 ± 0.005
	#3	0.99 ± 0.02
	#4	0.999 ± 0.002
	#5	1.001 ± 0.002
	#6	1.000 ± 0.003
FWHM Energy resolution at 356 keV	#1	4.10 ± 0.07
	#2	4.08 ± 0.07
	#3	4.18 ± 0.04
	#4	4.06 ± 0.06
	#5	4.10 ± 0.05
	#6	4.14 ± 0.06

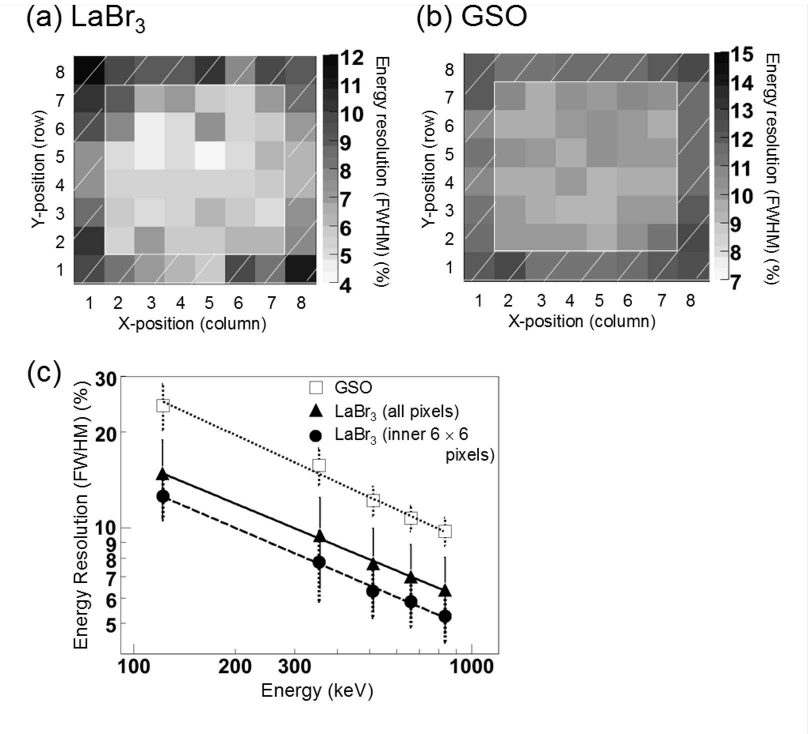

Figure 6.18: Energy resolution of each pixel of the LaBr$_3$:Ce (a) and GSO:Ce (b) arrays at 662 keV using the H8500. (c) Averages and SDs of energy resolutions of the pixels as a function of energy. Solid line denotes the best fit to the LaBr$_3$:Ce array data with all 64 pixels (triangles). Broken line denotes that of the LaBr$_3$:Ce array with inner 6×6 pixels (circles) represented by the non-shaded portion in (a). Dotted line denotes that of the GSO:Ce array (open squares). Error bars represent SDs.

compared with the first generation.

We measured the second generation arrays using as doing the first generation, and we obtained the images and energy spectra (Fig. 6.21). Figure 6.22 shows FWHM energy resolutions of each pixels for array A and B. Fig. 6.23 shows the FWHM energy resolutions of the average and SD of all 64 LaBr$_3$:Ce pixels (array A) as a function of the energy. For comparison, those of a GSO:Ce array and fist generation are also shown in Fig. 6.23. The best-fit lines for the data points listed in table 6.10 including array B, and the point of inner 6×6 pixles for only LaBr$_3$:Ce arrays of the both first and second generations.

The results show that the differences of the energy resolution between the outer and inner pixels was considerably improved in the second-generation array. This difference is similar level to that of GSO:Ce array. The difference in GSO:Ce array and second generation is thought that light emitted from the pixels on the corner and edge of the array spreads over a few anodes of the PMT.

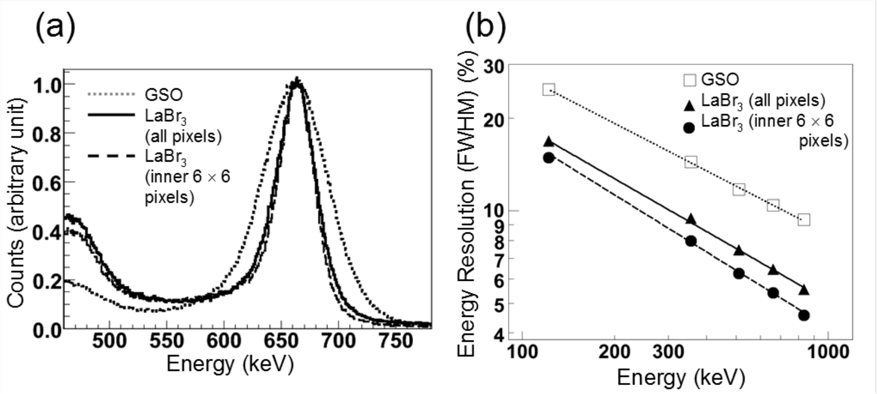

Figure 6.19: (a) Energy spectra taken with all GSO:Ce pixels (dotted line), all LaBr$_3$:Ce pixels (solid line), and inner 6 × 6 LaBr$_3$:Ce pixels (broken line), which were coupled to the PMT H8500 and irradiated with gamma rays from a ^{137}Cs source. (b) Energy resolutions and best-fit lines with all GSO:Ce pixels (open squares and dotted line), all LaBr$_3$:Ce pixels (triangles and solid line), and inner6 × 6LaBr$_3$:Ce pixels (circles and broken line) as a function of energy.

Although the array B of the second generation did not have a good energy resolution than the array A, it is still better than GSO:Ce array. Thus, we succeeded in the development of the array to use for the absorber in the ETCC.

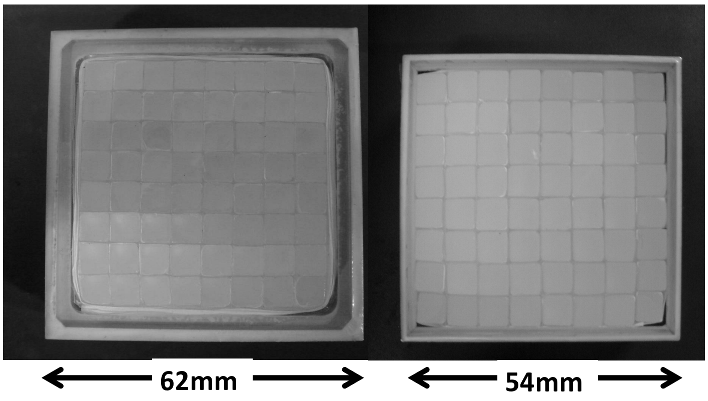

Figure 6.20: Comparison of LaBr$_3$:Ce array between (a) first and (b) second generation (array A).

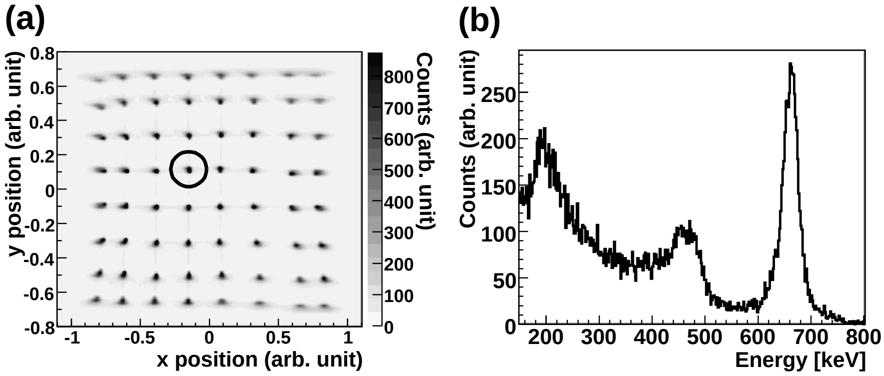

Figure 6.21: (a) Two-dimensional image of the LaBr$_3$:Ce array A in flood-field irradiation of gamma rays from a ^{137}Cs source. (b) Energy spectrum of ^{137}Cs with the central pixel indicated by the circle in the left image.

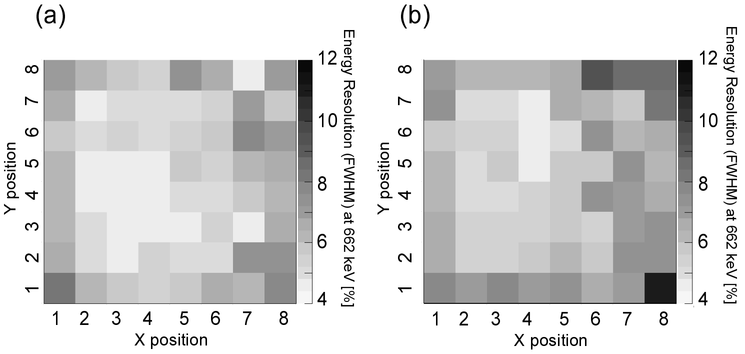

Figure 6.22: Map of the FWHM energy resolution of each LaBr$_3$:Ce pixel at 662 keV. (a) and (b) are first and second generation, respectively.

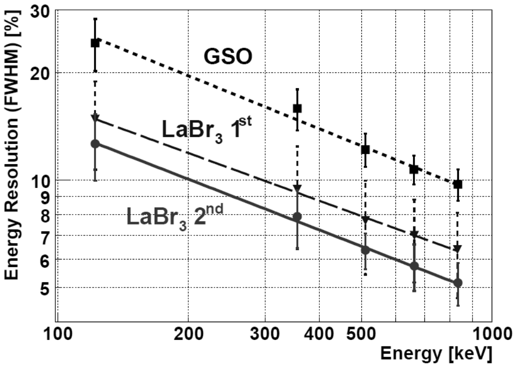

Figure 6.23: FWHM energy resolution of the average and SD of all 64 LaBr$_3$:Ce (2nd generation array A, circles) as a function of energy, and that of GSO:Ce (squares) and 1st generation (triangle).

Table 6.10: FWHM energy resolution of LaBr$_3$:Ce arrays

generation		$\alpha^\star$	$\beta^\star$
1st	all pixels	7.0 ± 0.5	0.47 ± 0.03
	inner 6 × 6	5.8 ± 0.4	0.44 ± 0.01
2nd arrayA	all pixels	5.7 ± 0.5	0.47 ± 0.01
	inner 6 × 6	5.4 ± 0.3	0.44 ± 0.01
2nd arrayB	all pixels	6.4 ± 0.6	0.61 ± 0.02
	inner 6 × 6	5.8 ± 0.7	0.58 ± 0.02
GSO:Ce	All pixels	10.8 ± 0.3	0.48 ± 0.01
	inner 6 × 6	10.0 ± 0.2	0.46 ± 0.03

$\star$:α and β are defined by equation 6.1

6.9 Comparison with Other Position-Sensitive LaBr$_3$:Ce Camera

We adopted the array type scintillation camera because the spatial resolution was dictated by the pixel width and the uniformity over the entire area, which do not need position calibration in space even after the deterioration of the scintillator by cosmic rays irradiation. In addition, some multiple hit events occur in the scintillator, and, for the Compton camera, we need to measure the first hit point of a gamma ray in the scintillator. Although it is difficult to discriminate between multiple Compton hits and a single hit in the continuous crystal, it is feasible with an array camera to judge first hit point. Indeed, events with multiple hits are not negligible for gamma rays above a few hundred keV up to MeV where the main interaction process is Compton scattering. For example, for 662 keV gamma rays vertically incident on the scintillator, GEANT4 simulation show that probability of the multiple hits in our LaBr$_3$:Ce array is only 7.5% of all events between the pixels.

For the continuous type, spatial resolution (FWHM) is defined as a half width of image profile when the crystal is irradiated with collimated gamma rays. On the other hand, the FWHM resolution of array camera $\triangle x$ is defined as $\triangle x = 2.35 \times \frac{d}{\sqrt{12}}$, where d is pixel pitch. Here our array camera has the resolution of 4.1 mm. The spatial resolution of continuous type is several times better than that of the array, and it is effective if it is important to obtain the spatial resolution. However, table 6.1 shows that it is enough with an FWHM spatial resolution of array camera (4.1 mm) for Compton camera.

Next, I describe the detail of comparison between the array and continuous type. Kuhn et al. have developed Anger-logic detectors with LaBr$_3$:Ce pixellated arrays that achieved an FWHM energy resolution of $\sim 5.3\%$ at 511 keV [154]. On the other hand, that of our detector was 6.3% at 511 keV using all 8×8 LaBr$_3$:Ce pixels in array A (second generation). Kuhn et al. obtained a better energy resolution because they used single-anode PMTs. However, the peak-to-valley ratio of their detectors was approximately 3 above 450 keV, whereas that of our array was more than 20 from approximately 100 to 900 keV.

Bloser et al. measured a continuous LaBr$_3$:Ce with a volume of 5 cm ×5 cm ×1 cm using a 3" square position-sensitive PMT (Hamamatsu R2487), irradiated with collimated gamma rays [153]. This crystal had an FWHM spatial resolution of ~ 3 mm and ~ 6 mm at 122 keV, and an FWHM energy resolution of 13.5% and $\sim 18\%$ at 122 keV near the center and at a diagonal distance of ~ 28 mm from the center, respectively. On the other hand, Pani et al. also reported that a LaBr$_3$:Ce detector, consisting of a continuous LaBr$_3$:Ce crystal with an area of 5 cm ×5 cm, a thickness of 1 cm, and a PMT (H8500), had a spatial resolution of 1.80 mm at 122 keV in an effective area of 36 mm ×36 mm [15]. Their spatial resolutions were better than Bloser et al. Because our array had a spatial resolution of 4.1 mm (FWHM) over the entire area of the array, the continuous LaBr$_3$:Ce detector had a better spatial resolution than our array in the center region. However, the continuous LaBr$_3$:Ce detector had a poorer spatial resolution of up to 6 mm outside the effective area, whereas ours remained 4.1 mm even near the edges. The continuous $LaBr_3$:Ce detector of Pani et al. also had better energy resolutions than Bloser et al., ~ 12 and $\sim 15\%$ (FWHM) at 122 keV inside and outside the effective area, respectively, whereas our array had $12.6 \pm 2.0\%$ and $17.7 \pm 4.3\%$ (FWHM) at 122 keV with inner 6×6 and outer 28 $LaBr_3$:Ce pixels, respectively. Because the effective area of the continuous $LaBr_3$:Ce detector was the same as the area of the inner 6×6 pixels in our $LaBr_3$:Ce array, there is no difference in the energy resolutions over the inner region of approximately 3.6 cm ×3.6 cm between the continuous $LaBr_3$:Ce detector and our array, whereas the outer pixels in our array have poorer energy resolutions near the edge than the continuous $LaBr_3$:Ce.

Case et al. [157] and Budden et al. [158] showed position-sensitive detectors using continuous $LaBr_3$:Ce crystals and wavelength-shifting fibers. Case et al. reported that a continuous $LaBr_3$:Ce crystal with a 2.5-cm ϕ and a thickness of 2.5 cm had an FWHM energy resolution of 5.6% at 662 keV using a single-anode PMT viewing through a layer of 2-mm ϕ wavelength-shifting fibers (Saint-Gobain BCF-99-33A). This energy resolution is similarly to the inner 6×6 pixels in our $LaBr_3$:Ce array. On the other hand, Budden et al. measured the position resolution in an array of four continuous $LaBr_3$:Ce crystals each with a size of 3.8 cm ×3.8 cm ×1 cm glued together into a 7.6 cm ×7.6 cm ×1 cm mosaic. The position measurement was achieved using a layer of wavelength-shifting fibers arranged parallel to the surface of the crystal and coupled to a multi-anode PMT. Two orthogonal layers were used to measure a two-dimensional position. The position resolution was 2.7 mm (1σ, FWHM: 6.3 mm) irradiated by gamma rays from a ^{137}Cs source, and it is the worse resolution than our array.

6.10 Performance of the Compton Camera with a $LaBr_3$ Array

Using first and second generation of $LaBr_3$:Ce arrays, we measured the angular resolution of the ETCC. Figure 6.24 shows the set up for the performance test of the ETCC consisting of first and second-generation $LaBr_3$:Ce arrays. Here we also used a 10×10 array with a pixel size of 4 mm ×4 mm ×30 mm made by Saint-Gobain [154]. The FWHM energy resolutions were $5.2 \pm 0.7\%$ at 662 keV using the same multi-anode PMT as described in the previous chapter. However, this array had several bad pixels which is hard to separate between pixels in the flood-field irradiation image (Fig. 6.25), and these pixels were not used for the analysis of the ETCC data.

Although we used a similar small ETCC of proton beam experiment,the drift height in the TPC was different from the ETCC of proton beam as followings. TPC had an detection area of 10 cm×10 cm ×7.5 cm, and a drift voltage of −3300 V was supplied to the drift plane. The μ-PIC was driven at 490 V with a gain of approximately 3500, and the total gas gain of the TPC was $\sim 3.5 \times 10^4$. The FWHM energy resolution of the TPC at 22.2 keV (^{109}Cd) was $27.7 \pm 0.6\%$. The ETCC was irradiated with gamma rays from ^{137}Cs, and ^{54}Mn point sources at 20 cm from the center of the μ-PIC (Fig. 6.24). In addition, an ^{131}I (364 keV) liquid source, which was a

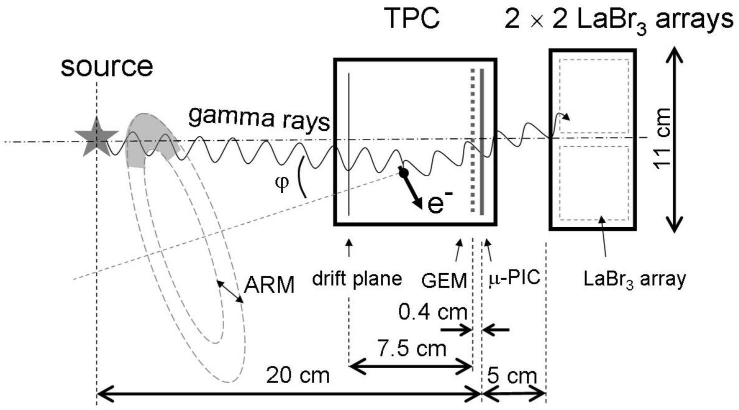

Figure 6.24: Schematic view of the setup of the ETCC and $Labr_3$:Ce arrays including second-generation arrays

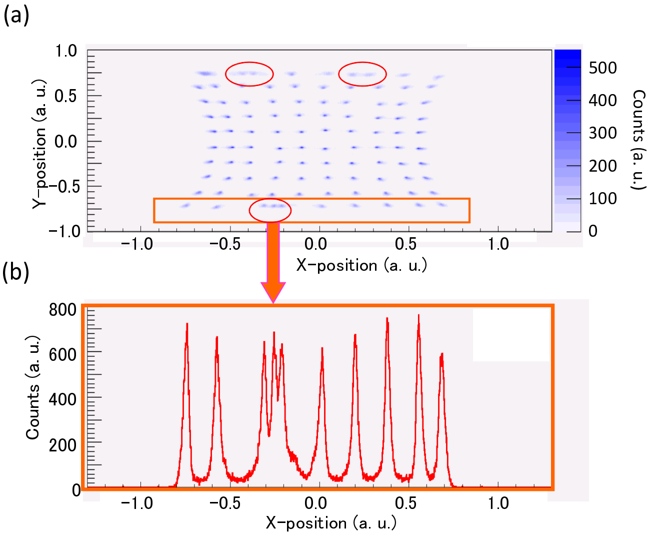

Figure 6.25: Bad pixels in Saint-Gobain $Labr_3$:Ce arrays. (a)flood-field irradiation image and (b) histograms of events with pixels in the square as shown (a).

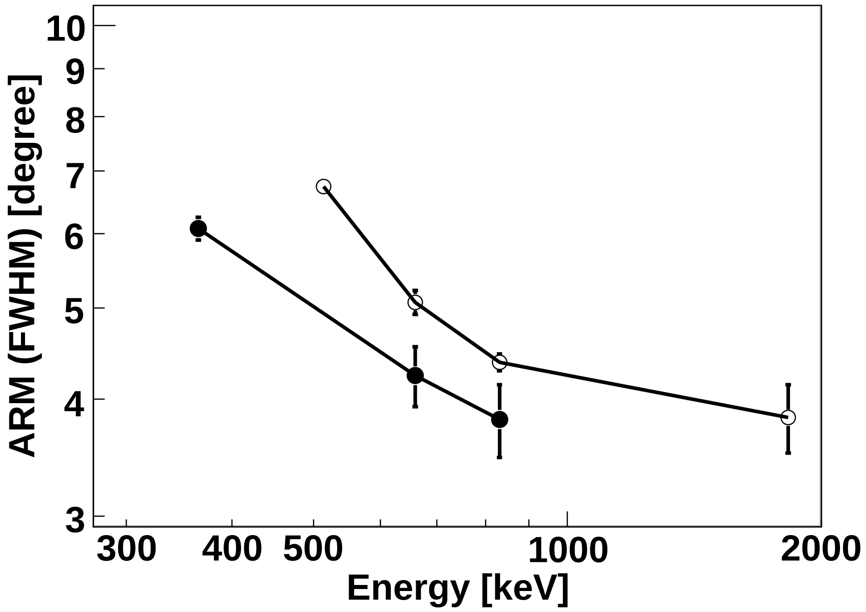

Figure 6.26: ARM of ETCC with a LaBr$_3$:Ce array (solid circles) and GSO:Ce arrays used for RCNP (open circles) as a function of the energy.

drop with a size of less than ϕ3mm, was also used.

The FWHM ARM of the ETCC with LaBr$_3$:Ce arrays was $4.2 \pm 0.3°$ at 662 keV as shown in Fig 6.26.

For the comparison, Fig. 6.26 also shows the FWHM ARM of the ETCC with 26-mm thick GSO:Ce arrays which was used for the RCNP beam test. The FWHM energy resolution of the GSO:Ce array was $12.7 \pm 3.4\%$ at 662 keV, and that of the TPC for RCNP beam test was $30.0 \pm 0.9\%$ at 22.2 keV (chapter 5). The FWHM ARM at 662 keV was $5.1 \pm 0.2°$. We succeeded in improvement of angular resolution of the ETCC using the LaBr$_3$:Ce array.

Here, the contributions to the ARM were itemized as followings:

- Energy resolution of scintillator ($\sigma_{s,e}$)
- Energy resolution of TPC ($\sigma_{t,e}$)
- Position resolution of scintillator ($\sigma_{s,p}$)
- Position resolution of TPC ($\sigma_{t,p}$)
- Doppler broadening (σ_d)
- Other, unknown factor (σ_o)

Table 6.11 summarized the above factors for this experiment using the calculation as described in section 6.3.

Here, $\sigma_{s,e}$ and $\sigma_{s,e}$ were assumed that the energy resolution of the TPC or scintillator had no error, respectively, and σ_e was calculated with the both energy resolutions. σ_e was not described

Table 6.11: Contribution to ARM (FWHM) at 662 keV [deg.]

	$\sigma_{s,e}$	$\sigma_{t,e}$	σ_e^a	$\sigma_{s,p}$	$\sigma_{s,p}$	σ_p^b	σ_d
w/ GSO:Ce array	4.0	1.1	4.5	2.8	0.3	2.8	0.9
w/ LaBr$_3$:Ce array	2.0	0.9	2.7	3.3	0.3	3.3	0.9

a: $\sigma_e = f(\sigma_{s,e}, \sigma_{t,e})$, b: $\sigma_p^2 = \sigma_{s,p}^2 + \sigma_{t,p}^2$

Table 6.12: Contribution to ARM (FWHM) at 662 keV [deg.]

	ARM	σ_{tot}	σ_e	σ_p	σ_d
	(measurement)	(calculation)			
w/ GSO:Ce array	5.1 ± 0.2	5.3	4.5	2.8	0.9
w/ LaBr$_3$:Ce array	4.2 ± 0.3	4.3	2.7	3.2	0.9

as $\sigma_e = \sigma_{s,e}^2 + \sigma_{t,e}^2$, because the energy of scattered gamma ray and Compton recoil electron are not independence and the sum of these energy is the incident gamma-ray energy. Since the Compton recoil-electron energy is commonly smaller than scattered gamma-ray energy by an order of 1, the contribution of the recoil-electron energy resolution to the ARM is small than that of scattered gamma-ray energy resolution.

σ_p was calculated assuming the position resolutions of the TPC and scintillator. σ_p was described as $\sigma_p = \sigma_{s,p}^2 + \sigma_{t,p}^2$, because $\sigma_{s,p}$ and $\sigma_{t,p}$ are independent factor. Here, the position resolution of the TPC was assumed to be 0.4 mm (1 σ) [161], while the volume of the pixel scintillator was large than the TPC position resolution by an order of more than 1. Thus the position resolution of scintillator dominated the contribution of position resolution to the ARM σ_p.

The measured resolution σ_{tot} is described as

$$\sigma_{tot}^2 = \sigma_e^2 + \sigma_p^2 + \sigma_d^2 + \sigma_o^2. \tag{6.2}$$

where σ_e, σ_p, σ_d, and σ_o are independent factor each other. Table 6.12 lists the measurement and calculation of ARMs, where $\sigma_o = 0$.

The measurement of ARM was consistent with σ_{tot}, and σ_os were negligible for the ETCC with GSO:Ce and LaBr$_3$:Ce arrays.

Using the ETCC with LaBr$_3$:Ce arrays, the spatial resolution of the ETCC is expected to be 1.8 and 1.1 cm when the center of 15-cm-high TPC and the target have a distance of 25 and 15 cm, respectively, at 662 keV. This performance satisfies the medical requirement.

6.11 Possibility of Improvement in Angular Resolution

In the previous section, Table 6.12 suggests that the item of the position resolution is larger than that of the energy resolution if LaBr$_3$:Ce arrays are used in the ETCC. Thus, improvement of the position resolution is effective in order to obtain a better ARM. Especially, the improvement

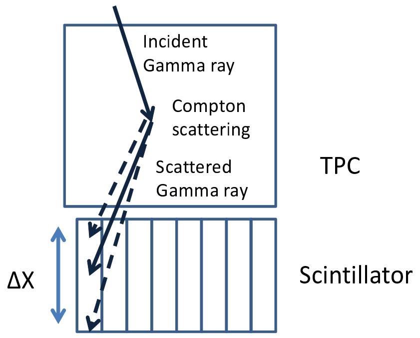

Figure 6.27: Schematic view of the ETCC. The scattered gamma ray is measured with some position error depending on the thickness of the pixel scintillator.

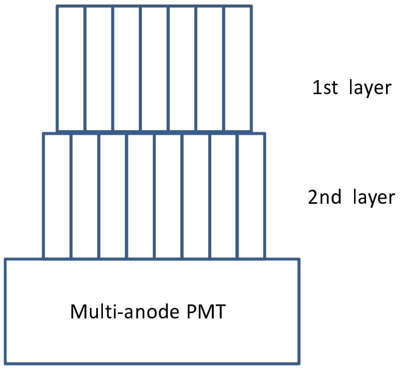

Figure 6.28: Schematic view of the 2-layer pixel array camera.

of the position resolution is limited by the thickness of the pixel scintillator as shown in Fig. 6.27. One of the solution is use of a larger size TPC than 10-cm scale TPC, because the size of the pixel scintillator become smaller relatively than that of the TPC. However, use of a larger TPC lead to be bad spacial resolution, and it is not advantage to medical imaging.

For medical imaging, the determination of the depth of interaction (DOI) in the scintillator is effective to improve the position resolution of the scintillator and the ARM of the ETCC. Although there are some methods of DOI, 2-layer $LaBr_3$:Ce pixel array (Fig. 6.28) may be applied to the ETCC because they are easy to keep the energy resolution. Other methods would lead to worsen the energy resolution, because other scintillator, which has worse energy resolution than $LaBr_3$:Ce, is used. When the depth-spatial resolution is $\sim$ 6 mm in each pixel scintillator, it is expected to be an angular resolution of $\sim 3.5^\circ$ (FWHM) at 662 keV calculated using the method as described in section 6.3.

Chapter 7

Conclusion

We have developed an Electron Tracking Compton Camera (ETCC) consisting of a gaseous time projection chamber and a position-sensitive scintillation camera as an absorber. This camera is expected to be applied to various fields such as MeV gamma-ray astronomy and medical imaging. We have already succeeded in imaging the cosmic and atmospheric gamma rays using our small size camera μ-PIC onboard a balloon in 2006. Then we have developed a larger camera with a size of 30 cm $\times$30 cm $\times$30 cm in order to detect the bright objects such as Cyg X-1. We have also tested for medical imaging using small animals with radio isotopes.

In this thesis, my works were the following two developments: (i) a continuum gamma-ray imaging detector for proton therapy, which was also important for astronomy and (ii) a novel position-sensitive scintillation camera with a better energy resolution than the GSO:Ce array camera.

As described in section 5.1, measurement of the prompt gamma rays is important in the proton therapy, because the distribution of the prompt gamma rays is correlated with the proton dose, especially near the end of the proton range. Although a scintillation detector with a collimator scanned the distribution of prompt gamma rays from a water phantom irradiated with a proton beam, no imaging detector was available for the real time monitor due to the gamma-ray backgrounds. Since the ETCC has the background rejection ability and the wide energy range, it is expected to verify the proton dose even during the proton irradiation using the continuum gamma rays.

We constructed an ETCC for the monitor in proton therapy. As a first step, our aim was to show the difference of distribution between the annihilation and prompt gamma rays, and to verify that the prompt gamma ray distribution is useful for the detection of Bragg peak position. Since higher energy gamma rays were reported to trace the proton dose, an ETCC was tuned with an energy range of 0.4 to 2 MeV. Obtained energy resolution was 15.3 ± 0.5 % at 662 keV (FWHM), and ARM and SPD were $(5.1\pm0.2)^\circ$ and $(119\pm2)^\circ$ at 662 keV (FWHM), respectively.

Using this ETCC, we tested the gamma-ray imaging from a water phantom irradiated with 140-MeV proton beam in the Research Center for Nuclear Physics (RCNP) of Osaka University in 2010. The beam current was $\sim$ 2 pA, and measurement duration was 32 hours (live time), and dead time due to the data acquisition was 6 %. Finally, we succeeded in obtaining the difference images between 463 - 559 keV and 0.8 - 2.0 MeV bands which include mainly annihilation and prompt gamma rays, respectively. The annihilation gamma-ray distribution had a flat distribution (peak width: ~ 4 cm), while prompt gamma rays (0.8 - 2.0 MeV continuum gamma rays) had sharp peak at $\sim$ 1cm-upstream of proton beam from the Bragg peak. Those results near the peak of the gamma-ray distribution were consistent with the prediction using GEANT4. This experiment may be first one to carry out the imaging for continuum gamma rays using a Compton camera in the laboratory. In addition, this results obviously indicated the ability of the ETTC for observation of continuum gamma rays in space.

However, in order to verify the proton dose more clearly, the ETCC should measure the higher energy gamma rays ($\geq$ a few MeV) with a sufficient detection efficiency. Thus we develop an ETCC with a higher detection efficiency. For example, we test new gas with an high pressure for the TPC such as 1.4-atm CF_4 based gas.

In addition, the angular resolution of the ETCC at 662 keV was not sufficient for medical imaging and astronomy. Actually, an FWHM spatial resolution was 2.2 cm at 662 keV in the beam experiment, and medical requirement is $\sim$ 1 cm. Here, use of the scintillator with a higher energy resolution is effective to for the improvement of angular (spatial) resolution of the ETCC. Therefore, we have developed a position-sensitive scintillation camera using a $LaBr_3$:Ce crystal instead of a GSO:Ce, because the $LaBr_3$:Ce has an excellent energy resolution. The monolithic $LaBr_3$:Ce had an energy resolution of $\sim$ 3 % at 662 keV (FWHM) with a single-anode Photomultiplier Tube (PMT).

Although this crystal has a hygroscopic nature, we developed an 8×8 $LaBr_3$:Ce pixels array with a pixel size of 5.8 mm $\times$5.8 mm $\times$15.0 mm using our own technique. Finally, we have developed three arrays. Then FWHM energy resolution of all 64 $LaBr_3$:Ce pixels reached 5.7 ± 0.5 % at 662 keV when coupled to a multi-anode PMT (Hamamatsu H8500), while that of a GSO:Ce array was 10.8 ± 0.3 % at 662 keV. Therefore, we succeeded in development of the novel position-sensitive scintillation camera with a better energy resolution than the GSO:Ce array.

As a results, the ETCC with the $LaBr_3$:Ce arrays had an FWHM angular resolution of $4.2 \pm 0.3^\circ$ at 662 keV, and we succeeded in improvement of the angular resolutions. Thus, the spatial resolution of the ETCC is expected to be 1.8 and 1.1 cm at 662 keV (FWHM) when the center of 15-cm-high TPC and the target have a distance of 25 and 15 cm, respectively. Since the medical requirement of the spatial resolution is $\sim$ 1 cm, our detector have an ability to use for the monitor of dose in proton therapy. In astronomy, the ETCC is expected to have a better angular resolution of $\sim 3.5^\circ$ (FWHM) at 1.27 MeV than COMPTEL which had an FWHM ARM of 4.74° at 1.27 MeV [112].

reference

[1] V. Schönfelder; *Astron. Nachr.*, **323** (2002), 524.

[2] G. K. von Schulthess; "Molecular anatomic imaging" (2006).

[3] V. Schönfelder; *New Astronomy Reviews*, **48** (2004), 193.

[4] V. Schönfelder; *A & AS* **143** (2000), 45.

[5] R. C. Hartman *et al.*; *ApJS*, **123** (1999), 79.

[6] W. N. Johnson *et al.*; *ApJS*, **86** (2001), 693.

[7] A. M. Levine *et al.*; *ApJ*, **469** (1996), 33.

[8] F. Tokanai *et al.*; *Proc. SPIE*, **2808** (1996), 563.

[9] R. Jager *et al.*; *A & A Supp.*, **125** (1997), 557.

[10] S. D. Barthelmy *et al.*;*Space Science Reviews*, **120** (2005), 143.

[11] C. Winkler *et al.*; *A & A*, **411** (2003), 1.

[12] D. E. Kuhl and R. Q. Edwards; *Radiology*, **80** (1963), 653.

[13] R. J. Jaszczak; *Phys. Med. Biol.*, **51** (2006), 99.

[14] M. M. Ter-Pogossian *et al.*; *Radiology*, **114** (1975), 89.

[15] M. E. Phelps *et al.*; *J. of Nucl. Med.*, **16** (1975), 210.

[16] G. W. Bennett; *Science* **200** (1978), 1151.

[17] R. R. Wilson; *Radiology*, **47** (1946), 487.

[18] G. T. Y. Chen *et al.*; *Int. J. Radiat. Oncol. Biol. Phys.*, **5** (1979), 1809.

[19] B. Schaffner, and E. Pedroni; *Phys Med Biol.*, **43** (1998), 1579.

[20] K. Parodi and T. Bortfeld; Phys. *Med. Biol.* **51** (2006), 1991.

[21] T. Nishio *et al.*; *Med. Phys.*, **33** (2006), 4190.

[22] C. Min *et al.*; *Applied Phys. Lett.*, **89** (2006), 183517.

[23] J. Ködlseder; *Proc. SPIE*, **6266** (2006), 623.

[24] R. Orito *et al.*; *Nucl. Instr. and Meth. A*, **513** (2003), 408.

[25] T. Tanimori *et al.*; *New Astron. Rev.*, **48** (2004), 263.

[26] A. Takeda *et al.*; *IEEE Trans. Nucl. Sci.*, **51** (2004), 2140.

[27] A. Takada *et al.*; *Nucl. Instr. and Meth. A*, **546** (2005), 258.

[28] H. Kubo *et al.*;*Nucl. Instr. and Meth. A*, **513** (2003), 94.

[29] K. Miuchi *et al.*; *IEEE Trans. Nucl. Sci.*, **50** (2003), 825.

[30] K. Ueno *et al.*;*Nuc.r Sci. Symp. Conf. Rec., 2008. NSS '08. IEEE*,(2008), 3470.

[31] F. Sauli; *Nucl. Instr. and Meth. A*, **386** (1997), 531.

[32] M. Inuzuka *et al.*; *Nucl. Instr. and Meth. A*, **525** (2004), 529.

[33] A. Ochi *et al.*;*Nucl. Instr. and Meth. A*, **471** (2003), 264.

[34] T. Nagayoshi *et al.*; *Nucl. Instr. and Meth. A*, **525** (2003), 20.

[35] H. Kubo *et al.*; *Nucl. Sci. Symp. Conf. Rec.*, **1** (2006), 406.

[36] A. Takada *et al.*; *J. Phys. Soc. Jpn.*, **78** (2009), 161.

[37] S. Kabuki *et al.*; *Nucl. Instr. and Meth. A*, **580** (2007), 1031.

[38] S. Kabuki *et al.*;*Nucl. Sci. Symp. Conf. Rec., 2008. NSS '08. IEEE*, (2008), 3937.

[39] XCOM; Photon Cross Section Database (http://physics.nist.gov/PhysRefData/Xcom/Text/XCOM.html).

[40] G. F. Knoll; "Radiation Detection and Measurement 3rd edition", *WILEY* (2001).

[41] V. Schönfelder; "The Universe in Gamma Rays", *Springer* (2001).

[42] V. Schönfelder *et al.*; *ApJS*, **86** (1993), 657.

[43] K. S. Cheng, and G. E. Romero; "Cosmic Gamma-Ray Sources", *Kluwer Academic publishers* (2004).

[44] P. V. Ballmoos; *Experimental Astronomy*, **6** (1995), 85.

[45] B. Kozlovsky *et al.*; *ApJS*, **141** (2002), 523.

[46] S. Hayakawa, Prog. Theo. Phys. **8** (1952), 571.

[47] P. Morrison, Nuovo Cimento **7** (1958), 858.

[48] W. Kraushaar *et al.*ApJ **177** (1972), 341.

[49] G. Badhwar *et al.*; Astrophysics and Space Science, **27** (1974), 147.

[50] C. E. Fichtel *et al.*; ApJ **186** (1973), 99.

[51] G. Bignami *et al.*; Space Sci. Instrum **1** (1975), 245.

[52] W. A. Mahoney *et al.*; *ApJ*, **262** (1982), 742.

[53] A. Palacios et al.; *Proceedings of the 5th INTEGRAL Workshop on the INTEGRAL Universe*, (2004), 111.

[54] J. Knödlseder *et al.*; *A & A*, **441** (2005), 513.

[55] K. S. Cheng *et al.*; *ApJ*, **645** (2006), 1138.

[56] N. Guessoum *et al.*; *A & A*, **457** (2006), 753.

[57] M. J. Harris *et al.*; *A& A*, **461** (2007), 723.

[58] F. W. Stecker;*Ap & SS*, **6** (1970), 377.

[59] F. A. Aharonian and A. M. Atoyan; *A & A* **362** (2000), 937.

[60] G. Ghirlanda *et al.*; *ApJ*, **613** (2004), 13.

[61] N. Tanvir *et al.*; *Nature*, **461** (2009) 1254.

[62] N. Salvaterra *et al.*; *Nature*, **461** (2009) 1258.

[63] Y. Inoue *et al.*; astro-ph/1001.0103

[64] V. Schönfelder *et al.*; *Astron. Astrophys. Suppl. Ser.*, **143** (2000), 145.

[65] R. C. Hartman *et al.*; *ApJS*, **123** (1999) 79.

[66] A. A. Abdo *et al.*; *ApJS*, **188** (2010) 405.

[67] B. Reiner *et al.*; *Chest*, **120** (2001), 1803.

[68] T. F. Delaney *et al.*; *Cancer Principles & Practice of Oncology*, **17** (2003), 1.

[69] T. F. Delaney *et al.*; *Int J Radiat Oncol Biol Phys. Supplement*, **42** (1995), 222.

[70] V. Benk *et al.*; *Int J Radiat Oncol Biol Phys.*, **31** (2003), 577.

[71] A. Terahara *et al.*; *Int. J. Radiat. Oncol. Biol. Phys.*, **45** (1999), 351.

[72] A. E. Rosenberg *et al.*; *American J.l of Surgical Pathology*, **23** (2003), 1370.

[73] Y. Shioyama *et al.*; *Int. J. Radiat. Oncol. Biol. Phys.*, **56** (2003), 7.

[74] Y. Matsuzaki *et al.*; *Radiol. Phys. Technol.* **3** (2010), 84.

[75] Y. K. Lim *et al.*; *Medical Dosimetrists*, in press.

[76] J. J. Coen and A. L. Zietman;*Nature Reviews Urology*, **6** (2009), 324.

[77] U. Schneider and E. Pedroni; *Med. Phys.*, **22** (1995), 353.

[78] J. Beebe-Wang *et al.*; *Nuclear Science Symposium Conference Record, 2003 IEEE* , **4** (2003), 2496.

[79] NNDC, http://www.nndc.bnl.gov/.

[80] J. Beebe-Wang *et al.*; *Proceedings of EPAC 2002, Paris, France*, (2002), 2721.

[81] K. S. Seo *et al.*; *J. Korean Phys. Soc.*, **48** (2006), 855.

[82] Jean in't Zand "Coded Aperture Imaging in High-Energy Astronomy " (http://lheawww.gsfc.nasa.gov/docs/cai/coded.html).

[83] S. D. Barthelmy *et al.*; *SSR*, **120** (2005), 143.

[84] Peter Von Ballmoos; *New Astronomy Reviews*, **48** (2004), 243.

[85] Le fonctionnement d'une lentille gamma (`http://www.cesr.fr/~pvb/lentille_gamma/L_fon_e.html`)

[86] G. Weidenspointner *et al.*; *A& A*, **368** (2001), 347.

[87] V. Schönfelder; *New Astronomy Reviews*, **48** (2004), 193.

[88] G. K. Loudos *et al.*; *Computerized Medical Imaging and Graphics*, **27** (2003), 307.

[89] C. S. Levin and E. J. Hoffman; *Phys. Med. Biol.*, **44** (1999), 781.

[90] S. Oishi *et al.*; *J. Radioanal. and Nucl. Chem.*, **239** (1999), 411.

[91] K. Matsumoto *et al.*; *Biol. Pharm. Bull.*, **28** (2005), 2029.

[92] M. Singh and D. Doria; *Med. Phys.*, **10** (1982), 428.

[93] S. Motomura *et al.*; *Pure Appl. Chem.*, **80** (2008), 2657.

[94] A. Studen *et al.*; *Nucl. Instr. and Meth. A*, **501** (2003), 273

[95] A. Zoglauer, and G. Kanbach ; *Proceeding of SPIE*, **4851** (2003), 1302.

[96] A. Takada; Ph. D. Thesis, Kyoto Univ. (2007).

[97] T. Nagayoshi; Ph. D. Thesis, Kyoto Univ. (2004).

[98] K. Hattori; Ph. D. Thesis, Kyoto Univ. (2009).

[99] O. Sasaki; "Amplifier-Shaper-Discriminator ICs and ASD Boards" (http://online.kek.jp/˜sosamu/ASD-PRR.pdf)

[100] R. Orito; Ph. D. Thesis, Kyoto Univ. (2005).

[101] H. Sekiya *et al.*; *Nucl. Instr. and Meth. A*, **563** (2006), 49.

[102] G. R. Lynch, O. I. Dahl; *Nucl. Instr. and Meth. B*, **58** (1991), 6.

[103] K. Parodi *et al.*; *Phys Med Biol.*, **47** (2002), 21.

[104] K. Parodi *et al.*; *IEEE Trans. Nucl. Sci.*, **52** (2005), 778.

[105] K. Parodi *et al.*; *Med. Phys.*, **34** (2007), 419.

[106] " Stopping Powers and Ranges for Protons and Alpha Particles, " *ICRU, Rep.* (993) 49..

[107] M.-H. Richard *et al.*; *2009 IEEE Nuclear Science Symposium Conference Record*, (2009), 4172.

[108] J-W. Kim and D. Kim; *Radiation Measurements*, **45** (2010), 1417.

[109] J. C. Polff *et al.*; *Phys. Med. Biol.*, **54** (2009), 519.

[110] F. L. Foulher *et al.*; *IEEE Trans. Nucl. Sci.*, **57** (2010), 2768.

[111] M.-S. Park *et al.*; *App. Phys.letter*, **97** (2010), 153705.

[112] V. Schönfelder; *Advances in Space Research*, **11** (1991), 313.

[113] M. Takahashi, *et al.*; *Nucl. Instr. and Meth. A*, in press.

[114] J. D. Parker *et al.*; *Nuclear Science Symposium Conference Record (NSS/MIC), 2009 IEEE* , (2009), 1107.

[115] C. Trotta *et al.*; *Nucl. Instr. and Meth. A*, **577** (2007), 604.

[116] Y. Chou *et al.*; *ApJ*, **618** (2005), 856.

[117] L. Bouchet *et al.*; *ApJ*, **548** (2001), 990.

[118] S. M. Schindler *et al.*; *Nucl. Instr. and Meth. A*, **384** (1997), 425.

[119] H. O. Anger; *Rev. Sci. Instr.*, **29** (1958), 27.

[120] S. Surti *et al.*; *IEEE Trans. Nucl. Sci.*, **50** (2003), 1357.

[121] W.-H. Wong; *IEEE Trans. Nucl. Sci.*, **40** (1993), 962.

[122] S. Kim *et al.*; *IEEE Trans. Nucl. Sci.*, **53** (2006), 40.

[123] R. Pani *et al.*; *Nucl. Instr. and Meth. A*, **477** (2002), 72.

[124] S. Siegel *et al.*; *IEEE Trans. Nucl. Sci.*, **43** (1996), 1634.

[125] R. Pani *et al.*; *Nucl. Instr. and Meth. B*, **213** (2004), 197.

[126] C. S. Levin; *Nucl. Instr. and Meth. A*, **497** (2003), 60.

[127] W. R. Cook *et al.*; *IEEE Trans. Nucl. Sci.*, **32** (1985), 129.

[128] T. Y. Song. *et al.*; *IEEE Trans. Nucl. Sci.*, **52** (2005), 1396.

[129] R. Pani *et al.*; *Nucl. Instr. and Meth. A*, **576** (2007), 15.

[130] R. Pani *et al.*; *Nucl. Instr. and Meth. A*, **571** (2007), 187.

[131] H. Nishimura *et al.*; *Nucl. Instr. and Meth. A*, **573** (2007), 115.

[132] K. Takagi, and T. Fukazawa ; *Appl. Phys. Lett*, **42** (1983), 43.

[133] H. Ishibashi *et al.* ; *IEEE Trans. Nucl. Sci.*, **38** (1989), 170.

[134] R. Hofstadter ; *Phys. Rev.*, **74** (1948), 100.

[135] W. van Sciver, and R. Hofstadter ; *Phys. Rev.*, **84** (1951), 1062.

[136] M. Kobayashi *et al.* ; *Nucl. Instr. and Meth. A*, **330** (1993), 115.

[137] W. Lee, D. K. Wehe, and B. Kim ; *IEEE Trans. Nucl. Sci.*, **52** (2005), 1119.

[138] K. Shimizu *et al.*; *IEEE Trans. Nucl. Sci.*, **35** (1988), 717.

[139] J. Rogers et. al.; *IEEE Trans. Nucl. Sci.*, **36** (1989), 993.

[140] W-H. Wong; *IEEE Trans. Nucl. Sci.*, **33** (1986), 591.

[141] J. S. Karp; *Nucl. Instr. and Meth. A*, **260** (1987), 509.

[142] E. V. D. van Loef *et al.*; *Appl. Phys. Lett.*, **79** (2001), 1573.

[143] E. V. D. van Loef *et al.*; *Nucl. Instr. and Meth. A*, **486** (2002), 254.

[144] P. R. Menge *et al.*; *Nucl. Instr. and Meth. A*, **579** (2007), 6.

[145] K. S. Shah *et al.*; *IEEE Trans. Nucl. Sci.*, **50** (2003), 2410.

[146] K. S. Shah *et al.*; *IEEE Trans. Nucl. Sci.*, **51** (2004), 2395.

[147] A. Iltis *et al.*; *Nucl. Instr. and Meth. A*, **563** (2006), 359.

[148] J. Glodo *et al.*; *IEEE Trans. Nucl. Sci.*, **52** (2005), 1805.

[149] P. F. Bloser *et al.*; *Nucl. Sci. Symp. Conf. Rec.*, **3** (2006), 1500.

[150] S. Normand *et al.*; *Nucl. Instr. and Meth. A*, **572** (2007), 754.

[151] J. Seguinot *et al.*; *Il Nuovo Cimento C*, **29** (2006), 429.

[152] W. M. Higgins *et al.*; *J. of Crystal Growth*, **287** (2006), 239.

[153] P. F. Bloser *et al.*; *Nucl. Sci. Symp. Conf. Rec.*, **2** (2006), 1204.

[154] A. Kuhn *et al.*; *IEEE Trans. Nucl. Sci.*, **51** (2004), 2550.

[155] R. Pani *et al.*; *Nucl. Instr. and Meth. A*, **567** (2006), 294.

[156] M. Kokubun *et al.*; *IEEE NSS-MIC 2006, October 29 Nov. 4, 2006, at San Diego, N30-92* (2006).

[157] G. L. Case *et al.*; *Proceeding of SPIE*, **5898** (2005), 58980K.

[158] B. Budden *et al.*; *Nucl. Sci. Symp. Conf. Rec*, **2** (2006), 943.

[159] C. M. Rozsa *et al.*; *Saint Gobain Crystals*, available at www.detectors.saintgobain.com.

[160] Hamamatsu Photonics K.K.; R6231 PMT data sheet; Japan.

[161] K. Hattori; Master Thesis, Kyoto Univ. (2006).

[162] L. A. Shepp, and Y. Vardi; *IEEE Trans. Med. Imag.*, **MI-1** (1985), 113.

Acknowledgments

First and foremost I would like to thank my advisor, Professor Toru Tanimori. He has taught me how good experimental physics is done. I appreciate all his contributions of time and ideas to make my Ph.D. experience productive and stimulating. This thesis would not be completed without his support. Also, I would like to thank Dr. Hidetoshi Kubo for his advice. He taught me how good experimental physics is done.

In the medical imaging study, I greatly thank the collaborators in Korea, Dr. J-W. Kim (Korea national cancer center) and Mr. D. Kim (Seoul Univ.) for their supports. In addition, they was very helpful in my Korean trip. For the preparation of the proton beam test, I would like to tank Mr. K. Ueno (RIKEN) Dr. S. Kabuki, Mr. S. Iwaki, Mr. M. Takahashi, Mr. K. Taniue, and Mr. N. HIgashi (Kyoto Univ.).

For the development of the $LaBr_3$ arrays, I would like to thank you Dr. Y. Yanagida and Mr. T. Kadono. My works would not be completed without their support.

I specially thanks to our MeV-gamma ray collaborators Dr. K. Miuchi, Dr. J. D. Parker, Dr. A. Takada, Dr. Y. Kishimoto, Mr. T. Sawano, Mr. K. Nakamura Mr. Y. Matsuoka Mr. M. Aono (Kyoto Univ.), Dr. K. Hattori (Okayama Univ.) and Dr. H. Nishimura. I also thank my colleagues and friends: Mr. M. Nobukawa, S. Nakano, and Y. Takikawa.

This work was supported by the Korea Japan Collaborative Research Project funded by National Research Foundation of Korea, Japan Society for the Promotion of Science (JSPS) , Scientific Research of the Japan Ministry of Education, Culture, Science, Sports, Technology (MEXT), "SENTAN" by the Japan Science and Technology Agency (JST), the Global COE Program "The Next Generation of Physics, Spun from Universality and Emergence" from the MEXT, and JSPS Research Fellowships for Young Scientists.

In addition, Dr. M. Ishiura and Dr. T. Kouyama (Nagoya Univ.) taught me the technique of the experiment and support my study life. Finally, I am forever indebted to my family and caretaker of my house in Kyoto, who is 101 years old !, for their understanding, endless patience and encouragement.

KUROSAWA, Shunsuke
Kyoto University
January 2011